Rotation of the Sodium Driven Bacterial Flagellar Motor

ALEXANDER D. ROWE

A thesis submitted in partial fulfillment of
the requirements for the degree of
Doctor of Philosophy at the University of Oxford

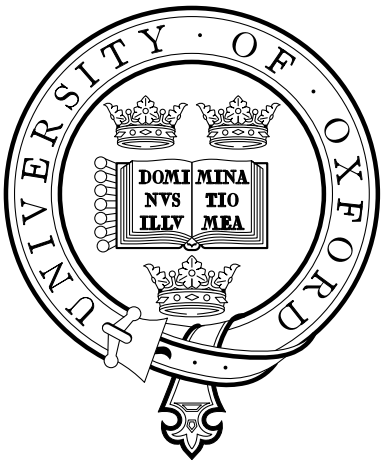

The Queen's College
University of Oxford
Trinity Term 2005

Rotation of the Sodium Driven Bacterial Flagellar Motor

Alexander D. Rowe, The Queen's College.

Thesis submitted for the degree of Doctor of Philosophy
at the University of Oxford, Trinity Term 2005.

Abstract

This thesis describes the investigation of high-speed and low-speed rotation in the sodium-driven bacterial flagellar motor and a series of experimental techniques which were developed for this purpose. A home-made laser trap and novel microfluidic laminar-flow assay were combined to measure the torque-speed relation of *Vibrio alginolyticus* in a range of sodium concentrations and viscosities.

A chimæric sodium driven *Escherichia coli* flagellar motor was provided for collaborative work by members of Nagoya University, Japan. The torque-speed relation for this motor was investigated and the rates of stator association and dissociation at the rotor were measured. The number of stators driving the motor was discovered to be heavily dependent upon external sodium concentration and conditions for sustainable slow-speed single-stator rotation were derived.

Slow rotation conditions and high-precision angular detection techniques were used to attain the first experimental resolution of steps in an ion driven molecular motor. Under single-stator slow-rotation conditions the flagellar motor was discovered to rotate with 26 steps per revolution, which is consistent with the periodicity of the site of force generation of the rotor. This result validates stepping models for the bacterial flagellar motor.

Acknowledgements

It is my duty now to thank a host of people, whose contribution to this DPhil must be recognised.
First and foremost must come my supervisor, Richard Berry, whose tireless pursuit of perfection is an example to us all. Thank you for entertaining even the most tenuous notions I put forward as grand theories of a few little things.
The members of my lab, in order of seniority:
Dr Mark Leake, whose wholehearted devotion to my personal advancement over the last four years has been nothing short of outstanding.
Teuta Pilizota, Gabriel Mendes, Jennifer Chandler, Bai Fan, Chien-Jung Lo, Stuart Reid and Tania Saxl; it has been a pleasure. Good luck.
George and Steve in B4 for their help with microbiology.
The staff of the Physics workshop for countless hours spent with me as I manufactured intricate devices, and the ever present contractors for providing the obligatory low frequency noise, without which no experimental data set would be complete.

It remains for me to thank those who have supported me financially.
The EPSRC for the studentship, and John Ryan and his IRC for direct and indirect support of my research.

Finally, in memory of a friend who wasn't around for long enough.
John Ibbotson 17.07.1978-27.09.2005

To those who made this possible, I express my sincere gratitude and to those who find this useful in the future, I salute you.

Contents

Chapter 1

Biophysics and Molecular Motors

'Science has "explained" nothing; the more we know the more fantastic the world becomes and the profounder the surrounding darkness.'
Aldous Huxley (1894-1963)

1.1 Introduction

The ultimate aim of all investigations into molecular motors must be to generate a model which replicates and explains the behaviour of the system across the full range of potential biological and experimental conditions. Only at this point can it be truly stated that the system is understood. Ideally therefore all possible variables affecting the system must be controlled in such a manner as to limit experimental ambiguity, thereby refining the model.

This thesis aims to fulfil the dual purpose of recording my research on the rotary bacterial flagellar motor and, more generally, drawing together some of the most directly relevant biology necessary to create a picture of the complex systems and structures which form the background to this research. Many of the biological subjects summarised, while trivial to a biochemist, are largely unknown to the physicist and must be considered, given that they potentially form an indispensable part of a robust model.

Controlled movement on all scales is fundamental to the maintenance of life in biological systems. From the macroscopic muscles that transport a creature through

its environment, to the microscopic transport systems that organize and control the contents of cells, there exists a range of natural motors acting either individually or cooperatively, that generate linear or rotary force at controlled rates and in specific directions. The composite behaviour of large groups of these motors acting as a single system has been observed and measured thoroughly - muscle is a prime example [1] - but this tells us little about the actual origin of the forces in the macroscopic system.

This implies the central question which drives this research:

> *What can be inferred about quanta of force generated within these motors from the behaviour of single components of the ensemble?*

The movement of individual motor sub-units has only recently been observed. The main obstacles to elucidating the mechanisms of individual motors are their size and environment. In systems with physical dimensions of microns and below, the rules of macro-scale physics no longer apply. Inertia is insignificant while brownian motion and intermolecular forces dominate. Until relatively recently the techniques to manipulate and isolate single motors were not available. By a combination of fortuitous circumstance and design [2], the application of physics techniques to biological problems provided an array of techniques which simultaneously afforded a means to measure forces with piconewton (pN) precision and position with nanometre (nm) accuracy.

In order to familiarise the reader with the progress experimentalists have made and to contextualise their results in light of the inevitable physical limitations which apply, the remainder of this chapter gives a general overview of the molecular motors field followed by a review of the development of experimental techniques applied to measuring flagellar motor rotation. Particular reference is made to "optical tweezers," since they form the basis of my experimental techniques.

There follows a fuller appraisal of a generic swimming bacterium. Starting with a motile cell, the modes of movement and the control systems behind them are summarised before delving into the cellular function of the bacterium.

Using the relatively well understood *Escherichia coli* (and in parts the *Vibrio alginolyticus*) cell as a template, the structure and energetics of the bacterium which are relevant to the assembly and function of the flagellar motor are discussed. What has so far been discovered - in terms of protein structure and function - about the various types of flagellar motor is summarised, followed by a general evaluation

of existing motor rotation models. Chapter 2 covers the techniques which were developed and adapted for high speed rotation detection and high angular resolution, that formed the basis of my experimental setup. Chapter 3 describes the creation and use of a microfluidic assay and its application to measuring the torque-speed relation of *V. alginolyticus* at a range of sodium concentrations. Chapter 4 is a summary of the results from a range of characterisation experiments carried out on a new chimæric flagellar motor, to determine conditions for stable low speed rotation. A partial torque-speed relation is also derived and short timescale fluctuations in rotation are examined in order to extend our knowledge of the real-time assembly process for the flagellar motor. The most significant contribution of this thesis is contained in Chapter 5 where two separate experiments were carried out to detect fine structure in the angular position of slow rotating flagellar motors. The result, the first of its kind for an ion driven motor, shows that the motor takes 26 steps per revolution.

Immediate conclusions are given at the end of each chapter, while the wider ranging implications of these results are drawn together in Chapter 6, with an outline for relevant further work.

1.2 Molecular Motors - A General Summary

Naturally occurring molecular motors fall into one of two categories, either linear motors which run in a preferred direction along a specific track, or rotary motors. Lately there have been advances made in the synthesis of true molecular motors using DNA which also warrant a mention, given the bio-nanotechnological setting of this research. Since the motors investigated for this thesis form a subset of the rotary motor group, I have given a general summary of the main categories of molecular motor, for completeness and for comparison.

1.2.1 Linear Motors

Twin Headed Stepping Motors

The Myosin and Kinesin families are well known natural linear motors with similar modes of force generation. The myosin family which travel along actin filaments are abundant in nature, as are the kinesins and dyneins - which travel unidirectionally and in opposite directions - along microtubules. In both cases they are formed by the pairing of two similar large proteins (∼500 kDa molecular weight) with three distinct structural domains. In the case of myosin-V, the (220 kDa) tail domains of a pair spontaneously form a long (1700 Å) helically coiled filament in physiological solution, splitting at one end into two neck domains, each of which terminates in a globular head region roughly 160 Å long and 50 Å in diameter [1].
Each head and neck region alone can function as a motor for short times, however it is the combined action of the paired structures that represents true linear motor behaviour.

Kinesins have been observed to take hundreds of successive 8 nm steps in a positive direction along microtubules towing a load of up to 6 pN [3], while dyneins have been reported to move in a retrograde manner along microtubules with a load-dependent step size. In low load conditions they appear to take steps of 15, 24 or 32 nm, while in high load conditions they take 8 nm steps while exerting a maximal force of 1.1 pN [4].

The head domains of these molecules are the force generating units. Each head forms a mechano-enzyme which catalyses the conversion of chemical bond energy from the exothermic breakdown of ATP to provide the mechanical energy to move the molecule in a forward direction along the track. In the case of myosin-V this can happen at speeds up to 550 nms^{-1} with run lengths normally distributed around 800 nm [5].

Taking myosin-V as an example; in solution a myosin head naturally binds to the polymerised form of actin (F-actin) which forms a filamentous track for the myosin to follow. This forms a complex known as actomyosin. This complex can be made to dissociate by the addition of ATP to the solution.

The general model for the processive walk of a two headed myosin motor along an actin filament cycles through the following sequence [6, 7]. Starting, for simplicity, with both heads bound to the actin filament, separated by a 36 nm interval, the strain in the neck domain of the forward head (1) gates the release of ADP from the rear head (2) resulting in a 5 nm forward progression, while keeping this domain firmly shut in the forward head (1). A single ATP molecule may then bind to a site on the rear head (2), causing it to dissociate from the actin. In so doing it releases the strain in the neck domain of the forward head (1), carrying out a 20 nm working stroke. The unbound head (2) then explores the actin filament and binds weakly to the next actin binding site,[1] releasing the phosphate ion, which triggers the "powerstroke" during which the newly bound head (2) applies strain to the neck domain, to return to the beginning of the cycle. The process of rebinding for an unbound head requires an extra 11nm diffusional contribution in the forward direction to complete the full 36 nm stepping cycle [7]. This cycle has been broken down into six discrete processes, which are subsets of the general processes I describe, [5], but opinion is not yet settled on the exact division of processes involved in force generation.

Thus by successive processing of single ATP molecules, a myosin motor can walk directionally along an actin filament; a system which has been demonstrated by sticking myosins to a coverslip and introducing fluorescent actin filaments. Using fluorescence microscopy, these filaments can be seen to move around the surface of the coverslip in response to the addition of ATP.[2] The employment of optical tweezers to hold a single actin filament - pulled taut between two trapped latex beads - in contact with a single myosin motor has resolved the individual 36 nm steps [8, 9] and substeps [7] in the motor process, through observation of the displacement of the attached beads during actomyosin interaction.

Likewise this assay has been used to measure the step sizes of kinesin. Compared to myosin-V, the shorter flexible neck domains of kinesin correlate inevitably with

[1] Despite the actin molecule being repeated every 2.75 nm in the filament the helical pitch of the actin polymer (which is 36 nm) defines the size of the complete motor step, implying that the motor sticks to its original orientation on the actin filament rather than rotating around it. This minimises azimuthal distortion.

[2] www.motility.york.ac.uk : In vitro motility assay videos show this clearly.

smaller 8 nm step lengths, which also match the separation of the microtubule repeat, and despite reports of the possibility of substeps, the latest results rule out the presence of substeps which take place in a time greater than 30 μs [10].

Perhaps the most relevant concepts for comparison between the flagellar motor and linear motors are those of duty ratio and processivity while running along a track. In order for a motor to move a load more than a few steps along a track without being removed from the track by diffusion, the proportion of time a motor spends attached to its track (this proportion is known as duty ratio (r)) must tend towards 1. In the case of a single headed motor, this clearly cannot be the case, since diffusion is also what moves the detached motor domain between sites where it binds. In fact, for a single head of myosin-V the duty ratio r is around 0.7. A two headed motor with both heads acting stochastically and independently, however, only requires a single head domain to be attached to the track for the effective motor to continue processing along the track. The probability of at least a single head being attached to the track is $2r - r^2$, which is significantly closer to 1 than the individual duty ratios. This allows the mean number of steps taken by the motor before dissociation from the track to be described by a processivity number $P_n = 1 + [\ln 2/(-\ln(2r - r^2))]$. This value ($\sim$8 for $r = 0.7$) actually turns out to be low compared to experimentally derived values (between 20 and 60) and the latest work in the field considers load dependence of the kinetics in the head domains and linking between neck domains which biases the kinetics and searching process towards a higher processivity, in order to explain this phenomenon [11].

Synthetic DNA Motors

Apart from the naturally occurring motor proteins which travel along DNA such as DNA helicase, there are synthetic DNA-only motors being made which allow a single strand of DNA attached to a cargo to move directionally along a predefined DNA track, using a further set of strands as fuel in the process.

One of the best known early demonstrations of the cyclical force generation process required for any motor was the DNA tweezer [12] made by Andrew Turberfield and colleagues at Bell Labs. The introduction of one type of short fuel strand to the medium surrounding the tweezer structure closed the tweezer arms and the subsequent addition of another short strand which unbound the original fuel from the tweezer reopened the arms. This was a repeatable process.

Since then work has been successfully carried out to overcome the need for the fuel to be changed in order to produce a motor step. By judicious sequencing of the

bases in the strands involved, the conformation of the cargo, track and fuel strands at each point in the process means that a forward step is kinetically favourable [13, 14, 15].

1.2.2 Rotary Motors

There are two distinct forms of rotary molecular motor; those using the hydrolysis of ATP as an energy source and those which rely upon ion flux driven by an electrochemical potential to couple torque.

ATP Driven

Of the rotary motors that are powered by ATP hydrolysis, probably the best known is the F_1F_O-ATPase shown in Figure 1.1. This ∼10 nm diameter ∼500 kDa enzyme consists of a central γ-subunit which rotates inside a cylinder formed alternately from three α and three β subunits. Kilohertz imaging of a single motor rotating at ∼130 Hz with a 40 nm gold bead attached to the rotor [16] has revealed distinct 120° steps in the rotation, each of which consists of an 80° and a 40° substep [17]. The torque at high load has been measured at 40 pN nm.

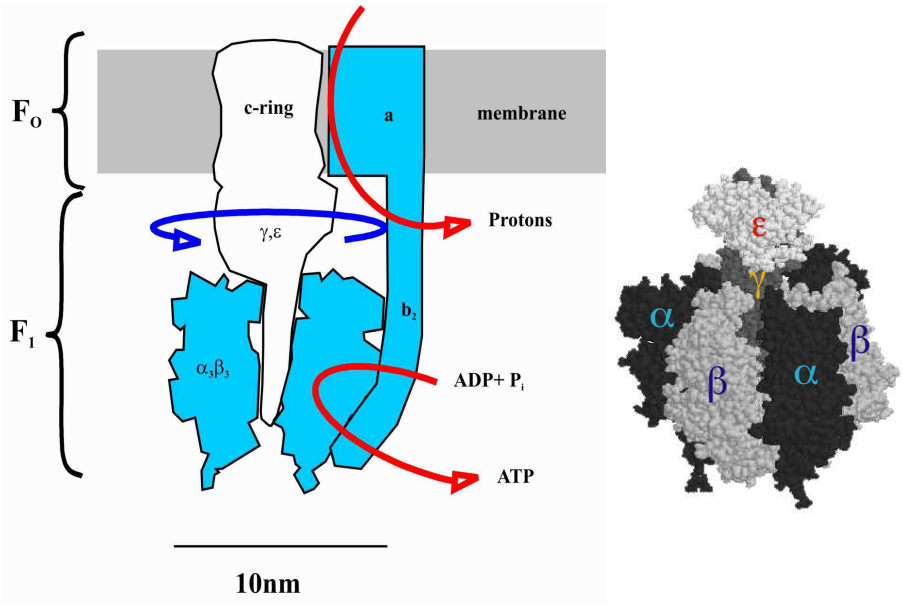

Figure 1.1: The protein structure of the ∼10 nm diameter F_1F_OATPase molecule. A cross section through the motor is shown on the left and a space-filling 3d protein structure of the F_1 section is shown on the right (R. Berry, with permission). The central γ subunit - which projects down inside the 6-fold segmented stator structure of alternate α and β subunits - rotates about its long axis, driven by the hydrolysis of ATP.

The in-vivo function of both the F_1 and F_O sections of the complex are known to be reversible in specific cases.[3] Either the ATP driven F_1 section can rotate the γ axle to drive protons through the F_O section which would be set in the membrane, to create a membrane potential, or the membrane potential can be used to drive the axle and thereby synthesise ATP inside the membrane envelope. This mechanically driven ATP synthesis has recently been demonstrated in F_1 by attaching a magnetic particle to the γ subunit and turning it by means of a rotating magnetic field [18].

Ion Driven

Apart from the F_O component of the ATPase, whose rotation has been observed [19] but whose mechanism remains postulated [20, 21], the ion driven motor is defined by the bacterial flagellar motor. A full review of the structure and function of this type of motor follows (Section 1.4), but they are introduced briefly here.

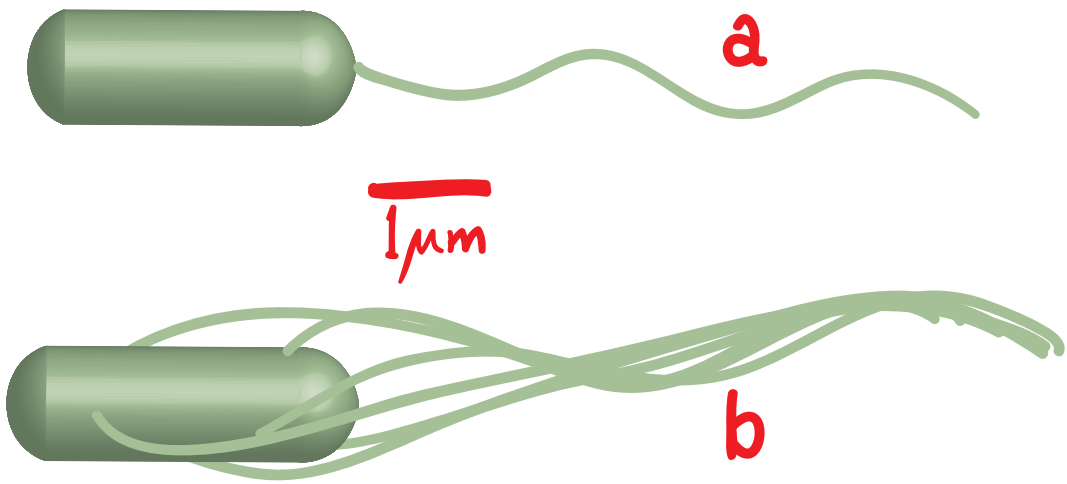

Figure 1.2: Basic morphology of flagellated bacterial species used for my experiments. (a) The freely swimming *V. alginolyticus* expresses a single flagellum at one pole of the cell. (b) The *E. coli* species expresses an average of six flagella around the cell surface. These flagella are attached via a flexible universal joint allowing them to rotate freely at any angle. During forward swimming the filaments form a bundle behind the cell, each rotating independently and thus slipping against the rest of the bundle.

Many species of bacteria propel themselves through aqueous media by rotating a single[4] (Figure 1.2a) semi-rigid helical flagellum, or a bundle[5] (Figure 1.2b) of flagella. These filaments are several microns long and 20-30 nm in cross section [22, 23] and are turned at their base by a ∼50 nm diameter rotary motor (Section

[3]This is species dependent. Many prevent the hydrolysis of ATP.
[4]In the case of freely swimming *V. alginolyticus* species.
[5]In the case of *E. coli* species.

1.4.7) embedded in the cell wall. The motor is driven by the passage of specific positively charged ions through the stator units, down the electrochemical gradient that the cell generates across the cytoplasmic membrane. The precise mechanism of energy transduction in these motors is not known.

In the case of *E. coli* and many other species, the powering ions are protons [24], wheras in the case of alkalophilic and marine species such as *V. alginolyticus*, rotation can be driven by sodium ions [25]. The flagella of proton driven motors are known to rotate at rates up to 150 Hz [26], while the sodium driven filaments of *V. alginolyticus* have been observed rotating at speeds as high as 1700 Hz [23].

1.3 Experimental Techniques Review

Since the first definite experimental corroboration [27, 28, 29] of the statement that "bacteria swim by rotating their flagellar filaments" [30] there have been many techniques applied to the further investigation of this rotation. Some of these are now redundant or have been improved dramatically, while others are still relied upon.

1.3.1 Assays for Rotation Rate Measurement

Flagellar rotation is characterised by low Reynolds number dynamics where inertia is negligible and the rotation rate is equal to the instantaneous torque divided by the rotational drag coefficient.

Tethered Cells

For many years the dominant technique for observing single motor rotation was the tethered cell assay, where a cell is attached to a microscope coverslip by a flagellar filament and the motor causes the cell body to rotate, as shown in Figure 1.3(a). The drag coefficient of the cell body is considerably greater than that of the filament, thus the motor in a tethered cell operates in a low-speed, high-load regime compared to the motor in a freely swimming cell and the rotation rates observed in this assay fall below 10 Hz. Accurate measurements of rotation rates were generally made by counting from video records or by frequency analysis of a section of the image whose intensity depended upon the angle of the cell body.

Faster Rotation Detection Assays

Various methods have since been employed to observe faster flagellar rotation. The first was similar in part to the method used for the experiments in Chapter 3 which is discussed in detail later in Section 2.2 and was published as a techniques paper for the detection of high speed rotation in micron sized particles [32]. The fundamental difference is that this technique was applied to a population of cells rather than a single cell [26]. The image of a chamber containing cells at a density of $4\text{x}10^8$ ml^{-1} was projected onto a photodiode that was assumed to be position-sensitive and the power spectrum of the diode signal showed two broad peaks. The faster peak showed the flagellar rotation rate while the slow peak showed the rate

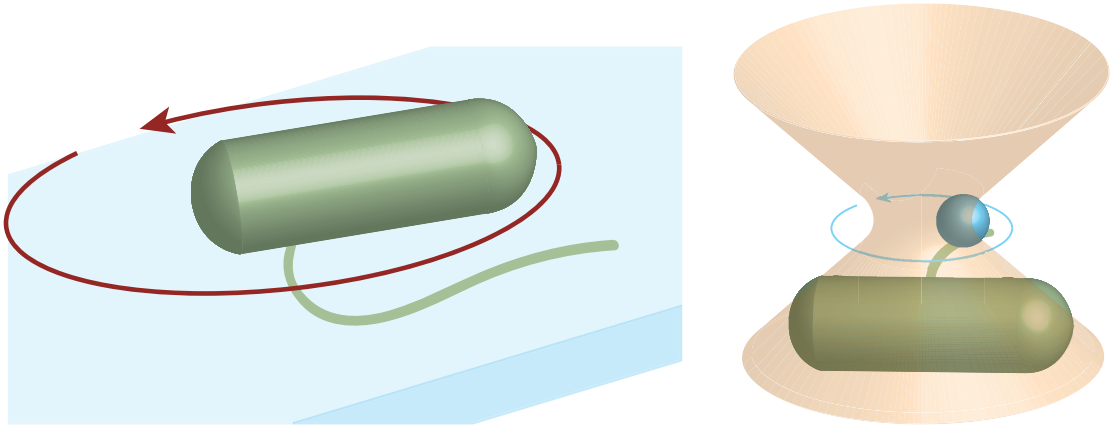

(a) Tethered cells on glass. (b) Bead labelled flagella.

Figure 1.3: (a) The traditional rotation assay immobilised *E. coli* by covalently fastening a flagellum onto glass [31]. The cell body then rotated in the plane of the surface. The high load conditions produce rotation rates in the region of 10 Hz. (b) A modern, variable load, rotation assay involves sticking the cell body to glass with polylysine and attaching a variety of latex beads to sheared flagellar stubs. The diameter of the bead and the radius of rotation which lies reliably between 150 and 250 nm determine the viscous load on the motor and the rotation rate can be measured using a laser trap with back focal plane (BFP) interferometry, thus inferring the instantaneous torque of the motor.

of counter-rotation of the cell body.[6]

Beads on Flagellar Stubs

Subsequent techniques have attached small polystyrene beads to truncated flagella (See Figure 1.3(b)) as indicators of rotation [33]. The viscous load on the motor depends upon the bead diameter and the eccentricity of rotation.[7] By tracking the position of the bead label, the motor speed may be related to the torque required to rotate the viscous load. Since this load is dependent upon the bead diameter, this assay allows the torque-speed relation for the motor to be investigated by varying the diameter of the bead.

It should be noted that in all of the above cases the exact values for load, and thus torque generated by the motor, rely upon hydrodynamic estimation of the drag coefficients of either the cell body or the bead and flagellar stub combination. While these can be quite accurate for large beads, the presence of an unknown length of flagellar stub becomes a significant factor in error contribution when the bead size used is small. The unknown flagellar stub lengths in the experiments of Ryu [33]

[6]This inevitable counter-rotation will often be referred to as "body-roll."

[7]There is the additional consideration of the drag contributed by the unknown length of the flagellar stub. This is discussed in the context of the experiments of Chapter 4.

were estimated to be between 0.7 and 1.2 μm. The drag contribution from stubs of this length can be up to twice that of a 0.5 μm bead, setting a lower limit to the loads applicable by this means.

Laser Dark Field Microscopy

An alternate technique for measuring high speed filament rotation is laser-dark-field (LDF) microscopy [34]. A cell passing through the dark-field laser beam in ∼0.05 s or less will scatter some of the incident light into the imaging path. The cell body causes a large flare in images, which masks the signal from the first 4 μm of the flagellum, but the intensity of the illumination scattered into the imaging path by the remainder of the helix depends sufficiently upon the rotation angle of the flagellum for frequency spectrum analysis to reveal the rotation rate. Predominantly by means of LDF, experiments have shown that the speed of Na^+-driven motors in swimming cells of *V. alginolyticus* increases with Na^+ concentration [35]. LDF has been used to observe the rotation of flagella in swimming cells and to compare the flagellar rotation rate to the swimming speed of the cell. The fastest motor rotation rates have also been observed with LDF.

1.3.2 Techniques to Measure Torque and Speed

Techniques were also developed which expanded the range of operating torques and speeds in which motor rotation could be measured. These included laser trapping and electrorotation.

Electrorotation

Electrorotation is a technique that can be used as a non-invasive method of characterising the dielectric properties of single micron-sized particles such as biological cells. To induce electrorotation of a particle, a rotating electric field is required and this is generally accomplished using microelectrode structures. Characterisation of the rate of rotation of a particle as a function of the applied frequency can be used to determine the intrinsic dielectric properties of the particle [36]. The technique has been used to provide information on the biophysical properties of cells, and has also been used to characterise cell populations as a pre-requisite to separation using dielectrophoretic methods [37].

When a polarizable particle such as a latex bead or a biological cell is exposed to an externally applied electric field an induced dipole moment is formed. If the

electric field is non-uniform, this results in motion of the particle towards high or low strength electric fields, depending on the effective polarisability of the particle, i.e. dielectrophoresis [31]. If the electric field is uniform, the dipole moment aligns itself with the field. If the field vector changes direction, the induced dipole moment vector will attempt to realign itself with the electric field vector and the particle experiences a torque. In a rotating electric field the particle is continuously attempting to align with the field, leading to rotation at a constant angular velocity. This has been used to apply a range of torques to tethered cells [31, 38] in both a forward and backward direction in order to probe the extremes of the torque-speed relation.

Electrorotation relies on the dielectrophoretic susceptibility of the cell body and is therefore able to exert torque most effectively on a cell body whose major axis lies in the plane of rotation such as *E. coli* (Figure 1.3(a)). Furthermore the conductivity of the medium affects the dielectrophoresis, making it impossible to apply the technique to cells which require a medium with a high sodium content.

1.3.3 Single and Multiple Laser Traps

The technique of optical trapping, in which a focussed laser beam is used to hold a small dielectric particle at a fixed point in three dimensions, was first demonstrated in the mid-1970s by Arthur Ashkin, and was applied to biological specimens in 1987 [2]. Infra-red wavelengths, typically of 1064 nm, are chosen for the low level of photodamage they cause to biological specimens [39]. The laser beam is brought to a diffraction-limited focus by a high numerical aperture (NA>1) microscope objective lens. Particles close to the focus, with a refractive index greater than their surroundings[8] (typically an aqueous solution) are drawn into what is essentially a potential well at the focal point (See Figure 1.4). This may be understood either by considering the exchange of momentum between a trapped particle and the incident photons which it deflects, or in terms of minimization of the energy in the laser radiation field.

Trapping forces have been modelled using ray optics [40] and Rayleigh scattering respectively for particles much larger or much smaller than the wavelength of the trapping laser beam.[9] Calculated and experimentally measured trapping forces are broadly in agreement [43], with trap force scaling as laser power times particle radius

[8]The refractive index relative to water is ∼1.16 for polystyrene beads and ∼1.05 for biological specimens.

[9]2004 saw the modelling of the trapping force for particles with dimensions of the order of the wavelength of the trapping laser [41, 42].

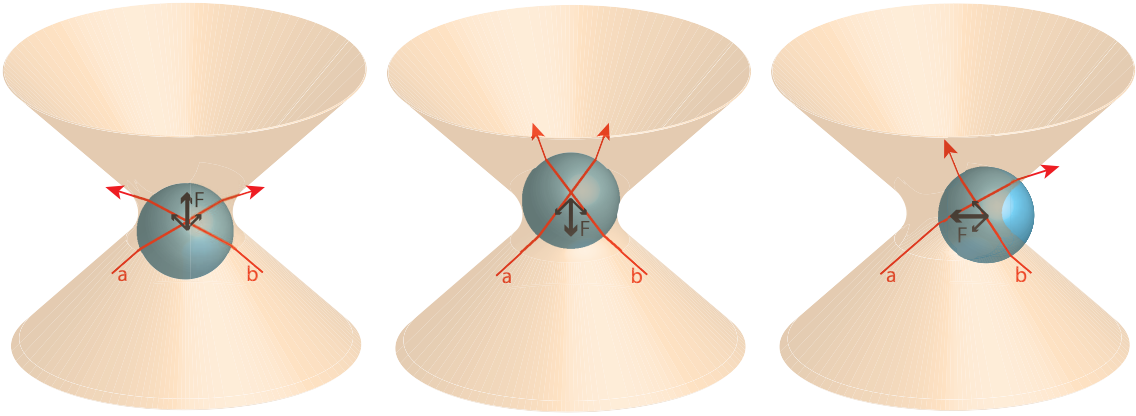

Figure 1.4: A ray optic treatment of the restoring forces (F) applied to a trapped particle which is deflected from the focus of the laser trap. In each instance the resultant force is towards the centre of the trap.

in the ray optics regime. Trapping forces in intermediate and Rayleigh regimes have been shown to scale with laser power, by experiment.

The maximal trapping force for a 1 W laser at 1064 nm wavelength on 1 μm diameter polystyrene particles in aqueous solution is of the order of 100 pN, which implies a trap stiffness in the region of $\sim$0.2 pNnm^{-1} [44]. The force restoring a trapped particle to the centre of the trap is linearly related to the displacement within the diffraction limited range of the focal spot.

The magnitude of forces applicable with laser tweezers makes them ideal tools for the study of biological molecular motors and they have been used to measure the pN forces and nm displacements invloved in the movement of many types of molecular motors including Myosin-V [8] and kinesin [45, 10].

The side effect of a laser tweezer technique, aside from photodamage [39] is local heating at the focus. The implication of experiments carried out by Dr Mark Leake in his pomp [44], is that there will be a local temperature increase of $\sim$2°C per 100 mW of 1064 nm wavelength trapping power.

1.3.4 Laser Trap for Position and Force Detection

Given a trapped particle displaced from the centre of the focus, it is useful to know what force the trap is exerting on it. For this purpose we first need to know the displacement of the particle from the centre of the trap.

Position Detection

Displacements may be measured from the image of the trapped particle [46], or alternatively by measuring the deflection of either the trapping beam [47] or a second, separate, laser beam [48]. In the latter techniques, the transmitted laser beam is collimated by a condenser lens and the back-focal-plane (BFP) of the condenser is imaged onto a quadrant photodiode. See Figure 2.1 for the layout of a single beam BFP detector.

During experiments, photo-currents from each of the four quadrants of a quadrant photodiode were amplified using a home-made current to voltage amplifier, and sampled at up to 5 kHz. The coordinates of a trapped particle deflected in the x direction P_x and y direction P_y are calculated as

$$P_x = \frac{(V_a + V_b) - (V_c + V_d)}{V_a + V_b + V_c + V_d}, \tag{1.1}$$

$$P_y = \frac{(V_a + V_c) - (V_b + V_d)}{V_a + V_b + V_c + V_d}, \tag{1.2}$$

where V_a, V_b, V_c and V_d are the sampled voltages from the quadrant diode.
The relative magnitude of the signal ($V_a+V_b+V_c+V_d$) may also be used as a measure of the displacement along the optical axis [49], although this was not applied in these experiments.[10]

A point relevant to measuring position accurately is that it is often the case that one[11] of the four quadrants of the photodiode has a response $\sim$5% weaker than the other three, which distorts a position signal unless it is taken into account. In this case, relative to the A quadrant, the responses were $V_b = 1.06 \times V_a$, $V_c = 1.05 \times V_a$, $V_d = 1.07 \times V_a$. This was most relevant to the measurements taken during the rotational stepping experiment in Section 5.

This detection method is well suited to experiments requiring high time resolution, as the high intensity of the focussed laser beam avoids the problem of shot noise that arises with lower intensity detection.

[10] With a numerical aperture of 1 for light collection at the condenser as set by an air gap between the slide and condenser, the light gathered can depend on the contents of the trap. The presence of a cell does not, however, affect it significantly. A higher refractive index object such as a bead will increase the amount of light transmitted. A 1 μm bead will increase it by $\sim$14% and a 0.4μm bead by about 8%. With an oiled condenser this variation is considerably lower.

[11] Quadrant A, stated by the manufacturer, UDT Sensors.

Trapping Force and Stiffness

Trapping forces may be calibrated actively or passively.[12] The obvious active methods involve calculating the displacement in the trap of a bead with known drag coefficient experiencing a known constant force, for instance a bead being moved in a large circle at a constant velocity. The relaxation time for a bead experiencing a step shift of position from the trapping beam may also be used.

One passive approach used is the equipartition method, where the trap stiffness κ is related to the variance of the thermal motion of a trapped bead $\langle x^2 \rangle$, the temperature T and the Boltzmann constant k, by

$$\kappa = \frac{kT}{\langle x^2 \rangle}. \tag{1.3}$$

However this requires accurate detector calibration and that the bandwidth of the detector encompasses the entire frequency range.

The preferred passive method[13] of calculating trap stiffness requires a Lorentzian line fit to a (log-log) plot of the power spectrum for the trapped particle.

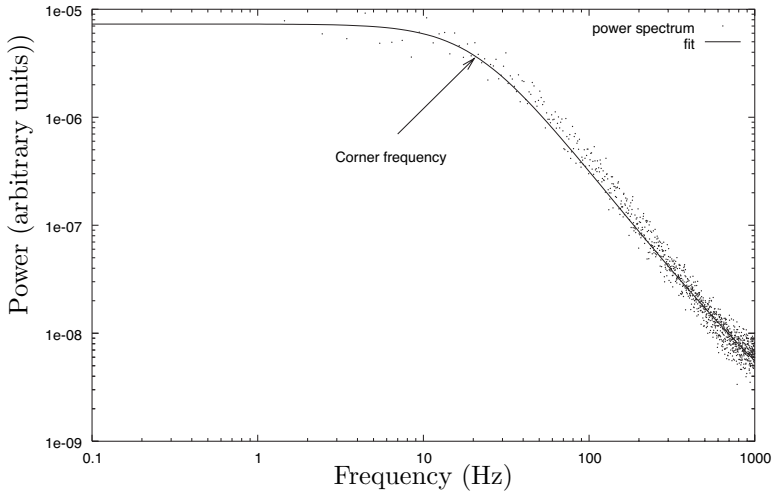

Figure 1.5: A Lorentzian line fit to the power spectrum of a 1.9 μm bead held in a 30 mW laser trap. The corner frequency is at 20.4 Hz, indicating a trap stiffness of 0.005 pN nm^{-1}.

Figure 1.5 shows a power spectrum of calibration data from my trap, with a

[12] An excellent summary of all things trapping can be found at http://motility.york.ac.uk/private/toc.html.

[13] Some doubt has been cast on the exactness of this method by Peterman *et al.* on account of the local heating experienced by the trapped bead which will affect the viscosity of the immediate solution [50]. However this will only be a serious issue at higher laser powers (>100 mW) and in solutions of higher absorbance than water.

Lorentzian fit $S(f)$ given by

$$S(f) = \frac{S_0 f_0^2}{f_0^2 + f^2}, \tag{1.4}$$

which intersects the $f = 0$ axis at S_0 and has a frequency f_0 at which $S = S_0/2$. The fit reveal the "corner frequency"[14] f_0.

The corner frequency is related to the trap stiffness by

$$f_0 = \frac{\kappa}{2\pi\gamma}, \tag{1.5}$$

where γ is the drag coefficient of the trapped particle.[15] This implies a trap stiffness of 0.005 pNnm^{-1} at 30 mW when trapping a 1.9 μm latex bead, which is reasonable.

ROTATION DETECTION

To obtain the rotation rate of a particle being held or detected by the trap, one second windows of data for P_x and P_y are combined to form a complex signal

$$P_C = P_x + iP_y. \tag{1.6}$$

For a particle rotating in a circle of radius A at angular velocity ω_0,

$$P_x = A\cos\omega_0 t, \tag{1.7}$$

$$P_y = A\sin\omega_0 t, \tag{1.8}$$

$$P_C = A\exp i\omega_0 t. \tag{1.9}$$

The complex power spectrum of P_C, which indicates the intensity of each frequency ω, has a single peak at ω_0. Thus the power spectrum of P_C indicates both the speed and the direction of any rotation between plus and minus the Nyquist frequency [38].

By far the easiest way to detect rotation of trapped particles was to feed the P_x and P_y signals into a loudspeaker or headphones. Any trapped particle that rotated would then generate a clear immediate sound at its rotational frequency. This simple method was used to assess the quality of the rotation signal from trapped *V. alginolyticus* cells (Chapter 3) and from beads on flagellar stubs (Chapter 4).

[14] Also known as the roll-off frequency.

[15] The drag coefficient for a sphere is $6\pi\eta r$ where $\eta = 10^{-3}$kgm^{-1}s^{-1} for water. In the case shown (Figure 1.5) this equates to a value of 3.58×10^{-8} kgs^{-1} for a 1.9 μm bead.

1.4 Introduction to Bacterial Motility

There are many bacterial species, with multifarious morphologies and modes of movement through their environment, that are too numerous to describe here. Therefore I have chosen to deal primarily with the two species of bacterium with which all of my experiments were performed, *E. coli* and *V. alginolyticus*, and to compare them in certain cases with the *Rhodobacter sphæroides* cell. All three of these species swim by rotating flagellar filaments, however the positions, shapes, numbers and modes of rotation of these filaments differ between the species.

1.4.1 *E. coli*

In the case of the ∼2 μm long and ∼0.8 μm diameter *E. coli* cell, an average of six helical flagellar filaments between 5 and 10 μm long and ∼20 nm in cross-section are expressed around the cell body. Each of these filaments is coupled to a single 50 nm diameter rotary motor embedded in the cell wall by a flexible 55 nm hook structure which behaves as a universal joint.
The proton driven flagellar motor of *E. coli* is able to rotate flagellar filaments at speeds in the region of 150 Hz [26] and to switch rotation direction within 1 ms, while generating the same level of torque in either direction [51].

Motility and Control

Under conditions of forward swimming, during which the flagellar motors rotate counter-clockwise (CCW) as viewed from the distal end of the filament, the multiple flagella form a bundle of helices behind the cell body, propelling the bacterium through its surroundings. Each of the filaments in the bundle is able to slip easily against its neighbours in the bundle [30].

Motors are able to switch direction independently [52] and in so doing will extract their flagellar filament from the bundle, causing the swimming direction of the cell to be deviated. It was previously thought that all of the motors in a cell rotated in the same direction, such that the flagellar bundle would fly apart and cause the cell to tumble upon motor reversal. Independent switching was shown by high speed video recording of fluorescent flagellar filaments and showed single flagella extracting themselves from the bundle.

The switching process is triggered by the response of the chemosensory system to the concentration of attractants or repellents. The signal to switch from CCW to CW rotation comes from the phosphorylated form of the CheY protein [53],

CheY-P binding to the internal face of the FliG, FliM and FliN switch complex of the rotor (Section 1.4.7) which, it is postulated, causes a conformational change at the C-terminal of FliG, reversing the direction in which force can be applied to the rotor [54, 55]. The chemosensory system effectively has a brief memory of the order of seconds, allowing temporal comparison of current conditions with previous conditions. If the comparison shows that the cell is moving towards an attractant or away from a repellent the rate of switching for the motor is biased so that the cell tends to continue in forward motion and vice versa. Motion driven by CCW motor rotation, although significantly deviated by brownian motion if it continues for much longer than a second, takes the cell in a roughly constant direction, while CW rotation causes the cell to tumble and randomly reset its direction of travel.

By this means the cell proceeds along a biased random walk, which takes it towards the attractant or away from the repellent. This process is known as chemotaxis. Other forms of taxis are exhibited by certain species of bacteria, including phototaxis and magnetotaxis.

Motor Torque

The torque-speed relation for the proton-driven flagellar motor has been derived in whole or in part by several techniques [31, 38, 56, 33, 57], all of which reveal a characteristic curve (Figure 1.6).

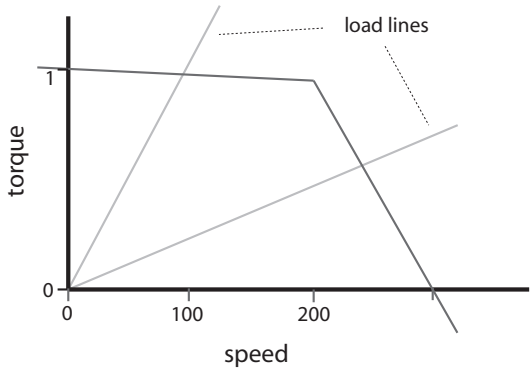

Figure 1.6: The generic torque-speed relation derived for the proton-driven motor. At room temperature, torque is roughly constant all the way from -100 Hz to a knee point around 200 Hz. Above 200 Hz the torque falls off in an approximately linear fashion to a zero-torque rotation rate of around 300 Hz. Load lines are shown for the purposes of introduction. A specific viscous drag load will require a torque proportional to the rotation rate in order to rotate. Thus knowledge of the drag coefficient of the rotated body will give the gradient of the load line and allows the calculation of the instantaneous torque for a given rotation rate.

The knee-point and subsequent drop in high-speed torque for this curve suggests that internal chemical rates in the torque-generation mechanism limit the high speed rotation rate. The temperature dependence of the knee point and the the high-speed zero-torque interecept - both of which increase with temperature - and the temperature independence of the stall torque indicate that this is the case. The accepted value for stall torque is around 4000 pN nm.

1.4.2 *E. coli* Structure

The following is a summary of the most relevant structural information derived from the collected research of Neidhardt and many others [58, 59]. The purpose of it is to consider possible factors relevant to motor assembly and function, and to discover the types of variables, over which we have very little control, that may directly affect the rotation of the motor.

The cell envelope of a Gram-negative cell is constructed in several distinct layers. The outer layer of the cell envelope which encloses the entire cell, a periplasmic space formed on either side of the structural peptidoglycan layer and the inner membrane which encloses the cytoplasm.

The two leaflets of the outer membrane are differently composed. The outer leaflet which is in contact with the environment consists predominantly of lipopolysaccharides. These are composed of proximal hydrophobic lipid A regions, which are extremely rich in charged groups, distal hydrophilic polysaccharide regions which project into the medium and intermediate polysaccharide regions. The overall stability of the membrane is greatly enhanced by the lateral interaction between the lipopolysaccharides which are very strong in the presence of divalent cations which neutralise electrostatic repulsion between them ([58] ch. XX).

The inner leaflet of the outer membrane consists of simpler phospholipids, with 8% of the inner surface area taken up by 7×10^5 lipoproteins per cell, one third of which exist covalently bound to the peptidoglycan, while the others exist as free proteins. This protein aggregates in trimers and functions to stabilise the outer membrane to the peptidoglycan against osmotic pressure ([58] ch. XX).

Inset into the outer membrane are porins, which form non specific channels for small hydrophilic molecules across the outer membrane. The outer membrane is approximately 8 nm in cross section.

The periplasmic space, some 7 nm or more across, is best considered as several microenvironments, formed on either side of the peptidoglycan by the inner and outer membranes. Polysaccharides and small molecules in the periplasmic space

serve to buffer the cell against changing osmotic and ionic conditions of the environment ([58] ch. XX). The periplasmic volume and osmolarity respond to changes in the osmotic strength of the external medium and the osmolarity of the periplasm can be mediated in part by the synthesis of membrane derived polysaccharides and their export to the periplasm. These 2400 Da branched glucose molecules with a charge of -5 e create a Donnan equilibrium of up to 30 mV across the outer membrane, thereby affecting the ionic concentration of the periplasm ([58] ch. XX).

The peptidoglycan layer, which constitutes the stress-bearing part of the cell wall, forms a 2 to 3 nm thick framework for the cell. This consists of long parallel strands of peptidoglycan which run perpendicular to the axis of the cell and bear the circumferal tensile load exerted by osmotic pressure, which is roughly twice the axial tensile load. These rings of pedtidoglycan are cross-linked to their neighbours by their peptide side chains. The separation between rings of peptidoglycan is $\sim$1 nm. Peptidoglycan is synthesised by the action of about 100 enzymes inside each cell, which move unidirectionally around the circumference of the cell with a cycle time of approximately 8 minutes. These enzymes synthesize peptidoglycan strands as they go and splice them in between existing strands, thereby extending the length of the cell body ([58] ch. XX). The intracellular pressure borne by the outer-membrane and peptidoglycan is osmo-regulated by the cell to a constant 300 kPa (3 atm.), however it can rise to 640 kPa under osmotic shock conditions without rupturing the outer membrane and causing plasmolysis ([58] ch. XX).

The $\sim$6 nm thick inner membrane is separated from the peptidoglycan layer and cannot support an osmotic gradient; hence the periplasm and cytoplasm are iso-osmolar and therefore isobaric. The osmotic gradient is maintained between the periplasm and the external environment. The cytoplasmic membrane contains all of the apparatus reqired to generate and maintain the proton motive force (pmf) which is used to drive many energetic processes in the cell ([58] ch. XX).

Protein diffusion rates around the inner membrane have been measured as 3×10^{-10} cm^2 s^{-1} for a 100 kDa protein, implying a membrane viscosity of 2.9 P, a figure higher than the 1 P idealised value often used for diffusion estimates ([58] ch. XX).

The transfer of proteins and lipopolysaccharides between their sites of manufacture at the inner leaflet of the cytoplasmic membrane and their final location in the outer membrane does not take place via the periplasmic space. Further to this there is rapid exchange between the phospholipids of the inner leaflet of the outer membrane and those of the cytoplasmic membrane. Inner and outer membranes

have been observed to fuse together at between 200 and 400 pointlike sites, covering about 5% of the total surface of the cell and it is postulated that the exchange occurs at these sites. These are known as Bayer fusion sites ([58] ch. XX). Whether the peptidoglycan is continuous through these fusion sites, or forms a boundary around them is unknown, but their approximate diameter is in the region of 50 nm.

Below is a table of collected vital statistics for *E. coli* [84, 58, 52].

Dimension	Average (μm)
Cell width	0.8-1
Cell length	2-3
Flagellum diameter	0.02
Flagellum length	up to $\sim$10
Flagellar helical pitch	2 - 2.5
Radius of helix	0.4 - 0.6

1.4.3 *E. coli* Energetics

The proton-based energetics of *E. coli* are well understood, with the extrusion of protons coupled to respiration generating a constant inwardly directed membrane potential ($\Delta\Psi$) in the region of -120 mV while the pH difference between the closely maintained cytoplasmic pH (7.6 to 7.8) and the external medium contributes an extra $(2.3kT/e)\Delta$pH, where k is the Boltzmann constant, T is absolute temperature and e is unitary charge. In a neutral medium this contributes an extra -50 mV.

It is instructive to consider the steady state leakage of protons through the cytoplasmic membrane, which has a conductance of 10^{-6} S cm^{-2} [58]. For a canonical cell with a pmf around 170 mV this implies a leakage current into the cell of the order of 10^4 protons per second. Interestingly, the canonical cell with an internal pH of 7.5 would be expected to contain 10 free protons, which goes some way to indicating the extent of the intracellular buffering. Furthermore, given that there are many thousands of proton exporters around the cytoplasmic membrane each pumping out hundreds of protons per second, this leakage current is insignificant.

The sodium based energetics of the cell which are relevant to the experiments of Chapters 4 and 5 are not so well understood. What is known is discussed in Section 4.1.

1.4.4 *V. alginolyticus*

The *V. alginolyticus* cell is a 2 to 3 μm long comma-shaped bacterium, native to a seawater environment. In conditions of free swimming the cell expresses a single helical filament around 5 μm long at one of the poles of the cell. This is rotated by a sodium-driven motor [60], with similar dimensions and considerable homology to the motor of *E. coli*. This motor differs from the proton-driven motor in its rotation rate. The average speed of a rotating flagellum is 600 Hz [61] and flagella have been seen to rotate at 1700 Hz at 37°C [35].

Wild type strains of the cell are also known to express many lateral flagella around the surface of the cell which are driven by proton motors in conditions of high viscosity, to allow them to crawl on a surface [62, 63]. The sensory trigger for this expression is not known.

Motility and Control

Chemotactic response of the *V. alginolyticus* cell driven by its polar flagellum is similar to *E. coli*. CCW motor rotation drives forward swimming and CW rotation pulls the cell backwards along a curved path. This again is in response to chemotactic signalling in the cell via CheY. In the case of the lateral flagella, the chemotactic response to a repellent appears to be stopped rotation as opposed to reversed rotation of the proton driven motors [64].

V. alginolyticus Vital Statistics

Below is a table of vital statistics for the YM42 *V. alginolyticus* strain, determined by transmission electron microscopy (TEM) [35].

Dimension	Average (μm)	σ (μm)
Cell width	0.80	0.09
Cell length	1.92	0.46
Flagellum diameter	0.032	0.004
Flagellum length	5.02	1.15
Flagellar helical pitch	1.58	0.14
Filament length per turn	1.82	0.16
Radius of helix	0.14	0.02

The ratio of forward swimming velocity v to flagellar rotation rate ω indicates the distance travelled per flagellar rotation. This ratio did not vary with temperature

and was 0.113 μm ($\sigma = 0.021$ μm). Given that the flagellar helix pitch is on average 1.58 μm ($\sigma = 0.14$ μm), this implies that the cell progresses by 7% of the helical pitch, per rotation of the flagellum. The highest flagellar rotation rate observed was $\omega = 1660$ Hz at 35°C, whilst the highest swimming speed observed was 147 μm s^{-1}. It is worth noting that the cell with the highest ω was not also the fastest swimmer. There appeared to be a saturation in v with respect to ω, with v tending to increase with increasing ω in the range below 1000 Hz and tending to remain constant for all $\omega > 1000$ Hz.

At the time of commencing experiments for Chapter 3 the only torque values quoted for the sodium driven motor were hydrodynamically derived estimates in the region of 1000 pN nm at stall [35]. Since then, and simultaneous with my work, a torque-speed relation has been derived [65], which will be discussed later (Chapter 3).

V. alginolyticus Structure

Apart from the flagellar and motor differences already mentioned, the gram-negative *V. alginolyticus* cell is assumed to have a physical structure similar to that of *E. coli* (Section 1.4.2).

1.4.5 *V. alginolyticus* Energetics

The energetics of the *V. alginolyticus* cell are broadly understood, although the extent and variety of some of the systems involved remain unknown. In conditions of near neutral pH a membrane potential is generated by the respiration linked extrusion of protons from the cytoplasm and Na^+/H^+ antiporters are used to regulate the internal sodium concentration. Thus the sodium energetics tend to be secondary. However, in alkaline conditions [66], or when the proton-dependent membrane potential has been collapsed using a proton conductor such as carbonylcyanide *m*-chlorophenylhydrazone (CCCP), the cell is able to generate a membrane potential purely by pumping sodium ions out of the cell as a direct result of electron transport. The membrane potential ($\Delta\Psi$) is measured to equilibrate around -150 mV, independent of the generating ion [67]. This potential, combined with the chemical potential caused by the difference in sodium concentration across the cytoplasmic membrane generates the sodium motive force (smf) which drives many inwardly directed processes in the cell. The extent and mechanism of intracellular sodium buffering is unknown, but the 10 mM internal sodium concentration for the cell

(C.J. Lo, personal communication) suggest there are 10^5 times more free sodium ions inside the cell than there are free protons in *E. coli*.

1.4.6 *Rhodobacter sphæroides*

In contrast to the relatively rigid flagellar filaments of the other two species, the *Rhodobacter* cell expresses a single subpolar flagellum whose relaxed form appears to be a helix with a large radius and very short pitch. When rotated, the viscous drag of the solution reshapes this into a helix similar in shape to those of other species. The motor which rotates this filament appears to be able to rotate in both directions, but a single rotation direction is specific to the individual cell. Rather than switching direction, this motor alternates between spinning and stopped states. The relaxation of the filament from the long functional helix to the large radius short pitch conformation when the motor stops, causes the cell body to tumble in its random walk [68, 69]. Further to this, the FliG protein of *Rhodobacter* which forms the site of torque generation on the rotor has been shown to support bi-directional rotation when inserted into flagellar motors of *E. coli*. This implies that the directionality is a feature of the stator rather than the rotor [70].

1.4.7 Filament and Motor Structure

The assembly and structure of the rotor and filament have been investigated in great detail and the sequence is well documented [71]. The positions of proteins comprising the motor have been shown as a guide (Figure 1.7). The reason behind the choice of site for a motor to incorporate into the cell envelope is unknown, but the remainder of the process is understood.

Beginning with the ∼40 nm diameter MS-ring, sited in the cytopasmic membrane, an export apparatus is expressed, which localises at the inner face of the MS-ring, and the C-ring is assembled. The FliG component of the C-ring is assembled with about 25-fold symmetry [54] around the MS-ring and the FliM and FliN components non-specifically associate to the C-terminal end of the FliG to form the lower portion of the C-ring. This has a ∼34-fold vertical symmetry [72, 73]. At this point the torque-generation interface and the switch mechanism of the rotor are constructed. Simultaneously the ∼10 to 12 stator units [51] which couple torque to the motor may be expressed in a wild-type cell. The assembly of these is not fundamental at this point in the process, as is described below. The export apparatus proceeds to convey a sequence of proteins through the centre of the rotor. These

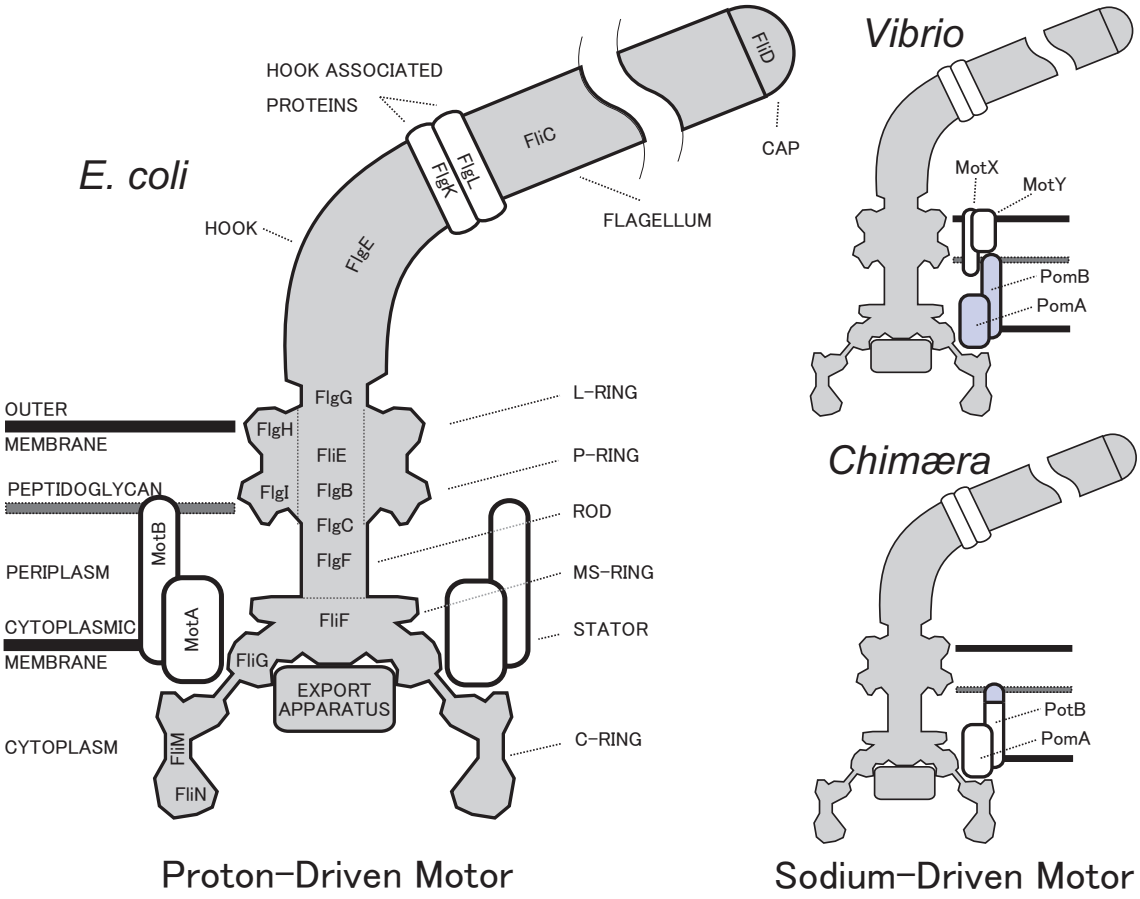

Figure 1.7: A cross section through the proton driven flagellar motor is shown (left). Torque is generated by the interaction between the stators (a single stator appears to be a multimer containing 2 MotB and 4 MotA proteins) and the ∼25-fold repeat of FliG around the rotor. The stator units of the sodium-driven *V. alginolyticus* species differ from those of the proton-driven motor (top-right). The stator complex consists of an outer membrane pair, MotX and MotY, whose function is unclear (They may function as a sodium ion channel, a viscosity sensor, a bearing for high speed rotation or a stabiliser to the torque-generating PomAPotB). Force is generated by the PomA and PotB stator proteins which have considerable sequence homology to MotA and MotB. Chimæra stators have been made using the fused peptidoglycan binding motif of MotB with the remainder of PomB - aptly named PotB - and PomA (bottom-right) which drive the rotation of the flagellum of an *E. coli* host cell using sodium ions.

proteins, sometimes with the aid of chaperone proteins, self assemble into the rotor rod and L-ring and P-ring bushings. The rotational symmetry of the rod is 11-fold [74].

Once the rod is assembled, the export of hook proteins begins. These assemble into a hollow, flexible, curved cylinder built from 11 adjacent cross-linked strands of FliE which can pack in either a long or short conformations [74]. This lends the flexible hook curvature and allows it to act as a universal joint between the rotor axis and the axis of rotation for the flagellum. The torsional spring constant of the hook has been measured as 500 pN nm rad^{-1} [75]. The length of the hook is tightly controlled to 55 nm [76].

With the hook assembled, two hook associated proteins (HAPs) are located on the end of the hook and the export of the FliC proteins that form the comparatively rigid flagellum begins. A cap on the end of the filament guides newly arriving FliC to the next available site for polymerisation [77] on the end distal end of the filament. The final length of the flagellar filament is somewhere in the region of 5 μm. Typically the pitch of the flagellar filament is roughly 2 μm with a helical radius between 0.4 and 0.6 μm in *E. coli* [58].

Proton-driven Stators

The stators of the proton-driven motor are assembled from multiple copies of two proteins, MotA - which has four membrane spanning domains and large cytoplasmic loops - and MotB - which has a single membrane spanning domain and a periplasmic domain with a peptidoglycan binding motif at the end. The accepted structure of a single stator unit has two MotB, peptidoglycan-binding proteins, arranged back-to-back, with four MotA proteins arrayed around the membrane segment of the MotBs [78, 71] (Figure 1.8). These are postulated to assemble into the complete $(\text{MotA})_4(\text{MotB})_2$ multimer before integrating to the motor.

The combination of membrane and cytoplasmic segments of the proteins (2/3 of MotA lies in the cytoplasm) presents significant problems to protein crystallographers and the precise structure remains unknown. What is known of the structure has been inferred from the sequence and from cross-linking studies between the components of the stator [79, 80]. It is believed from these structures that a single stator forms two ion channels between each MotB and the two MotAs closest to it.

The transit of ions across the stators, driven by the pmf, has been related to rotation by measuring the change in proton flux into the cell with the motor rotating and with motor rotation abruptly stopped [30]. The proton flux into the cell showed

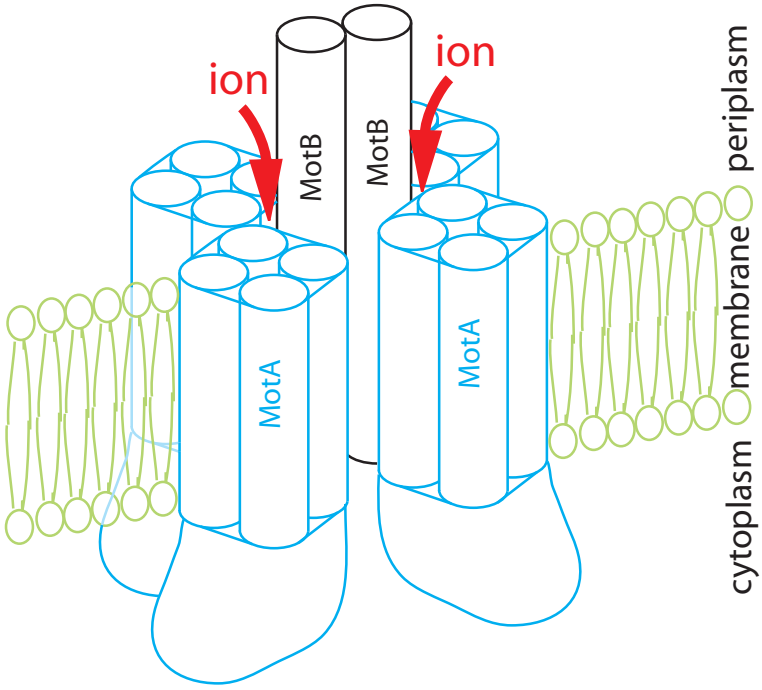

Figure 1.8: A single stator unit consisting of two peptidoglycan-binding MotB proteins, each with a single membrane spanning domain, and four MotA proteins, each with four membrane spanning segments, has been inferred to assume the structure shown. The two MotBs arranged back-to-back, with four MotA proteins arrayed around the single membrane spanning segment of the MotBs, are postulated to form two ion channels [78] as shown. How the cytoplasmic regions of MotA interact with FliG to couple torque is unknown.

a tight-coupled relation with the transit of ∼1200 ions per revolution across the stator units of the motor. This constitutes approximately 2% of the total proton energetics of the cell [81].

Further functional parts of the stator and rotor were identified by a mutational analysis of specific charged residues on the FliG, MotA and MotB proteins [82, 83]. These studies found three charged residues near the C-terminus of FliG, Arg281, Asp288 and Asp289 which were of primary importance in torque generation. Positionally these are arranged around the edge of the rotor. The Arg90 and Glu98 residues of MotA were also found to be functionally important, with the charge being fundamental. Neutralisation or reversal of the charge at these sites on either rotor or stator severely impaired the swimming of these cells, suggesting that there is an electrostatic interaction between rotor and stator. Equally it could simply affect the conformation of the proteins which may impede rotation any if torque is coupled by a steric interaction between these domains. Mutational changes also revealed that the Asp32 of MotB and Pro173 of MotA, both of which are sited near to the

cytoplasm and are relevant to the ion channel function of the stator, are essential for torque generation. It is postulated that torque is generated by the stator through a conformational change in response to the protonation and deprotonation of the Asp32 site [78].

Stator units are known to function independently. The motor of a MotA and MotB deletion mutant was paralysed and torque generation was restored by the production of stators from a plasmid in response to an inducer (Appendix C.2). The high-load torque increased in steps of equal size, implying that the individual stator units function independently and contribute equal torque [51]. This process has been termed 'resurrection.'

The duty-cycle for stators is required to be very high. This can be demonstrated by a simple thought experiment [84]. Given that a single stator will rotate a high load, such as a tethered cell, at 1 Hz with a torque of ∼400 pN nm and taking into account the torsional stiffness k of the flagellar hook (Section 1.4.7) of around 500 pN nm rad^{-1}, under steady rotation the hook will be wound up through nearly 1 rad (θ_0). Any time during the rotation that the stator spends detached from the rotor will allow the hook to relax. Since the angle θ during relaxation relates to the time t by $\theta = \theta_0 e^{-\frac{k}{f}t}$, where f is the drag coefficient for the rotor embedded in the cell wall (estimated as 2×10^{-2} pN nm rad s^{-1}), any very short time spent off the rotor would see a significant relaxation of the rotor in relation to the stator, meaning that the cell body would never rotate. This implies that the duty cycle must be very close to 1.

Sodium-driven Stators

The stator units of the sodium-driven *V. alginolyticus* species differ from those of the proton-driven motor (Figure 1.7 (top-right)). The stator complex consists of an outer membrane protein pair, MotX and MotY, and the PomA and PomB stator proteins which have considerable sequence homology to MotA and MotB. The function of MotXMotY is unclear. They may function together as a sodium ion channel [85, 86], a viscosity sensor to trigger the expression of lateral flagella for crawling on surfaces [87], a bearing for high speed rotation or even a mechanical stabiliser and/or ion specifier to the torque-generating PomAPomB [88]. The assembly and torque-generation processes are assumed to be the same in the sodium-driven motors as in the proton-driven stators. Powering ion specificity has been proved by motor inactivation in the presence of sodium channel inhibitors [25] and lithium has been shown to power relatively slower motor rotation when substituted for sodium. No

other ion drives motor rotation [89].

Chimæra Stators

A recent development, which justifies the assumption that the torque-generation process is independent of the powering ion, is the production of chimæric motors. Many hybrids across species have been constructed. Rotors of cells with naturally sodium-driven motors can be rotated by protons using stators from proton-driven species and vice versa, and stator ion specificity can be converted by using segments of different stators [90, 91, 92]. A sodium-driven chimæra motor (Appendix C.2) was used for the experiments of chapters 4 and 5 (Figure 1.7 (bottom-right)). The peptidoglycan binding motif of MotB fused to the membrane portion of PomB, together with PomA, form stators which bind at the rotor in an *E. coli* background cell and rotate the motor using sodium as the powering ion.

Bacterial Strains Used

The strain history, and growth conditions for all bacterial species used in my experiments are listed in Appendix C.2.1.

1.4.8 Models for Motor Rotation

Many models for flagellar motor rotation have been postulated, both kinetic and mechanistic. An electrostatic turbine model, where tilted lines of charge on the rotor couple the passage of an ion through the stator to generate torque [93] has been created, as have turnstile mechanisms [94] and stepping crossbridge mechanisms [33] (Figure 1.9).

To a greater or lesser extent these models can reproduce the characteristic torque-speed relation for the motor, but how closely the fundamental mechanism of the model relates to those taking place in the motor remains unknown. Without a known protein structure for the stator units, there is little that can be stated in detail about the nature of the force generating mechanism and the interaction between stator and rotor proteins. That being said, the evidence points to the stator units performing independent high duty-ratio poisson stepping around the rotor [95, 96].

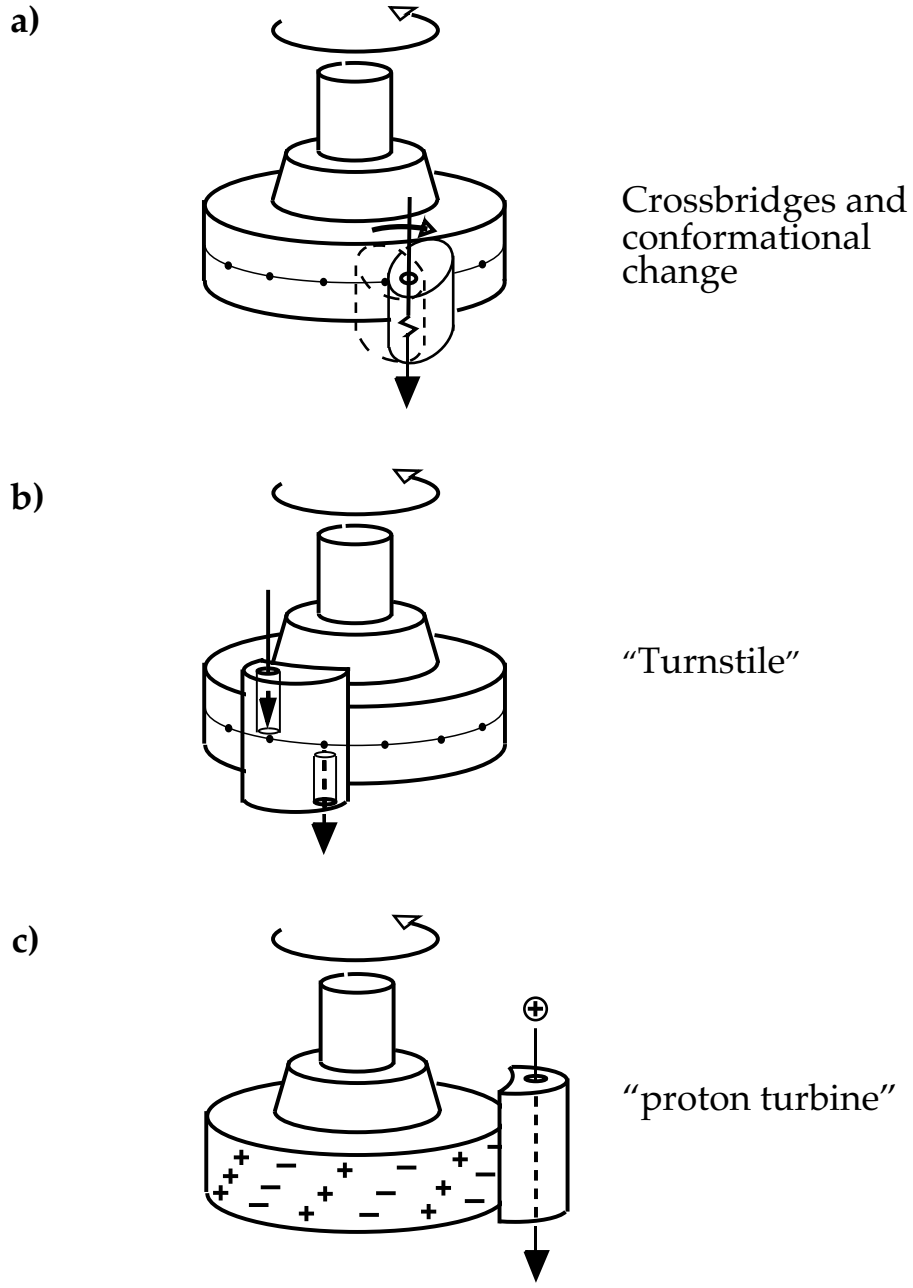

Figure 1.9: The three competing models of motor rotation are shown. (a) The most recent crossbridge stepping model couples the transit of an ion or several ions to a conformational change in the stator which applies torque to the rotor. The stator is required to step around the rotor to an adjacent binding site to complete a single cycle of torque generation. (b) The early turnstile mechanism proposed the arrival of an ion at a half channel in the outer face of the stator. Progress of the rotor would then pass the ion into another half channel which openned into the cytoplasm. This mechanism allows for the tight coupled relation between rotation rate and ion conduction. (c) The proton turbine in which tilted lines of charge on the rotor electrostatically interact with an ion as it passes through the stator to generate torque. Figure reproduced with permission of R. Berry.

Chapter 2

Techniques and Novel Applications

2.1 Laser Trap

The laser trap on which all of the experiments described in this thesis were conducted is a home-made[1] single beam, single focus 1064 nm wavelength laser trap. By current standards this is a simple experimental setup.

This trap was used successfully to measure the high speed rotation of different types of trapped anisotropic particles and later to perform sensitive positional and rotational measurements on a variety of bead assays. Later experiments also superceded BFP position detection with high speed video capture and analysis.
This chapter describes the trap layout and the data acquisition and analysis processes which were employed in each of the three main experiments performed.

The beam from a diode-pumped solid-state laser with 1064 nm wavelength (Elforlight, Northants, UK) is attenuated by a $\lambda/2$ waveplate and polarizer and passed through two beam expanding telescopes to slightly overfill the back aperture of an oil-immersion microscope objective of N.A. 1.4 (CFI plan-fluor 100x, Nikon, Japan). The focussed beam at the image plane forms the trap, (Figure 2.1).

The transmitted beam is re-collimated by a condenser lens, and the condenser back-focal-plane is imaged to fill the surface (78 mm^2) of a quadrant photo-diode (Pin-SPOT 9DMI, UDT Sensors, CA, USA). The photo-current from each quadrant is amplified using a home-made current-to-voltage amplifier and is sampled at up

[1] A detailed HOWTO for building and aligning an optical trap is included in Appendix A.

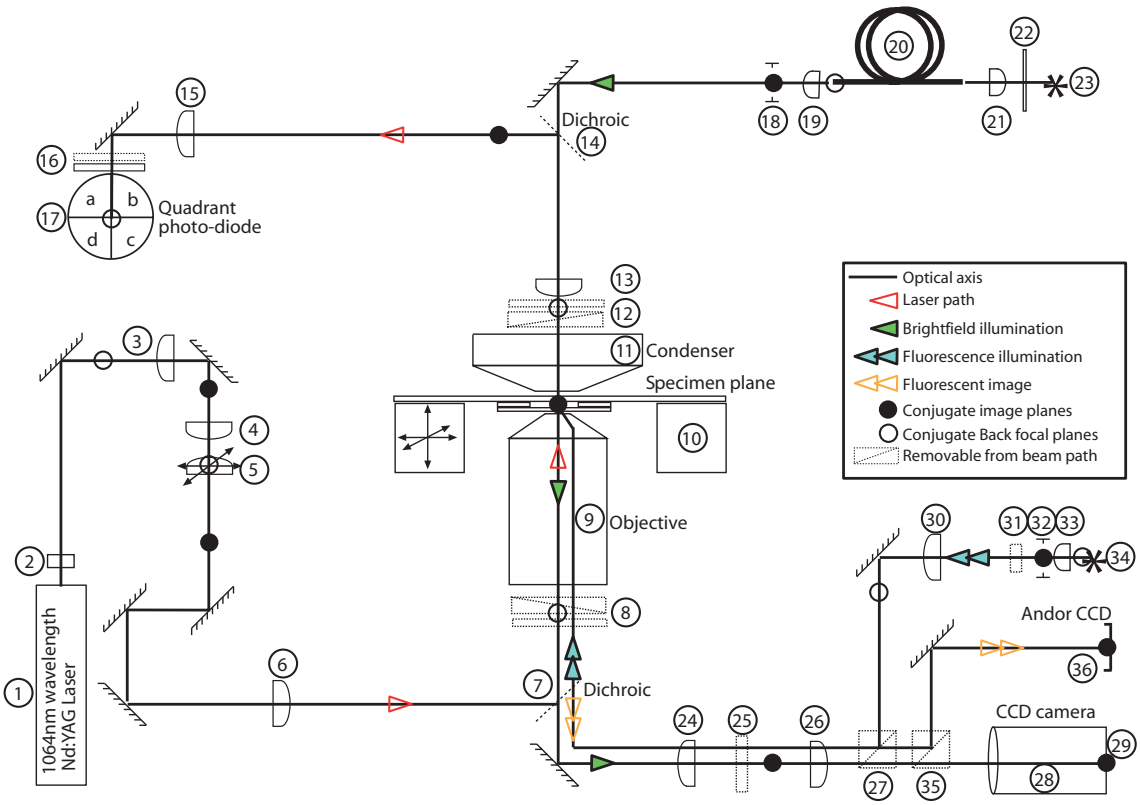

Figure 2.1: Anatomy of a laser trap. A 1064nm laser beam, broadened and steered into the back aperture of an oil-immersion microscope objective of N.A. 1.4 forms the optical trap. The transmitted beam is re-collimated by a condenser lens and projected onto a quadrant photodiode to form a position detector. Illumination for bright-field or DIC imaging is provided by a fibre-coupled tungsten halogen bulb. Illumination for fluorescence is provided by a mercury arc lamp. Solid circles mark planes conjugate to the optical trap, open circles mark planes conjugate to the back-focal-plane of the objective. The trap is steerable by moving lens (5). Components: (1)- Laser. (2)- Attenuator. (3)&(4), (5)&(6), (13)&(15), (24)&(26), (30)&(33)- Relay telescopes. (7), (14)- Dichroic mirrors. (8), (12)- Wollaston prism and polarizer pairs for DIC. (9)- Objective lens. (10)- Piezo-electric stage. (11)- Condenser. (16)- Long-pass and ND filters. (17)- Quadrant photodiode. (18)- Field iris. (19), (20), (21)- Fibre and coupling lenses. (22)- Short wavelength blocking filter. (23)- Tungsten halogen bulb. (25)- IR blocking filter. (27)- Filter cube. (28)- Zoom lens. (29)- CCD camera. (31)- ND filter. (32)- Field iris. (34)- Mercury arc lamp. (35)- Optional mirror. (36) 128x128 pixel Andor high speed video camera.

to 5 kHz by a PC, using National Instruments hardware inputs. A long-pass filter (cut-off 1000 nm) is placed in front of the diode to block ambient light and a neutral density filter (ND 1) is added when the laser would otherwise saturate the diode.

Tungsten halogen illumination for bright-field or DIC imaging is filtered to remove short-wavelength light that damages biological specimens, and introduced via a multi-mode optical fibre.

Epi-fluorescence illumination from a mercury arc lamp (Nikon, Japan) is introduced when required via a fluorescence filter cube (XF-108, Omega Optical, VT, USA). The brightfield image is projected onto a CCD video camera by a zoom lens and fluorescence emission images are filtered onto a high quantum efficiency 128×128 pixel Andor Ixon high speed video camera which records directly to the controlling computer.

2.2 Rapid Rotation of Slightly Anisotropic Particles

As a proof of principle for a techniques paper [32] and as an aside to the main experiment of Chapter 3, 1 μm diameter latex beads were hydrophobically associated with several 0.2 μm beads to produce large beads with a few small "decorations" (See Figure 2.2(a)). These beads were held in the trap and electrorotated to over 1 kHz. The rotational peak in the power spectrum inset to the figure is clear evidence for the viability of simultaneously trapping and recording a rotating particle. The experiment designed for Chapter 3 depended upon this rotation detection working for trapped *V. alginolyticus* cells, shown in Figure 2.2(b) oriented vertically in the trapping beam. Depending on whether the cells entered the trap from above or below, they tended to sit tail up and tail down respectively.

It is unlikely that the filament itself, which is only 30 nm in diameter, generates the rotation signal.[2] Most probably it is the small lateral deflection of the cell body caused by any non-integer turn of the flagellar filament during rotation which is being detected (Figure 2.3(a)).

[2]This is not entirely clear as I found it was possible to move a cell - which had spontaneously immobilised by its body to a surface - around in the focus of the trap and to get a weak but unmistakeable flagellar rotation signal. This was the exception rather than the rule and it is quite possible that the cell body was able to move enough to contribute the signal.

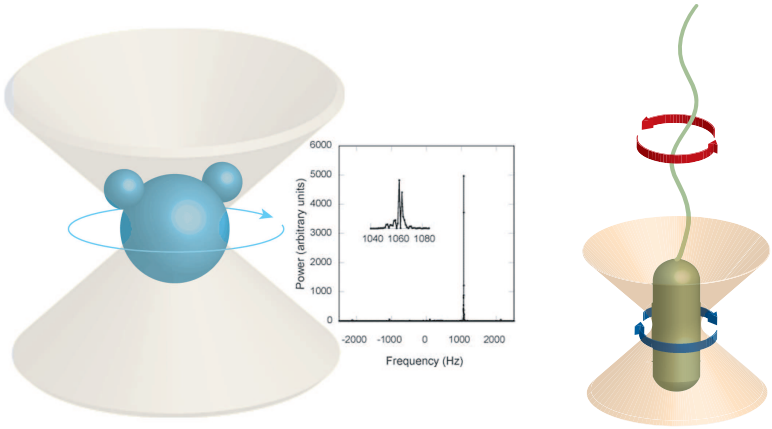

(a) Rotating anisotropic bead.

(b) Trapped *V. alginolyticus*.

Figure 2.2: (a) Large decorated beads were held in the laser trap and electrorotated at speeds in excess of 1 kHz. The power spectrum of the BFP signal can be seen inset, showing 1060 Hz rotation. (b) *V. alginolyticus* cells held in the trap oriented with the long axis of the trap. There is sufficient anisotropy in the oppositely rotating cell body and flagellum to generate rotation signals for both.

2.3 Automated Detection of Trapped Cell Rotation

For straightforward measurement of flagellar rotation rates, *V. alginolyticus* cells were diluted to a density of approximately 10^7 cells per ml and added to a flow chamber constructed from a microscope slide, double-sided sticky tape and a coverslip.

In media containing high concentrations of sodium, fast-swimming cells were allowed to swim into the trap. In low concentrations of sodium, slow-swimming cells were moved into the trap by manually moving the microscope stage. Using the audio signal available, a swift assessment of the amplitude and frequency of the rotation signal for each cell could be made. Cells that were poorly motile or that otherwise failed to give a strong signal were released by shuttering the trap laser. Analysing large amounts of data for a trapped cell by taking the complex power spectrum presented difficulties with automation. It was not trivial to create a reliable algorithm that picked out the two frequency peaks for flagellar rotation and body roll, particularly given that the flagellar signal often fell beyond the corner frequency of the trapped cell body.[3] Thus any algorithm which selected the highest power above and below a certain frequency threshold invariably picked out the

[3]See Figure 1.5 for the corner frequency of a weakly trapped bead by way of comparison.

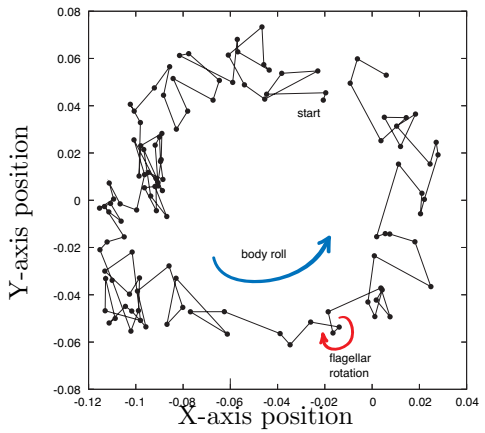

(a) *V. alginolyticus* position sampled at 2 kHz.

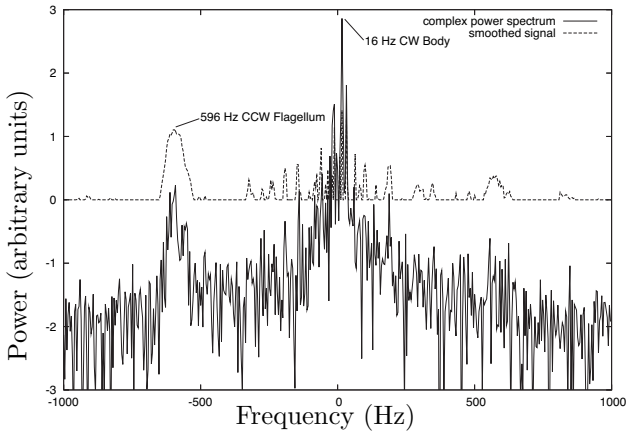

(b) Complex power spectrum of *V. alginolyticus* signal.

Figure 2.3: (a) Shows 116 consecutive samples at 2 kHz of the positional signals P_x and P_y plotted against each other. The large slow (16 Hz) CCW trace of the body roll indicates a cell held tail down in the trap, while the smaller faster (596 Hz) CW signals (confused by the convolution with Brownian motion but clear in many places) demark the lateral movement of the cell on account of flagellar rotation. (b) Shows the raw complex power spectrum and the final smoothed power spectrum from which high speed flagellar and low speed body rotation rates can be read automatically.

threshold value as the fast rotation peak.

The solution to this was to smooth the power spectrum twice, once with a narrow window of constant width in log-space and again with a significantly wider window. Subtracting the wide smoothed data from the narrow smoothed data left the smoothed signal (Figure 2.3(b)). This was reliably split by an algorithm, into body roll and flagellar signals.[4]

2.4 High Angular Resolution Measured with a BFP Method

The flagellar motor stepping experiment of Chapter 5 required a different approach. The bead on stub assay was used throughout, however the detection setup was much more stringently controlled.

When the axis of rotation for a large bead on a stub is centred in a very weak trap, the frequency of rotation is unaffected, but the positional signal is extremely

[4]Plotting flagellar rotation rate vs body roll for a single cell demonstrate a straight line relation. This is to be expected since the torque generated by the motor is equal to the rotational speed divided by the drag coefficient for either the filament or the cell body, so the ratio of speeds is simply the inverse of the ratio of drag coefficients.

circular, giving resolution of the order of nanometres. Small deviation from the centre of the laser focus tends to distort the signal, and further deviation removes any circularity. While this is still sufficient to give a frequency signal, angular resolution is impossible unless the signal is close to circular. Further to this, the low load requirements demand smaller bead labels which degrade the signal-to-noise ratio, such that even a perfectly centred 0.375 μm diameter bead does not give a signal that is sufficient to resolve angle.

To overcome this, three sequential solutions were used. The first was to use beads no smaller than 0.5 μm which minimised load whilst still providing an acceptable signal. The second was to ensure that the signal was as close to circular as possible by only choosing beads that were rotating in a plane as nearly orthogonal to the optical axis as possible. This meant that elliptical distortion to the signal was minimised. A true ellipse could be fitted (a downhill simplex method was the preferred method for fitting (Section 2.6)) to the elliptical signal in order to determine its major axis angle and eccentricity. This could then be used to fit the ellipse onto a circle where necessary. Finally it was sometimes necessary to employ a feedback system between the signal and the piezo-electric stage that accounted for any small thermal drift in the system by regularly centring the time averaged rotation signal on the optical axis. By this means it was possible to follow the angular position of the bead around its axis of rotation at 4 kHz with $\sim$2.5 nm precision, which correlates to about 1 degree of angle.

2.5 High Angular Resolution with Small Fluorescent Beads

In order to resolve greater detail in the angular velocity of the motors at low speed it was necessary to maximise the ratio of flagellar hook stiffness k to bead drag f by reducing the drag load below that of a 0.5 μm bead. This ruled out using BFP detection with 1064 nm wavelength.

The solution we chose to apply was a high speed video camera with 95% quantum efficiency to track the position of 0.2 μm fluorescent beads attached to flagellar stubs.

The frame rate of the camera is traded off against frame size, meaning that to get frame rates above 2 kHz, which was necessary to significantly improve upon the BFP method, our image size was limited. The final optimal choice of a 16$\times$16 pixel image allowed a frame rate of 2350 Hz. However the eqivalent size of a pixel in the image plane was 80 nm.

In order to improve positional resolution, a gaussian intensity distribution function was fitted to the image. Optimal values for the peak intensity I, the width σ, the x-

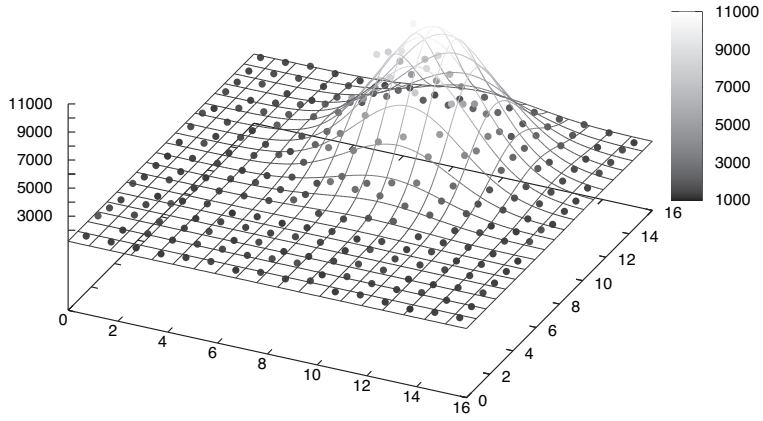

Figure 2.4: The intensities values (filled circles) of the 16×16 array of pixels sampling a rotating fluorescent bead at 2350 Hz frame rate and the simplex fitted optimal gaussian (wireframe) which localises bead position in x and y to 5 nm accuracy.

coordinate μ_x and the y-coordinate μ_y of the central maximum and the background intensity B, were obtained by a simplex fit to the function

$$f(x,y) = \frac{I}{2\pi\sigma^2} \exp\left(-[(x-\mu_x)^2 + (y-\mu_y)^2]/2\sigma^2\right) + B. \tag{2.1}$$

This allowed the centre of the bead to be localised with better than 5 nm precision,[5] (Figure 2.4).

2.6 SIMPLEX FITTING

The Downhill Simplex, also known as a Nelder and Mead method, is best visualised in terms of a two dimensional function.[6] The aim is to minimise a given function by searching through the space in a rational manner.

Given a single starting point, the algorithm generates a simplex and evaluates the function at each of the three points. The point at which the function is farthest from zero is then transposed across the centre of the axis defined by the other two points in the simplex, by a distance weighted by a factor of 0.5, 1 or 2, depending

[5]Determined by the accuracy with which the centre of a 200 nm bead stuck to a surface could be found.

[6]The process scales up to as many dimensions as are required and in each case the simplex consists of a shape defined by the minimum number of points required to define a boundary in the n-dimensional space considered. This number is $n+1$.

upon which new point gives the minimum functional value. Iterating through this process until the function converges on a minimum value results in the definition of a minimum point for the function. Thus in order to fit a function to a data set, the fitting function minimised by the simplex is the error value for the data relative to the function evaluated for each point in the simplex.

The results of the application of these techniques are shown in the following chapters.

Chapter 3

Torque-Speed Relation of the *V. alginolyticus* Motor

3.1 Experimental Aims

The torque-speed relation for the proton-driven motors of *E. coli* has been investigated using several techniques in the recent past [31, 56, 57] (summarised in section 1.3), whereas no detailed measurements had been made on the sodium driven motor of *V. alginolyticus* prior to my present study.

There were two available approaches, the first being to try to apply the relatively standard techniques as used by Chen and others [31, 56, 57] and the second being to develop a new technique entirely.

There were several good reasons not to follow the standard path. Firstly as mentioned in the descriptions of the two species of bacteria (Figure 1.2), the positions of the motors on the cell bodies differ. The multiple motors of *E. coli* are peritrichously[1] arranged around the cell wall whereas the single sodium driven motor of *V. alginolyticus* is situated at one pole of the cell. Optimal rotation measurement using a BFP detection technique[2] requires the plane of movement of the detected body - in this case a small latex bead attached to the stub of a flagellum - to be orthogonal to the optical axis. A peritrichously flagellated cell stuck on its side to a coverslip as in the standard assay (Figure 1.3(b)) has a reasonable chance of having

[1] **Peritrichous**: Having flagella evenly distributed about the body of the cell rather than at one of the poles.

[2] See 1.3.4.

at least one motor rotating in a plane which will provide a good rotation signal. It therefore follows that a single polar flagellum on a cell fixed in the same manner will always rotate in a plane perpendicular to the detection plane. This in itself does not prevent a rotational frequency being detected, however there is no way of being certain that the rotation rate is not hindered either by direct contact between the bead and the coverslip or simply by its proximity.[3] Thus for purposes of rigour it is necessary to be able to detect at least an elliptical signal to be sure that there is no unexpected interference with the rotation. The only way to produce this orientation of the motor with a polar flagellum is to prop the cell body on top of a feature on the surface by some means, a non-trivial technique in itself.

Further reasons against following the standard techniques were that the variation of viscous load on the motor produced by using different sized beads was susceptible to unknown error across cells on account of the uncertainty in the length of the flagellum to which the bead is attached. This is particularly noticeable when using small beads, where the drag of the filament and the bead are comparable.[4] Also, as is apparent from [33], a wide range of bead sizes only give load lines which fall inside a limited sector of the torque-speed curve. The full torque speed curve is best elucidated using electrorotation, as demonstrated by [31], however the arrangement of the polar flagellum[5] again foils this technique and the high ionic strength (300 mM) of the medium in which the cells live also makes this approach unfeasible.

Given all these considerations we chose to try an entirely new approach incorporating laser-tweezers and microfluidics with the aim of subjecting a single cell to several different external sodium concentrations at a constant viscosity, or to several different viscosities at a constant sodium concentration, in rapid succession whilst measuring the rotation rate of the flagellum.

[3]The proximity of any surface to a moving bead will affect the shear flow of the fluid around it in the low Reynolds number hydrodynamic regime, raising the effective drag coefficient. A good approximation is that the drag coefficient is unaffected as long as the particle remains more than its radius away from the surface. Closer approach sees the drag coefficient rise to ~ 3 times its quoted value at the surface [97].

[4]See discussion in 1.3.1.

[5]See 1.3.2 for summary and discussion of electrororation.

3.2 Experiment Design and Analysis

The primary considerations affecting the design of the experiment are as follows:

- *Vibro alginolyticus* generation time and the effect of age on motility of the cells.
- Flow cell dimensions, material and manufacture.
- Loading of flow cell and maintenance of constant flows.
- Maximum experimental flow rates and mixing between channels.
- The effects of laser trapping on the experiment.
- Movement of cell between channels and simultaneous recording of position and motor rotation rate.

These items are discussed subsequently.

3.2.1 *Vibro alginolyticus* Growth and Motility

In order to determine the optimal time to harvest a fresh culture of cells for a day's experiment, a 100 μl frozen stock of the NMB136 strain from an aliquot was inoculated in 3ml of VPG growth medium[6] and grown with shaking at 30°C. At intervals a 200 μl sample was extracted and its Optical Density measured at 700 nm wavelength against a baseline of fresh VPG to determine the cell density at that time[7] (Figure 3.1). Simultaneously a rough estimate of swimming speed and number of motile cells was made by eye, using a microscope. The maximal swimming speed and the range of motility of the population was very dependent upon the age of the culture. No consistent motility was visible within the first hour of growth. After 95 minutes the fastest cell swam at $\sim$30 μm/s with most travelling more slowly. By 135 minutes the fastest cell was travelling at $\sim$50 μm/s with an increased proportion of faster swimmers. After 165 minutes in excess of 50% of the cells were very motile and travelling at maximum speeds in excess of 50 μm/s. Beyond this age motility did not increase and remained consistently high for many hours. A culture stored for 6 hours at room temperature remained highly motile and cultures stored overnight at

[6]For all recipes of growth media and optimised growth protocols see Appendix C.1.2 and following.

[7]Using a Cary Spectrophotometer.

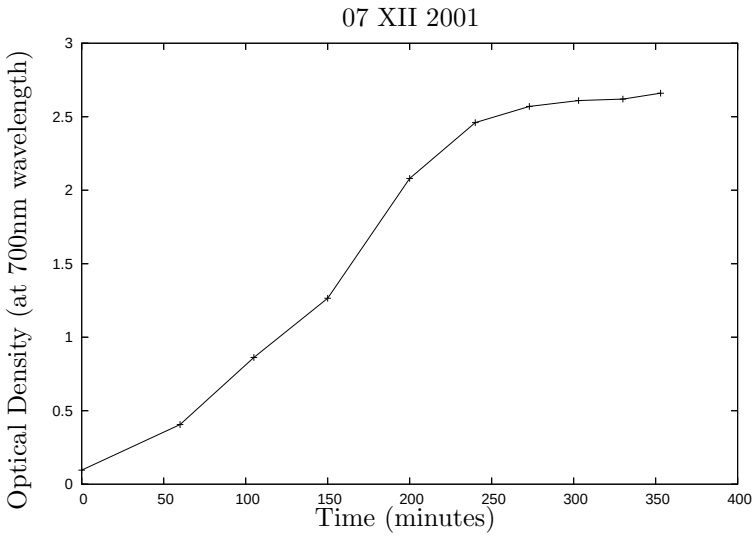

Figure 3.1: Growth curve for *V. alginolyticus* NMB136 strain cultured at 30°C with shaking and measured at intervals against a background of pure VPG growth medium.

4°C would still be reliably motile the next day. In practice, cells would be removed from the incubator after 2.5 hours, during the late log-phase of the growth curve (Figure 3.1) and stored at 4°C for up to an hour before being harvested, washed[8] and resuspended in a motility medium. For all experiments the sodium concentration of motility media used to wash and prepare the cells prior to use was 50 mM, except where otherwise stated.

To extend the range of motor loads measured into the high-speed low-load regime, some of the cells were subjected to "shearing." This refers to the process of repeatedly forcing a freshly harvested cell suspension through a 40 gauge hypodermic needle. The turbulent flow which occurs inside the needle is sufficient to shear the flagella at a random point along the filament. Using low pressure and few repetitions it was possible to get a range of lengths of filament. Heavily sheared cells became non-motile and while there may have been a functional motor present there was insufficient flagellum to generate a rotation signal in the trap, therefore poorly motile cells - due to partial flagellation - recorded the highest rotation speeds.

Sodium Motility Buffers

Motility media were made by combining TMN 300 (pH 7.5 Tris buffer with 300 mM Na^+) and TMK (pH 7.5 Tris buffer with 300 mM K^+) in the correct ratios in order to

[8]See Appendix C.1.1 for full details of harvesting process.

give the correct Na^+ concentration while maintaining a constant ionic strength[9] with K^+. The number following the letters TMN denotes the millimolar concentration of Na^+ in the buffer. Thus TMN 50 is a 5:1 mix of TMK with TMN 300 respectively.

3.2.2 Flow Cell: Dimensions, Materials and Manufacture

The idea we developed to allow us to switch the sodium concentration outside the bacterium as quickly as possible required several adjacent laminar flows with sharp boundaries between them to be delivered to a small flow chamber placed over the laser trap. A cell could then be trapped inside the chamber and moved between adjacent channels whilst measuring its speed of rotation. This system was to be created using home-made microfluidics.

For the microfluidic system to work with the laser trap, its dimensions had to fit the constraints of the existing system (Figure 3.2). A 625 μm wide by 80 μm deep flow chamber was designed to be fed by either five or 11 channels each separated by a 25 μm wide pillar at the entrance to the chamber (Figure 3.3(a)).

Flow Cell Manufacture

The microfluidics and the immediate flow supply network were cast [98] from Polydimethylsiloxane (PDMS),[10] a transparent flexible elastomer, on a silicon master. This original was cut using standard photolithographic techniques in Hywel Morgan's lab at Glasgow University.[11] The master was made extremely hydrophobic by the evaporation of trimethylsiloxane (TMSO)[12] over the surface, ensuring that it was possible to peel the freshly cast flow cell off the surface without damaging any of the fine detail. The elastomer flow cell was then placed onto clean hydrophilic

[9] It is worth noting that not maintaining the ionic strength of the motility buffer can have a catastrophic effect on the cells. This was shown by a test experiment in the flow cells described later in chapter 3. In one channel TMN 5 was replaced by a Motility medium containing 5 mM NaCl and no KCl. Every time a cell was brought into the channel it very rapidly "ghosted" away. The implication of this is that the sudden osmotic shock was causing the cells to swell and rupture, thereby losing their structural integrity and disappearing in the phase contrast image.

[10] Polydimethylsiloxane (PDMS) Sylgard 184 silicone elastomer from Dow Corning, comes as a clear viscous liquid which, when mixed in a ratio of 10:1 with a curing agent, sets into a flexible transparent elastomer. Variation of up to 10% in the amount of curing agent made little difference to the final elastomer, though more curing agent made it slightly harder. Elevated curing temperatures made for slightly harder finished flow cells.

[11] Professor Morgan has since moved to the Department of Electrical Engineering at Southampton University.

[12] This "silanization" process needs to be performed in an enclosed environment inside a fume cupboard due to the extreme volatility and toxicity of TMSO.

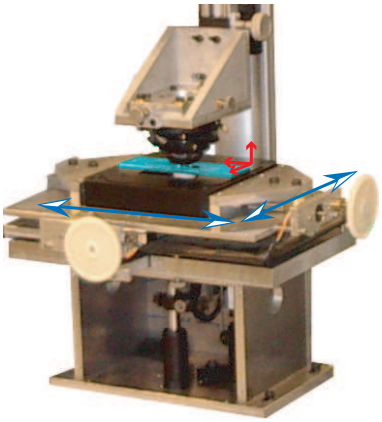

(a) Mounting around the objective lens which forms the laser trap.

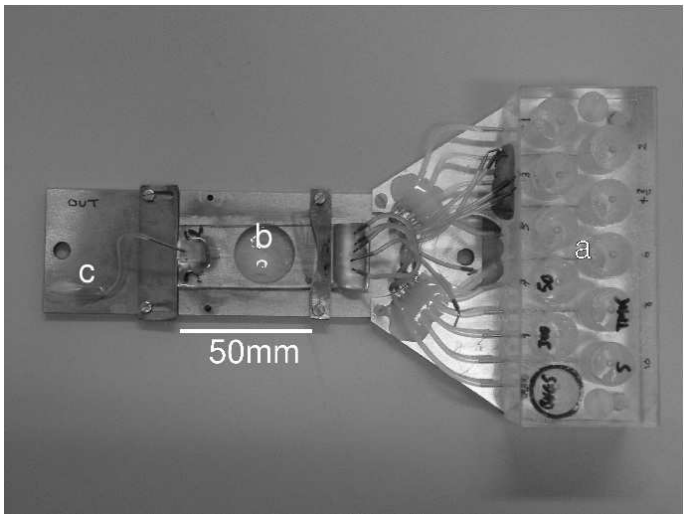

(b) Flow cell on mounting plate.

Figure 3.2: (a) The sample, highlighted here in turquoise, is fixed to the black nanopositioning piezo stage which is in turn carried on a larger metal frame. The piezo stage has three dimensions of movement as shown by the red arrows, with 20 μm vertically and 100 μm in each horizontal axis. The cradle carrying the piezo stage has several centimetres of freedom (blue arrows) in each horizontal direction and is positioned either using stepper motors or by hand with an accuracy of 2 μm. (b) A later generation of the flow cell system. The array of reservoirs, labelled **a**, delivered separate fluids via thin pipes to the microfluidics, **b**, affixed to carrier plate, **c**, which bolts on to the piezo stage to form the sample.

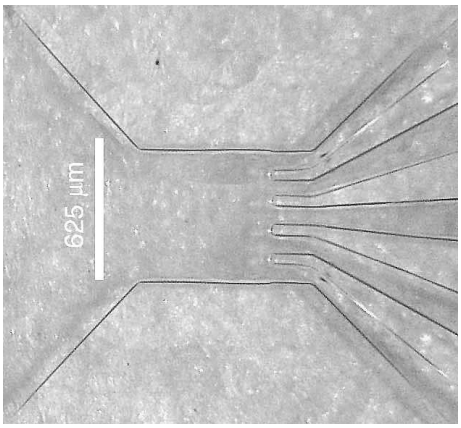

(a) 5-channel flow cell in PDMS detail.

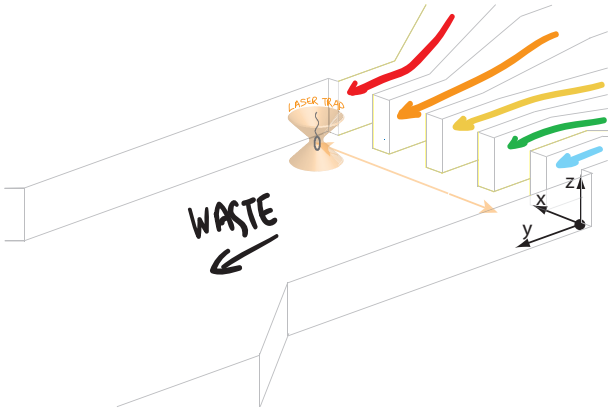

(b) 5-channel laminar flow diagram.

Figure 3.3: (a) Shows an expanded view of region **b** of Figure 3.2(b) with 5 flow channels, entering from the right, delivering fluid to the laminar flow chamber at the centre. (b) Is a diagramatic representation of the 5-channel flow chamber showing a trapped bacterium which can be moved across the mouths of the incoming flows.

glass.[13] I found that the most reliable seal was attained by spreading a very thin (<10 μm) layer of freshly mixed PDMS onto a glass surface and printing the flow cell onto it before placing it on the cover slip. A few seconds on a hot plate at 90°C completed the manufacturing process.[14]

Laminar Flows

There was a multitude of technical problems associated with loading the flow cell, to be overcome in such a way that all the channels flowed steadily and many weeks were spent optimising the system (Appendix B). Suffice to say that given the finite probability of any channel failing to load successfully, the time spent getting an 11-channel flow cell to work properly was considerably greater than for 5 channels. As a result all of these experiments were carried out in 5 channel flow cells.

At this point it is worth clarifying that the flow cell dimensions are appropriate for the function required. For a laminar (Poiseuille) flow to exist the Reynolds number $\mathcal{R}$ must be less than ∼30 at the narrowest point of the channel.[15]
For an arbitrary shape

$$\mathcal{R} \approx \frac{UL}{\nu}, \tag{3.1}$$

where U is flow velocity, L is the narrow dimension and ν is the kinematic viscosity of the fluid.[16] Given a narrowest dimension of ∼80 μm this sets an upper limit on the flow rate through the channel far in excess of that required. In fact the seal of the PDMS to the coverslip is the limiting factor here, as the pressure required to drive fast - but still non turbulent - flows through the channels was enough to lift the PDMS off the glass. A diagrammatic representation of the combination of two adjacent separate flows into one laminar flow is shown (Figure 3.4(a)). This was verified experimentally by observing the flow of suspensions of small beads through the channels.

In terms of the experiment the upper limit on flow velocity was set by the laser trap. A compromise had to be reached between several factors. A *V. alginolyticus* cell trapped in a stationary solution orients itself along the axis of the laser beam (Figure 2.2(b)), optimising rotation detection. A high flow velocity required not

[13] Soaked for ∼1hr in a saturated solution of KOH in ethanol.

[14] It was also possible to create a very secure association between the PDMS and glass by placing the contact faces in a funny little machine with a bright blue light for a few seconds before joining them. The high cost of such a machine made it impractical however. This was an oxygen plasma device.

[15] See http://scienceworld.wolfram.com/physics/ReynoldsNumber.html or Landau and Lifshitz [99].

[16] Kinematic viscosity $\nu = \eta/\rho$, where η is viscosity and ρ is the specific gravity of the fluid.

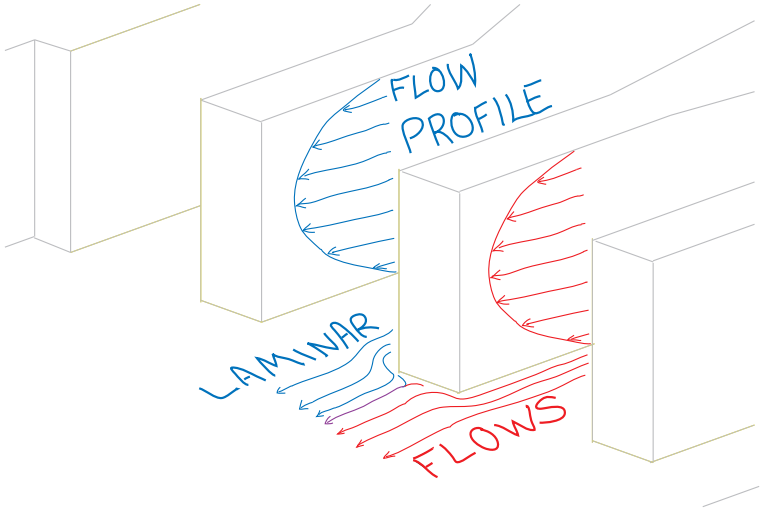

(a) Interface of laminar flows.

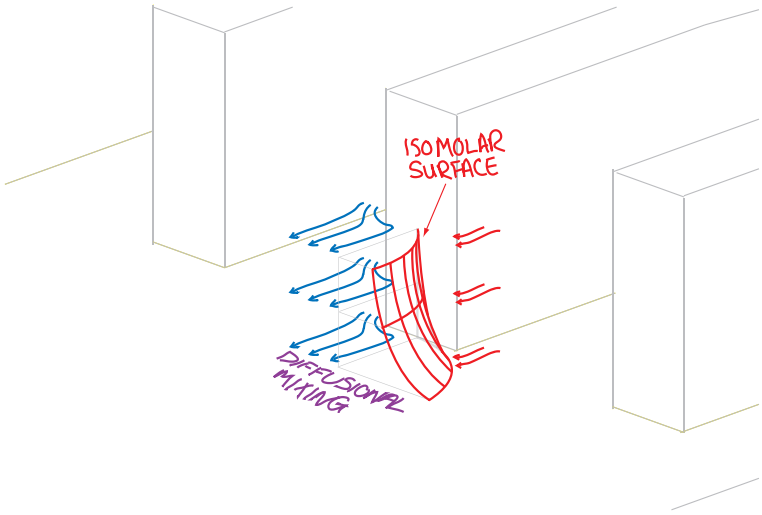

(b) Diffusional mixing across the interface between adjacent flows.

Figure 3.4: (a) Schematic representation of the flow paths of fluids in adjacent channels combining into a single laminar flow and the velocity profiles of the flow with height. (b) Since the diffusive mixing across an interface of different concentrations is a function of time, under steady state flow conditions a surface can be described in terms of the three dimensions of the channel which represents a constant concentration. This surface is shown here as the "isomolar surface."

only a strong laser trap to be used to hold the cell, but also tended to align the cell with the flow direction, losing the rotation signal in the process. The linear decrease in motor rotation rate associated with the use of laser-traps, known as opticution [39], is approximately linear with time and laser intensity. This is dealt with in full in Section 3.2.3 but the advantage of being able to use lower laser intensities is clear.

A laser trap intensity of around 45 mW - which equated to a lateral trap escape force of ∼2 pN for a bacterium - was a reasonable compromise and the flow rate was calculated so that the viscous drag on the cell would not exceed 1 pN.

Modelling the cell as an ellipsoid perpendicular to the flow direction [100], with a semimajor axis a of 1.5 μm and a semiminor axis b of 0.5 μm, its drag coefficient f will be

$$f = \frac{8\pi\eta a}{\ln\frac{2a}{b} + \frac{1}{2}}, \tag{3.2}$$

where η is the viscosity of the fluid (1 cP or 10^{-2} g cm^{-1} for water).
The drag force F on the trapped cell in the flow will be simply

$$F = fv, \tag{3.3}$$

where v is the flow rate. Given the force limit of 1 pN this implies a flow rate in the region of 60 μm/s.

However, as shown in Figure 3.4(a), the velocity profile of the flow is dependent upon the height h of the channel and the vertical position in the channel. The working distance of the objective lens used in the trap limits effective trapping to the bottom 20 μm of the chamber. Therefore the flow velocity 20 μm up into the stream should not exceed 60 μm/s.

Let the dimensions of the flow chamber be defined as follows: the flow direction shall be the y axis with $y = 0$ being the ends of the separate channels, the vertical laser trap axis the z starting at the bottom surface and the axis crossing the faces of all the channels the x, (Figure 3.3(b)). The flow velocity is given as

$$v_y(z) = \frac{4v_{max}}{h^2}(hz - z^2), \tag{3.4}$$

where, in this case, restricting $v_{y=20\mu\text{m}} \leq 60$ μm s^{-1} leads to a v_{max} of 80 μm s^{-1} for $h = 80$ μm. We can now model the mixing of the flows to illustrate that the cell is moved across a sharp transition in sodium concentration.

Consider a sharp interface at $x = 0$ between two solutions of concentration C_{high}

and C_{low} at time $t = 0$. Ions with a diffusion constant[17] D at the interface will diffuse with time so that the concentration C is given by

$$C(x,t) = C_{low} + \frac{C_{high} - C_{low}}{2}\left[1 + \mathrm{erf}\left(\frac{x}{\sqrt{4Dt}}\right)\right], \tag{3.5}$$

where $\mathrm{erf}(x)$ is the error function. Since the flow moves the interface in the y direction from $t = 0$ at a constant speed v_y, t can be replaced in Equation 3.5 with y/v_y. Using equations 3.4 and 3.5 the concentration at any point in the flow cell for a particular interface can be determined. Rearrangement allows a surface of a defined concentration to be plotted in x, y, z space as illustrated in Figure 3.4(b).

In experimental terms this confirms that the transition from one sodium concentration to the next takes place in $\ll$25 μm of the 125 μm transit from the centre of one channel to the next, which is completed in $\sim$1 s. This can thus be approximated as a step function in external sodium being applied to the cell.

Parallel Viscous Flows

Viscosity was varied by the addition of Ficoll 400 (Sigma Aldrich) in a range of concentrations to the existing motility media (Figure 3.5). Preparation of flow cells with channels containing a range of viscosities revealed other characteristics. Under a phase-contrast microscope the junction between adjacent flow streams were clearly visible, implying that the the flows were forming a non-mixing boundary between the separate channels of different viscosity.

This became further apparent when attempting to balance the flow rates to make the streams equal in width inside the flow chamber. Since the higher viscosity fluids required greater heads of pressure to drive them and occupied a wider portion of the stream for the same flow rate than lower viscosities, it was necessary to reduce the flow rate of the higher viscosities to produce streams of similar width. Doing this meant that there was a considerable shear flow between adjacent streams moving at different speeds, which often had the effect of pulling a specimen out of the laser trap, particularly in the higher viscosity solutions.[18] Despite this I succeeded in

[17] D is 1.5×10^{-5} cm^2 s^{-1} for sodium ions.

[18] This is because the refractive index is also affected by the Ficoll concentration. Given that the refractive index of biological samples is roughly 1.05 times that of water and that trapping was virtually impossible above 17% Ficoll, assuming an exponential relation between Ficoll concentration and the refractive index of the solution would give an exponential constant of $\sim$0.001. See the caption to Figure 3.5(b). This value should also be included in the sum of exponential constants which adds to zero, but is in fact negligible compared to the error margins on the line fits to Figures 3.5(a) and 3.5(b).

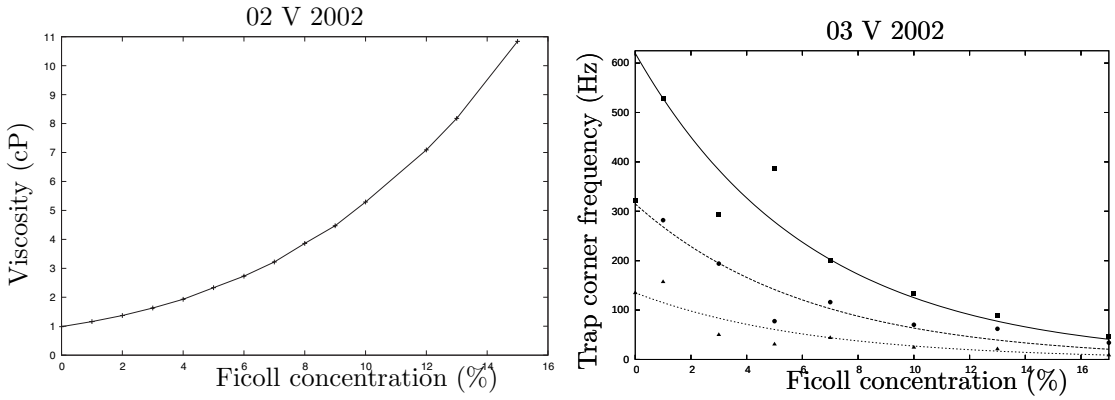

(a) Concentration dependent viscosity of Ficoll solution.

(b) Ficoll concentration vs laser trap stiffness.

Figure 3.5: (a) The viscosity η_F of Ficoll solution dependent upon its concentration (C_F) at room temperature [57]. The exponential line fit to this data is $\eta_F = \exp^{0.162 C_F}$. (b) It was not possible to determine the viscosity by a simple comparison of the corner frequencies of a bead held in the laser trap (See Section 1.3.4) because the presence of the Ficoll changed both the viscosity and the refractive index of the solution. Hence quoted values were used. The corner frequencies at three different laser powers are shown falling off with Ficoll concentration. Simple decaying exponential line fits to all three with a common exponential constant of -0.160 show good agreement. Since trap stiffness $\kappa = 2\pi\gamma f_0$, where γ is the drag coefficient (dependent upon viscosity) and f_0 is the corner frequency, the exponential constants for (a) and (b) should and do sum to nearly zero.

putting several cells through a range of viscosities in 300 mM Na^+.

Laser Local Heating

The other side-effect to be considered in any trapping experiment, besides opticution, is local heating due to absorption of the trapping radiation. The absorbency of PDMS was determined experimentally, showing that the 1 mm layer of PDMS above the flow chamber would absorb ∼2% of the incident 1064 nm light. By analogy to an electrostatic point charge model (for an electrostatic potential V, $\nabla^2 V = \rho/\epsilon$), local heating of the medium due to a point source of temperature T generated by thermal absorption at the focal point satisfies $\nabla^2 T = \rho/\kappa$, where κ is the thermal conductivity of the medium.[19] This implies that at a point, a distance r from the heat source T, the temperature rise $T_r = T/4\pi\kappa r$.

At the maximum experimental laser powers of ∼50 mW this implies a temperature rise of ∼2°C at a depth of 60 μm below the PDMS surface. This is an acceptable level of local heating, since it does not significantly deviate the temperature of the trapped biological system from room temperature, although higher laser powers

[19] 0.6 W m^{-1} K^{-1} for water.

could cause local temperatures to rise to levels which would significantly affect the kinetics of biochemical processes occurring in the trapped body.

Position Detection

The final requirement of the experimental design was to keep a record of the position of the trap in the flow cell in order to correlate the rotation speed with the channel contents. The horizontal range of the piezo stage (Figure 3.2(a)) was insufficient to move across more than once channel. The stepper motors covered the distance, but the vibration inherent in their operation smothered all of the signal from the cell during their operation and occasionally knocked the cell out of the trap.

After many attempts to automate the system I observed that moving the flow cell by hand was the smoothest and most reliable method available. There was also a record of the cell position implicit in the data, since the cell body was significantly deflected from the centre of the trap during transitions. Thus by plotting position in the trap against time it was possible to see when the cell was being moved. Inevitably there were some caveats, since the the PDMS pillars and side walls would deflect the positional signal when in close proximity. Despite this the signature is sufficiently reliable to set the time of transitions to within 0.2 seconds (Figure 3.7(a)).

3.2.3 Opticution and Compensation

As mentioned in Section 3.2.2, the $\sim 3 \times 10^{17}$ photons passing through the trapped cell every second have a detrimental effect on the cell's energetics. The photodamage mechanism is not understood, but is consistent with the illumination causing a steady breakdown of the membrane potential with both time and intensity, resulting in a concurrent slowing of the motor. Experiments were conducted to quantify this and showed that as a good rule of thumb the rotation rate of a trapped cell decreased by an amount in the region of $\sim$0.01% per second per mW of trap power.

The decline of rotation rate for a cell held in a 45 mW trap is shown, (Figure 3.6(a)). For the first 120 s the decline is a steady 0.3% s^{-1}. The discontinuity which occurs at 120 s is most likely to be the disengagement of stators from the rotor, causing a sudden drop in torque. This discontinuous behaviour exhibited during the later stages of opticution is not significant, as all experiments were carried out during the first 25% or less of the opticution process.

It is worth stating, however, that steps up and down in speed occur regularly throughout the rotation of these motors, the magnitude of which suggests that

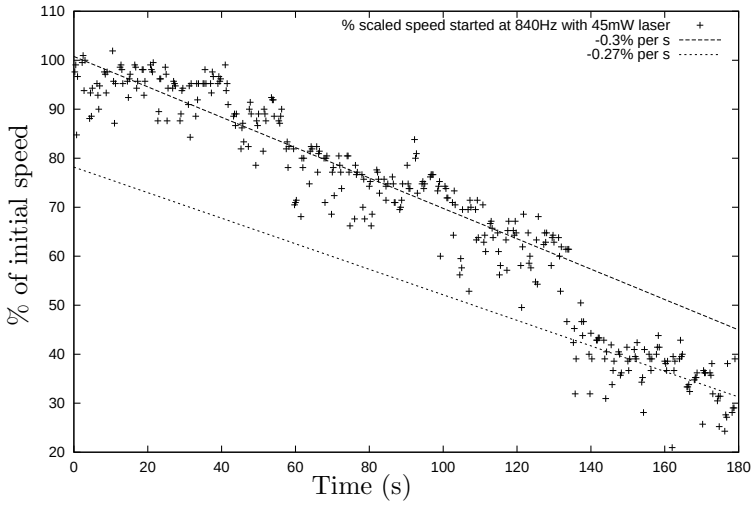

(a) Rotation rate change for an opticuting of a cell.

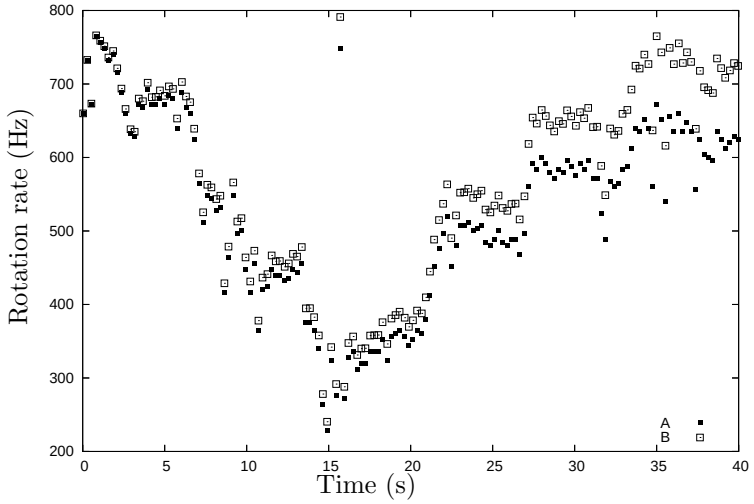

(b) Rotation rate compensated for opticution.

Figure 3.6: (a) Opticution of the cell shown by the steady decline in motor rotation rate. Averaged over many cells this tended to a loss of ∼0.01% per second per milliwatt of the initial speed. (b) Filled squares show uncorrected speeds for a motor initially in 100 mM Na^+ moved out through 50, 25 and 10 mM then back again. The open squares show the same data with the opticution compensation applied. This is shown in more detail with the levels separated in Figure 3.7(b).

stator units are being exchanged regularly at the motor. For the purposes of the experiment described in this chapter this is irrelevant, since we are only concerned with the average rotation rates of the motors, however more will be made of this behaviour in Sections 4.4.2 and 4.4.4.

Assuming this linear percentage decrease in rotation rate ξ with time t, meant that later speeds ω_t could be rescaled to the original rotation rate ω_0 using

$$\omega_{rescaled} = \frac{\omega_t}{1 - \xi t}. \tag{3.6}$$

This is shown in Figure 3.6(b).

3.3 RESULTS

The results of the rapid sodium exchange and viscosity exchange experiments are shown and sodium-dependent and viscosity-dependent torque-speed curves for the *V. alginolyticus* motor are derived separately. A discussion of the change in rotation rate in response to an instantaneous change of external sodium concentration is included to give further insight into the short timescale energetics of the cell.

3.3.1 DETECTION OF STATIC AND TRANSITION PHASES

Given the precise timings of the transitions between channels shown by the locations of the spikes and troughs[20] (Figure 3.7(a)), the opticution corrected trace could be separated into static and transition phases. These can be seen clearly, (Figure 3.7(b)).

For completeness, the repeatability of the experiment is shown (Figure 3.8). Here the opticution uncorrected data from a cell moved back and forth through four different sodium concentrations three times shows remarkable consistency.

For now we are interested only in the static phases shown by filled squares, (Figure 3.7(b)). The average value for each of these contributes one point for each sodium concentration on the load line for the specific cell. For this reason all cells were prepared and introduced to the flow cell in 50 mM Na^+ and every set of sodium concentrations that a cell was subjected to included a channel with 50 mM Na^+ in order to relate the load line specific to each cell to a common torque-speed curve. 50mM was chosen because the swimming speed of *V. alginolyticus* varies most significantly between 0 and 50mM sodium [101], with the speed at 50 mM being at least 75% of the maximium speed it approaches asymptotically at ∼300 mM.

3.3.2 SODIUM DEPENDENT TORQUE-SPEED RELATION

The original plan was to perform the viscosity changing experiment at all sodium concentrations and to combine the two sets of data to form a collection of torque-speed curves for a range of sodium concentrations. However the publication of a reliable experimental torque-speed relation by Sowa *et al.* [65] during the optimisa-

[20] In the time interval between 12 and 20 seconds on the figure the stationary phase does not return to near zero on account of the proximity of the far wall of the flow cell, which deflected the trapping beam on the detector. Despite this it is still easy to tell when the cell was moved into and out of this channel.

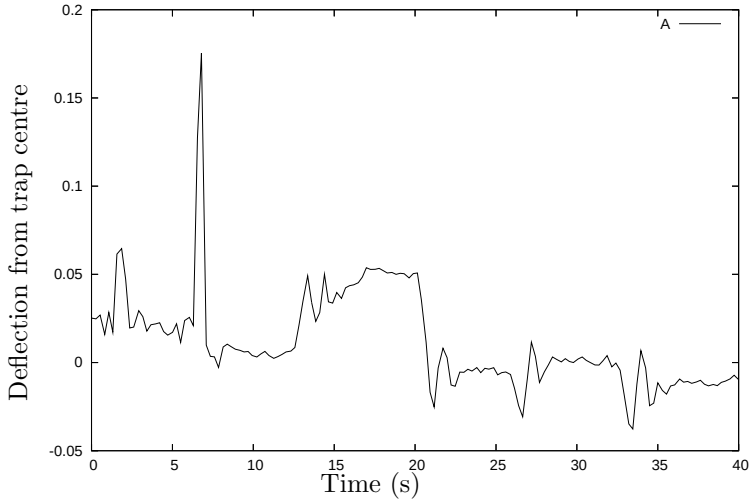

(a) Movement of cell.

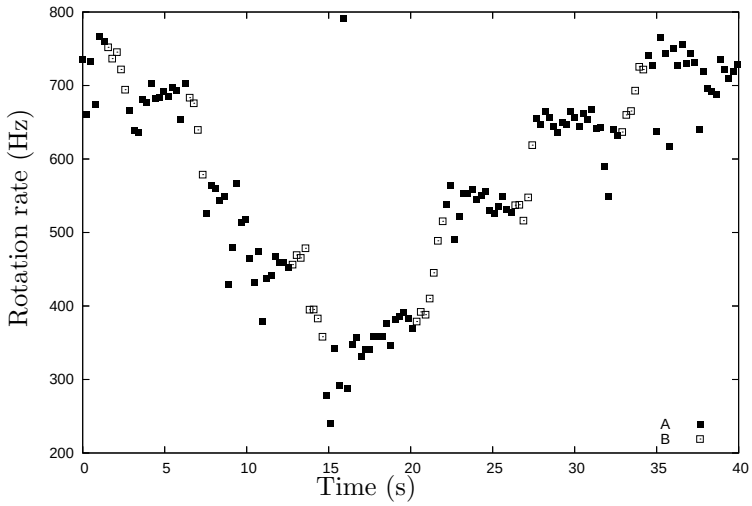

(b) Stationary and moving phases.

Figure 3.7: (a) Deflection from the trap centre indicates that the cell is being dragged through fluid with the trap. Thus spikes and troughs in the figure coincide with movement out and back across the flow cell. (b) Corrected data from Figure 3.6(b) separated into static and transition phases. Filled squares show the motor rotation rate in constant $[Na^+]$ while open squares show the rotation rate during transitions between channels of different sodium concentration.

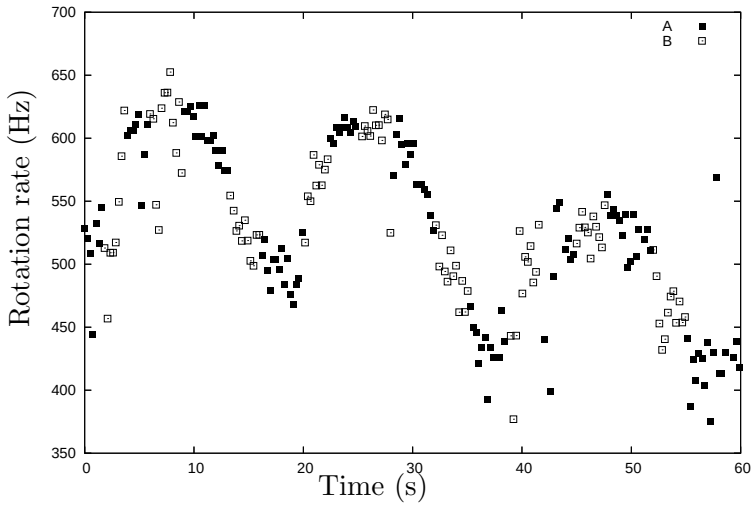

Figure 3.8: Repeatability of this experiment shown with a cell moved back and forth three times through 50 mM Na^+, 100, 200 and 300 mM. The point styles alternate to show where the cell is moved into an adjacent channel containing a different sodium concentration.

tion of my own protocols made some of my planned experiments redundant, though my existing data being in good agreement with their published result, lends credibility to this technique. Given that there was now a published torque-speed curve at 50 mM sodium it was simplest to correlate all of my data using this.

The speed measured in 50 mM Na^+ for each cell was placed on the published 50 mM torque-speed curve thereby associating a torque with the speed of rotation and defining a load line for the particular cell, (Figure 3.9). Having defined the load line for a specific cell, the speeds measured for the remaining sodium conditions through which the cell was passed were placed on the load line, (Figure 3.10). The resulting points for each sodium concentration were fitted to straight lines in two parts, below and above a knee point speed for each sodium concentration, which was determined by the point of best fit for both lines.

The proximity of the 100 mM and 200 mM data to the 50 mM curve must be mentioned here. Naïvely one would assume that as with the swimming speed which does not increase significantly with sodium concentration above 50 mM [35], the torque speed curves should converge. This would imply that the high sodium zero torque speed would be in the region of 1000 Hz. However on many occasions cells prepared in 300 mM sodium showed rotation rates for motors with sheared flagella in the range from 1000 Hz to 1300 Hz.

This disparity can only be explained on the basis of cell energetics. Cells that were used in the flow cell were stored in 50 mM sodium for a long period before

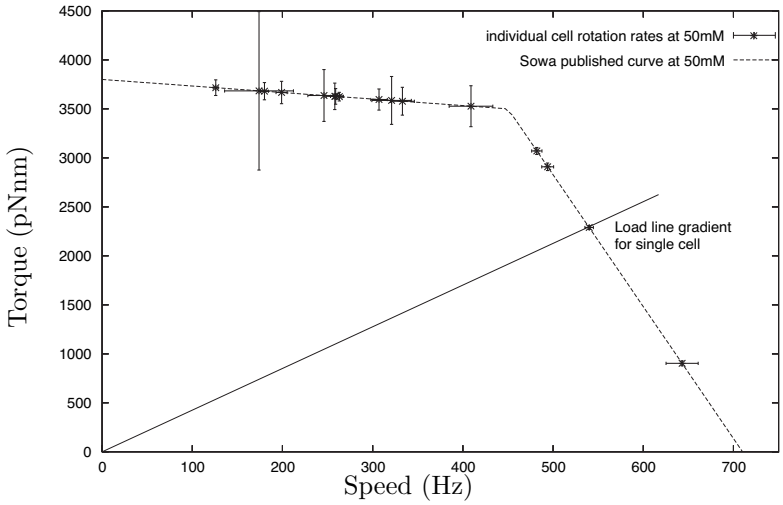

Figure 3.9: The speed measured in 50 mM Na^+ for each cell was placed on the published 50 mM torque-speed curve [65]. This allowed the load line gradient for each cell to be calculated.

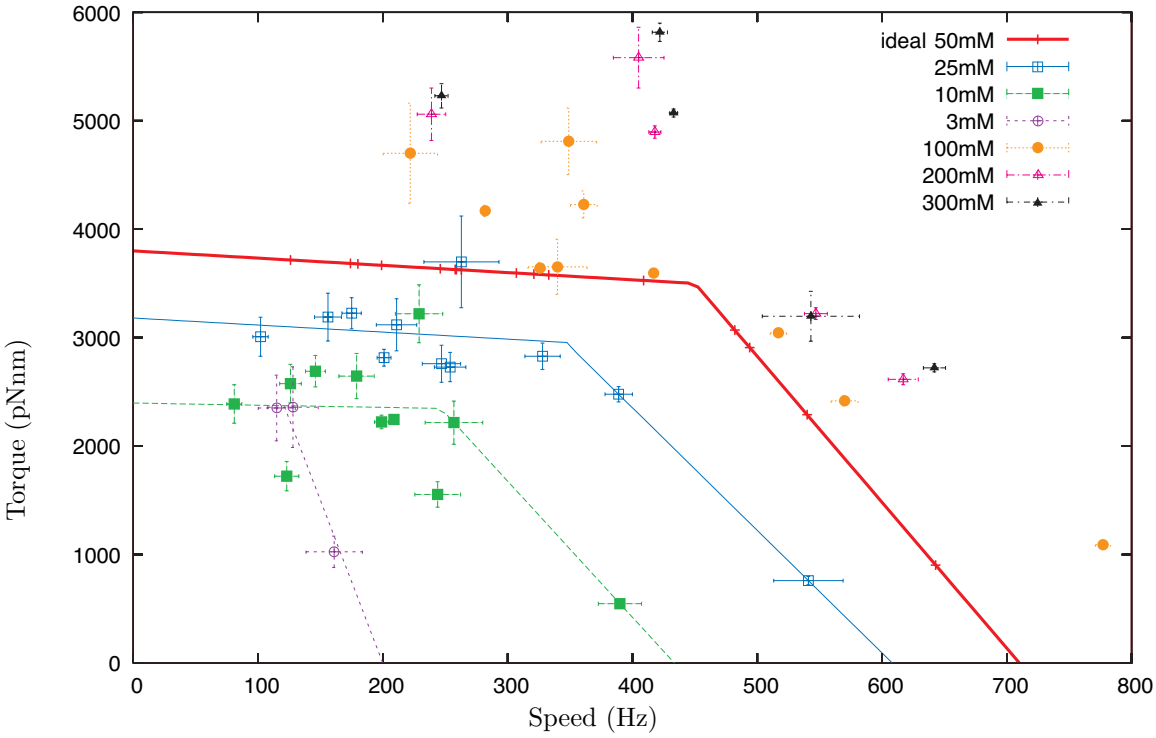

Figure 3.10: Data from cells prepared in 50 mM sodium only. Placing the speeds for cells - in each sodium concentration to which they were subjected - onto their load lines (determined in Figure 3.9) gave the torque speed curves for 25 mM and 10 mM in full, and for 3 mM in part. The lack of torque-speed curves at higher sodium concentrations is discussed in the main text.

transitions occurred. The cells that recorded very high rotation rates were stored in 300 mM sodium for a long period.

The implication of this is that there are at least two time scales of energetic adaptation to the external environment, a short term response on the order of seconds as shown in transitions between sodium concentrations (Figure 3.7(b)) and a long term adaptation of unknown timescale which is revealed in sodium concentrations higher than that used for cell preparation, that determine the maximum rate of rotation in a high sodium concentration. The absolute rotation rate torque-speed curve in 300 mM sodium is shown in Section 3.3.3 while the short term transitions are discussed in 3.3.4.

3.3.3 Viscosity Dependent Torque-Speed Relation

Cells prepared in 300 mM Na^+ and moved through a range of viscosities from 1 cP to 13.7 cP show a different torque speed curve to that shown in Figure 3.10.

It is possible to assume that the torque in the highest viscosity is equivalent to the stall torque. Fixing this torque value at 5000 pN nm for all of the motors defined the gradient of the high viscosity load line with a minimal error margin. Since the gradient of the load line for each cell is linearly related to the viscosity of the surrounding medium for the same motor, the motor torques in each viscosity could be calculated from the speed and the gradient of their respective steepest load lines.

The resulting curve (Figure 3.11(a)), though scattered in the high load regime where clusters of points indicate that the stall torque could be 4000 pNnm, 6000 pN nm, or somewhere in between,[21] has an average stall torque of 5000 pN nm. The knee point appears at ∼650 Hz and the line of best fit to the points with speeds greater than the knee speed intersects with the zero torque axis at ∼1600 Hz.

Given that, as discussed (Section 3.2.1), for a rotation signal to be generated there must be a minimum of one quarter of a turn of flagellum left on a sheared cell (roughly a twelfth of its original length) and likely more; this torque speed curve is consistent with rotation rates up to 1300 Hz which were measured for sheared cells. The difference between the higher speed 300 mM points from cells prepared in 300 mM solution and cells moved from a 50 mM background into 300 mM sodium

[21] This is greater than or equal to the torque of the proton driven motor of *E. coli*. It should be noted that the points which fall in the 6000 pN nm region are not the assumed maximal torque values at high viscosity. The chosen value was 5000 pN because it fitted best to the torque values derived from both the viscosity experiment and the high load points from the preceding sodium variation experiment.

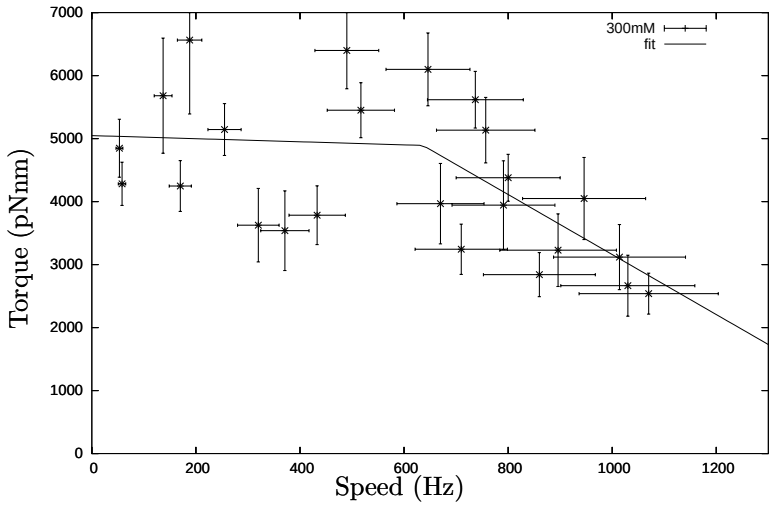

(a) Data for cells prepared in 300 mM sodium fitted to load line gradients for each viscosity to give a torque-speed curve.

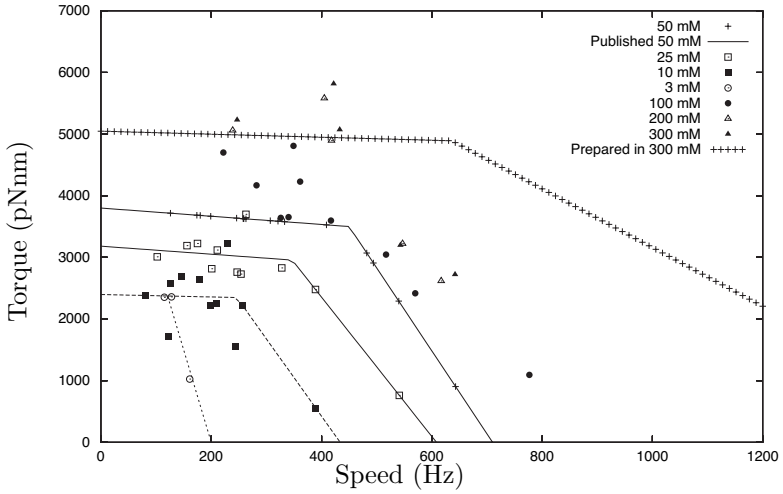

(b) 300 mM torque-speed curve overlaid on curves for cells prepared in 50 mM sodium.

Figure 3.11: (a) Combining the rotation rates of cells moved into a range of viscosities at constant 300 mM Na^+ gave a general form for the torque speed curve at 300 mM. (b) All the derived torque-speed curves shown together for comparison.

is clearly illustrated by the gap between the filled triangles and the 300 mM torque-speed curve at speeds greater than 500 Hz in Figure 3.11(b).

3.3.4 TRANSIENT RESPONSE

Without knowing what the intracellular sodium is for a given external sodium concentration, understanding the energetics of the cell is very difficult. For the sake of exploring this area I have plotted a characteristic speed response of the motor to upward and downward changes in external sodium concentration in Figure 3.12.

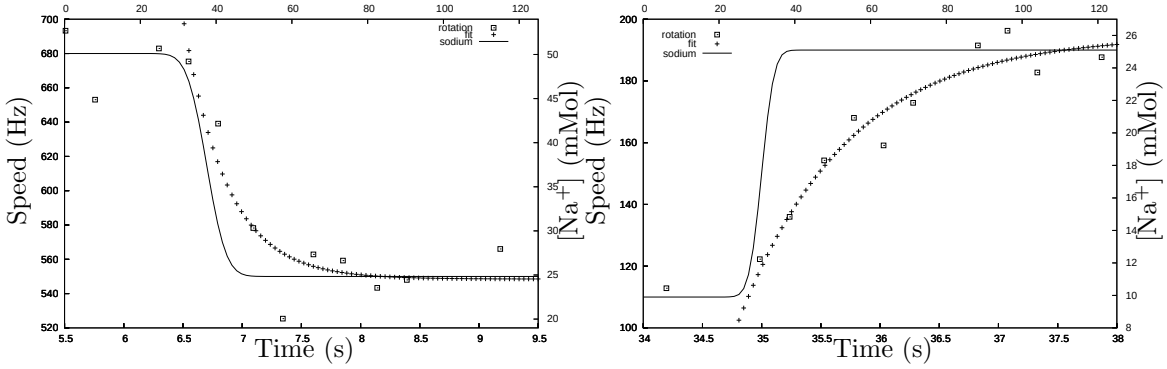

(a) Drop in speed in response to a downward step of external sodium from 50 mM to 25 mM.

(b) Rise in speed in response to an upward step of external sodium from 10 mM to 25 mM.

Figure 3.12: Response of motor rotation rate to external change in sodium. A simple exponential decay time constant of -1.89 s^{-1} with a σ of 0.58 s^{-1} fitted 12 transitions of two different cells moved up and down between 3, 10, 25, 50 and 100 mM external sodium concentration.

Superimposed on the speed trace I have shown a worst-case temporal change in the sodium concentration. In all likelihood the change would have been much closer to a step function. This is to illustrate that even in terms of the slowest possible external sodium exchange the response of the motor rotation is not instantaneous. In fact to generalise for transitions in the range 3 mM to 100 mM,[22] a simple exponential decay time constant of -1.89 s^{-1} with a σ of 0.58 s^{-1} fits 12 transitions of two different cells up and down between 3, 10, 25, 50 and 100 mM external sodium concentration.

3.4 CONCLUSIONS

Alongside the torque speed curves which, by correlating well with the results of Sowa [65], validate both experiments and speak for themselves as results, the laminar flow

[22] With never more than a trebling (or the inverse for downward steps) in external sodium concentration.

cell technique has been shown to be a useful and potentially widely applicable assay.

Further conclusions from this chapter are inferences regarding the energetics of *V. alginolyticus*. With respect to simply measuring the characteristics of motor rotation the intricacies of cellular energetics are more of a hindrance than a help, since they are insufficiently well understood to allow us control of them. However they remain an inescapable presence and as such, the information which can be gleaned from these experiments regarding the energetics is relevant to a complete picture of the system.

The higher stall torque and rotation speed shown by cells prepared in 300 mM sodium relative to those prepared in 50 mM sodium is a clear indication of systematic energetic differences between cells, depending upon the sodium concentration in which they were stored. The quantification of these in combination with the measurement of smf and pmf in the cell would make a large contribution to the field.

Given a stated $\Delta\Psi$ for *V. alginolyticus* of -150 mV [67] and making an assumption that[23] rotation rate will be proportional to smf in the high load regime below the knee, I chose to relate the speeds of several cells at high loads to the smf in each concentration, leaving the internal sodium concentration as the free parameter. To a first approximation the conclusion was that internal sodium is maintained at a constant level by the cell, independent of external sodium.

Knowing that there is a significant primary sodium component to the energetics of *V. alginolyticus* which is capable, where necessary, of extruding sodium ions directly by the respiratory chain [66], it is not beyond the bounds of possibility that - as with *E. coli* whose internal pH is closely regulated and buffered across a wide range of external pH - the cytoplasmic sodium concentration is constant, independent of external $[Na^+]$ in a wide range of external sodium concentrations. Thus the time constant of the equilibration may indicate the exchange time between the surrounding medium and the periplasmic milieu of the cell.

[23] As in the case of the proton driven motor of *E. coli* whose motor rotation rate follows the pmf [102].

Chapter 4

Characterising a Chimæric Motor

The YS34 chimæric motor strain (Appendix C.2) was brought to Oxford from Nagoya, Japan in 2003. The rotation detection techniques in my lab were better than those available in Japan and so began a long collaborative effort with Yoshiyuki Sowa.[1] Our first goal was to discover a set of conditions under which we could maintain constant slow motor rotation rates to search for fine structure in the rotation.

The Chimæra motor has all the technical advantages of the *E. coli* background (Section 3) for detection purposes, while the sodium dependence allows the motor driving force to be changed across a large range without affecting the internal biochemistry of the cell. Cells are sensitive to large fluctuations in external pH, therefore large changes in powering ion concentration for the proton driven motor cannot be realised without adversely affecting the cell physiology.

In the process of discovering these slow rotation conditions the motor was characterised in several ways. Some of the results are clearly explicable, while others, including the torque-speed relation - which was investigated in part with another member of my lab Chien-Jung Lo - require an expanded range of techniques to be applied before a conclusive statement can be made.

[1] Yoshi and I worked together on the early characterisation work, including Resurrection and Deresurrection, Speed vs Sodium relation and all of the laser trap based experiments for Chapter 5.

4.1 Experimental Aims

Having determined that the presence of two plasmids inside the cell had a considerable effect on the generation time[2] (Appendix C.2.1) it was necessary to find a growth condition after which cells could be reliably resurrected from a low initial expression level. It was hoped that this would then allow the production of steadily rotating motors with single stators. The rotation-rate dependence of a single stator on external sodium concentration could then be found.

With no directly relevant background literature available concerning the sodium energetics of the *E. coli* cell (Section 1.4.3), particularly one loaded with an additional large sodium flux, we were forced to treat the internal sodium concentration as an unknown parameter. The determination of internal sodium concentration, its dependence on external sodium levels and the simultaneous measurement of the membrane potential is a large project in itself and has been commenced separately and successfully so far by Chien-Jung Lo [103]. This work will fully clarify the results of this experiment in the future, but in the meantime we can be only partly informed by the knowledge that *E. coli* has at least one primary sodium energetic pathway [104] and perhaps two (Terry Krulwich, personal communication[3]). It is known that the expression level of the Na^+/H^+ antiporters in the cell is dependent upon the sodium conditions during growth, however the impact of the inward flux of ∼1200 ions per revolution for a fully resurrected motor on the energetics of the cell can only be hypothesised for now.

Beyond the determination of slow speed rotation conditions, the method of Ryu [33] was employed to investigate the torque-speed relation for this motor and its dependence upon external sodium concentration and the number of stators present.

4.2 Apparatus

All of the experiments were performed on the laser trap and microscope described previously, (Section 2.1). Cells were cultured and prepared throughout in 85mM sodium to maintain consistency of their energetics and the ionic strength of all media was maintained with potassium where lower sodium concentrations were required. Freshly cultured cells were sheared 40 times, washed (Appendix C.2.1) and immobi-

[2]Wild type cells tended to take around 3 hours to reach a density of 10^8 cells/ml while these cells took in the region of 5 hours to reach the same population density.

[3]Complex I has been shown to be a sodium pumping NADH:ubiquinone oxidoreductase [105] and ChaA can pump sodium in certain conditions.

lized by 15 minute incubation onto polylysine coated hydrophilic glass. Latex beads in a solution of motility medium were introduced at a concentration upwards of 10^9 beads/ml and incubated for a further 5 minutes to allow them to associate to the flagellar stubs. In this way a sparse lawn of cells with labelled flagellar stubs was produced.

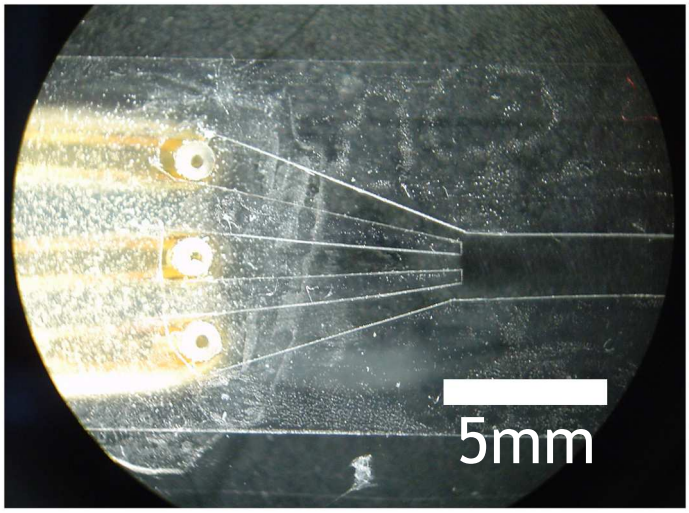

Figure 4.1: A 100μm deep flow cell with three inputs allowed rapid exchange of the medium around the cells stuck to the surface of the glass in the main channel.

For resurrection experiments a standard tape tunnel slide was used, however for the purposes of rapid exchange of fluid a simple multi channel flow cell was prepared in between a glass slide with input pipes glued in place and the coverslip, by cutting a channel pattern into double sided sticky tape (Figure 4.1).

4.3 Rotation Analysis

Position signals for the rotating bead were acquired at 2 kHz by the BFP method and rotation rates were calculated by the method described previously (Section 1.3.4). A running window 1 second wide was passed at 0.1 second intervals across the data to provide rotation rate vs time data for further analysis.

During the resurrection process discrete changes in speed can be seen by eye. In order to automate the process of step detection and to accomodate for the noise in the data (Section 4.4.1) various techniques were applied. These are discussed below.

4.3.1 Discrete Speed Level Detection

The simplest approach to smoothing noisy data, while preserving edges in the signal, was to median filter the signal with a reasonable (usually 1 second) window width. Clear levels could be extracted from the filtered signal by eye or by a histogram method. Preservation of edges in the signal by this method is poorer when the levels are close together and the fluctuations of the signal overlap significantly.

To this end a filter and edge detector based on the algorithm of Chung and Kennedy [106] was applied. In summary, two adjacent windows of equal size were run through the data and the variance of each was calculated. The filtered value for the point at the junction between the two windows was defined by the mean value of the window with the smallest variance.[4] Simultaneously a Student's paired t-test was performed to determine the statistical significance of the separation between two distributions. Absolute values of the t-statistic which fell above a chosen threshold defined a step at that point. By this means a step could be assigned a confidence level greater than that defined for the threshold value, given the number of degrees of freedom for the system.[5]

In practice, because of the large separation between resurrection levels and the magnitude of the signal noise, the sensitivity of the step detector, even with a 0.8 s window width, at confidence levels of 99.9% was low enough to accept relatively small amplitude fluctuations as steps. In order to limit this, the threshold was set to a minimum confidence level of 99.997% whereby only steps of larger amplitude were accepted.

4.3.2 Speed per Revolution

In certain cases, in order to investigate the process of stator integration during resurrection more closely, one axis of the rotation signal was smoothed and the period of each oscillation was calculated. This gave considerably greater precision with which rotation rate changes could be measured, particularly at lower speeds.

[4]This is referred to as the uncontaminated variance since the larger variance value may be caused by the presence of a step within the window - hence the contamination. The window width was set such that it was highly unlikely that two steps would occur within a single window. This ensured that the smaller of the two variances never contained a step.

[5]The number of degrees of freedom is one less than the number of data points in each window.

4.4 Results

The sodium dependence of rotation rate and stator number are presented here, with an investigation of the torque-speed relation and a measurement of the rates of stator arrival, separation and exchange from the rotor. A closer analysis of the change in speed between resurrection levels sheds a useful qualitative light on the process of stator integration at the rotor.

4.4.1 Stator Number Determined by Resurrection

A population of cells cultured in 10 mM IPTG had a broad distribution of motor units, such that the range of motor rotation rates extended from zero to near maximum. Selecting a slow spinning motor from among this population and adding 100 mM IPTG to the medium resulted in the arrival of new stator units at the motor roughly 30 minutes later. Each new stator unit contributed extra torque to the motor, resulting in a sudden increase in rotation rate (Figure 4.2). These are termed resurrection levels.

At low stator number and in the high load regime, the speed is linear with stator number, allowing the number of stators present to be inferred, even if the lowest levels are not measured. With smaller loads, the speed increase contributed by the arrival of single stators is linear at low stator numbers but begins to converge at higher stator numbers. This, convolved with the long term fluctuation in motor rotation rate which is accountable to variation in the sodium motive force, means that higher resurrection levels in low load conditions are often difficult to separate.

In spite of this, motors with 0.5 μm beads attached, whose single stator speed was measured to be 35 Hz, were resurrected to levels approaching 400 Hz, with a small reduction in the level interval above 300 Hz. The presence of 10 discrete levels could be counted, however the remaining few were unclear. At a conservative estimate however, there must have been at least 12 stators present to generate such high rotation rates. This corroborates results from Mark Leake and Stuart Reid [107], working with the WSR8 strain, who have shown that there are more than the currently accepted number of 8 stator units [33] present in a fully resurrected motor.

The speed of rotation for a given load and external sodium concentration is roughly comparable to that for the wild type sodium-driven stators in their native *V. alginolyticus* background and higher than the speed of a wild type proton-driven motor.

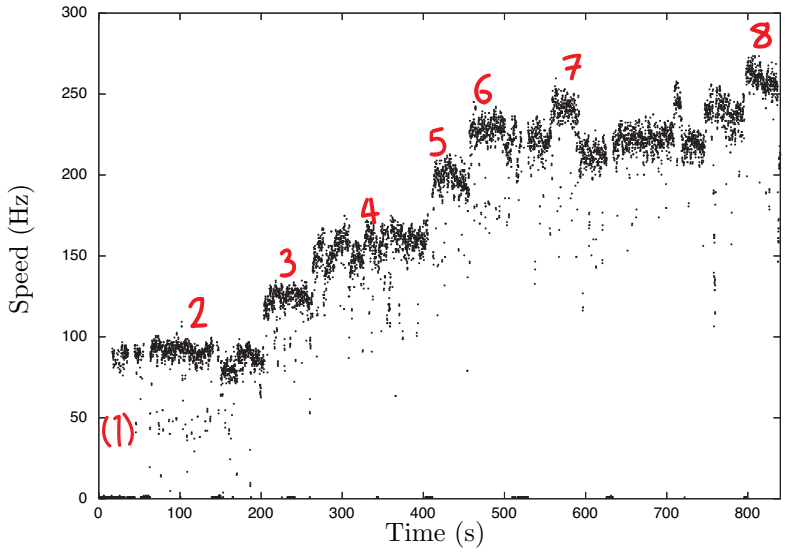

(a) 0.5μm bead resurrection in 85 mM Na^+.

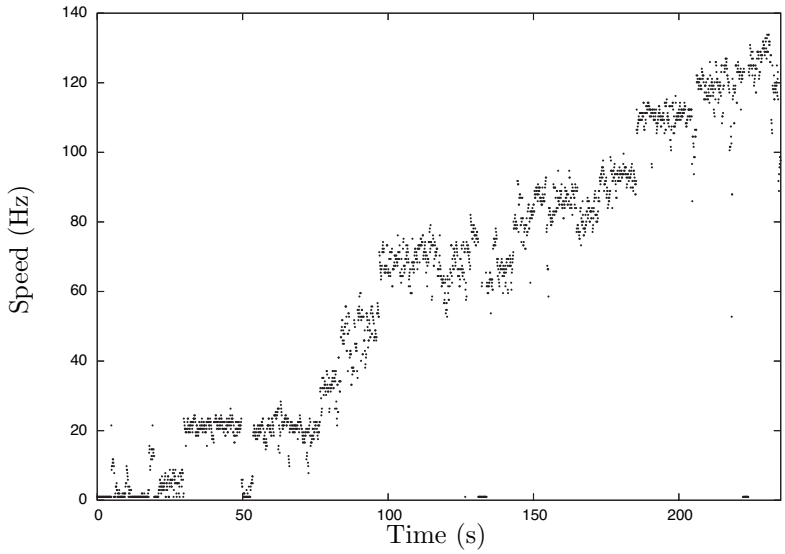

(b) 0.75μm bead resurrection in 85 mM Na^+.

Figure 4.2: Rotation rate versus time traces for chimæric motors induced with 100 mM IPTG for motors with (a) a 0.535 μm bead and (b) a 0.756 μm diameter bead attached to flagellar stub. In (a) the number of stators present is marked on the graph for each level. The first level is shown in brackets because it never appeared steadily. This ghosting is discussed in Section 4.4.4.

4.4.2 Sodium Dependence of Rotation

Single stator rotation rate

By a combination of resurrecting motors in a range of external sodium concentrations and changing the sodium concentration in the medium around partially resurrected motors it was possible to infer the speed contribution per stator at each sodium concentration. From this the dependence of single stator rotation rate upon external sodium was derived (Figure 4.3(a)). The low level sodium concentration required to reduce rotation rate to zero shows considerable fluctuation between cells, presumably on account of the variation of internal sodium concentration between cells becoming most significant at this point.

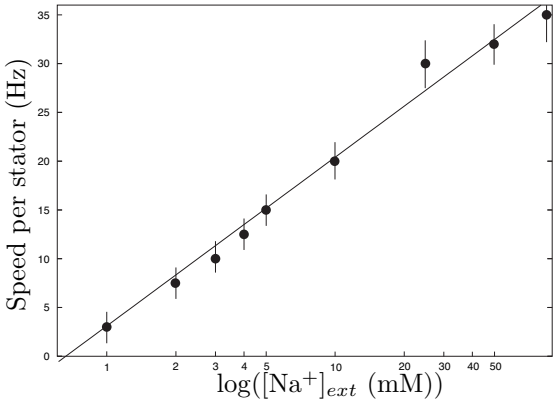

(a) Single stator rotation rate vs External Sodium Concentration.

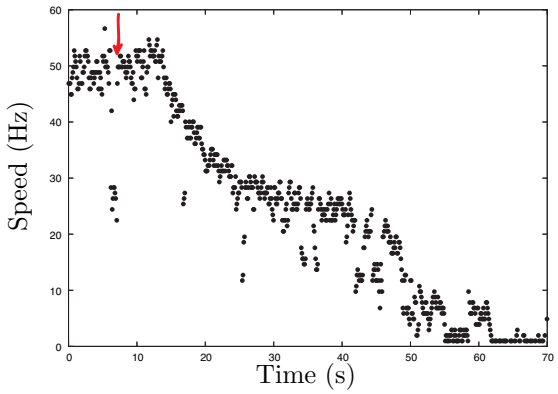

(b) Lithium dependent rotation rate.

Figure 4.3: (a) The average speed interval between low stator integration levels for a 0.5 μm bead at a range of external sodium concentrations was used to extrapolate back to the sodium concentration at which the rotation speed could be expected to be zero. (b) Lithium is able to substitute for sodium with partial effectiveness as a powering ion. In this case the transition from 5 mM Na^+ to 5 mM Li^+ added after 10 seconds (red arrow) clearly displays the reduced torque-generating capacity of the lithium ion, and the subsequent reduction in stability of the stator association with the rotor.

Lithium Dependent Rotation Rate

The lithium dependence of motor rotation was also investigated, since the relative permittivity of the sodium channel, in axon membranes, to lithium is 0.93 [1] and the sodium driven motor of *V. alginolyticus* is known to rotate more slowly [25] with lithium as the powering ion.

The result of the substitution of 5 mM lithium for 5 mM sodium (Figure 4.3(b)) clearly shows a reduced rotation rate as the lithium exchanges for sodium in the

system. However after about 40 seconds it can be seen to have changed speed in discrete steps, as though stators were rapidly engaging and disengaging at the rotor. This, perhaps, is an illustration of the instability trait which is mentioned by Liu *et al.* [25] in relation to the rotation of wild type sodium-driven motors when powered by lithium ions. The cause of this instability is not clearly defined, however, as is shown below, the lithium substitution was not the only condition that affected the stability of the association between stators and the rotor.

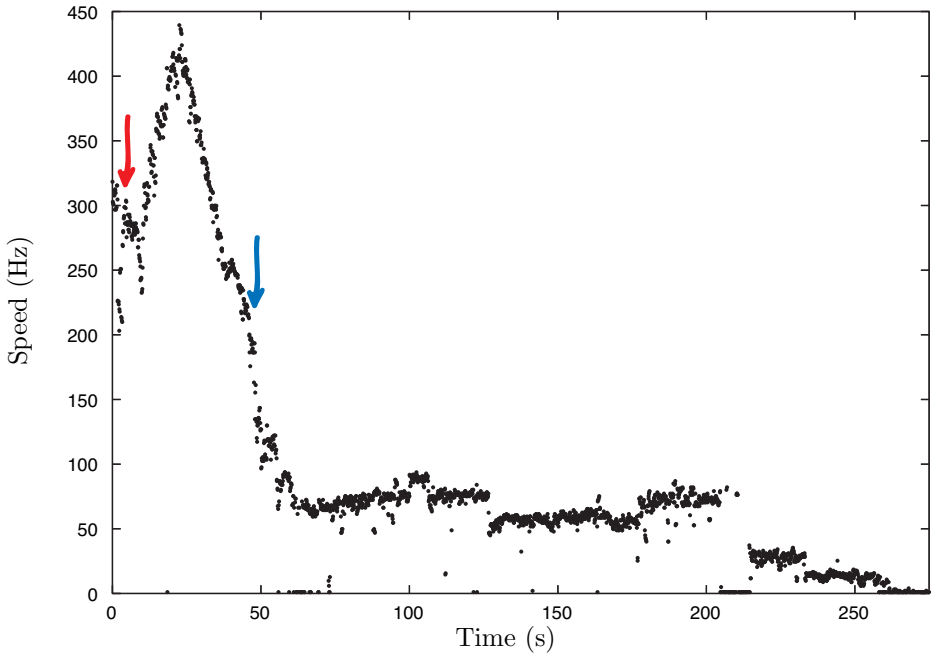

Figure 4.4: Sharp external sodium transitions, in this case from 85 mM to 0.1 mM, (flow started at red arrow and stopped at blue arrow) from a high to low concentration with a change greater than an order of magnitude, caused the motor to slow sharply followed by further stepped slowing, implying a separation of stators from the rotor to a new equilibrium level. The flow process began at time $\sim$ 15 s but the point at which the sodium concentration drops in the medium immediately surrounding the cell is clear. The increase in rotation rate with the flow on is due to a change in the rotational locus due to the drag on the bead from the flow. The result of this is that the eccentricity of the bead rotation drops, reducing the drag coefficient, yielding an increased rotation rate.

This begs the fundamental question as to why the sodium driven motor has higher speeds than the lithium driven motor. In all probability this is due to the relative dehydration energies required to remove all but two of the water molecules from the hydration shells of the ions in order to allow them to pass through their stator ion channel. The smaller atomic radius of the lithium ion (1.67 Å) relative to the sodium ion (1.9 Å) allows stronger interaction between the nucleus and the water molecules, requiring a greater energy to dehydrate the lithium and thus slowing

the conduction process for a given ion-motive force, relative to sodium conduction. This will throttle the upper rate limit of ion conduction, which, it is assumed, relates directly to the maximum rotation rate. Something similar may also be the reason for the proton driven motor being slower still, however the formation and dehydration of hydronium ions during proton conduction makes this more difficult to quantify.

Sodium Induced De-resurrection

Early experimental protocols for the single stator rotation vs sodium experiment required partially expressed motors with a known number of stators to be passed from 85 mM sodium into lower levels, whilst the speed change was recorded. However, it soon became apparent that sharp drops in external sodium caused the probability of a stator dissociating from the rotor to rise. As a rule of thumb, a downward change greater than an order of magnitude could be counted on to cause the motor to stop rotating, hence the necessity of the final approach used. This dissociation of stator units from the rotor was termed "de-resurrection" and has been seen before with proton driven motors under conditions of de-energisation [108], but has not been conclusively shown to be non-catastrophic breakage of the motor.

The de-resurrection was not confined to partially expressed motors. Even a fast-rotating, fully expressed motor could be slowed stepwise to a halt (Figure 4.4) by a large drop in the external sodium concentration.

Sodium Induced Re-resurrection

The proof that the de-resurrection was a temporary removal of the stator units from the rotor, rather than any catastrophic jamming of the motor came with the reintroduction of a high sodium medium. The motor would more often than not begin to rotate again with increasing discrete steps of speed (Figure 4.5) up to its original high speed. The longer a cell was left in a low sodium medium, the longer the recovery process would take.

Without knowledge of the membrane potential or the internal sodium concentration response to external sodium change it is impossible to state the cause of this de-resurrection, so the dependence of the rate of stator association to the rotor upon the smf must remain unknown until these can be measured simultaneously.

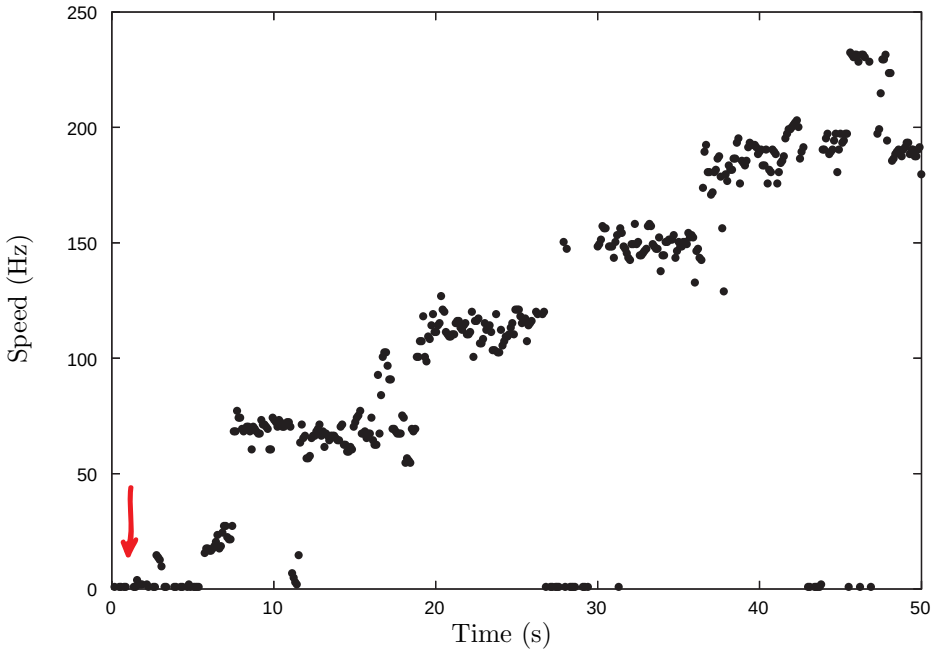

Figure 4.5: Previously fast rotating but de-resurrected cells, when reintroduced to high external sodium concentrations (85 mM sodium flowed at red arrow), would often begin to rotate again in discrete speed steps. In this case the sodium concentration around the cell from Figure 4.4 was raised some 30 seconds or so after it stopped rotating completely, resulting in a very clear resurrection trace.

4.4.3 Torque-Speed Relation

The attempt to replicate the experiments of Ryu [33] in a range of sodium concentrations was inconclusive.

A reluctance to resurrect which increased with the age of the original stock and was put down to degradation of the plasmid but much later turned out to be a failure on the part of the IPTG, complicated matters. The quality of the data taken was consequently less than ideal. Long resurrection records of the quality shown (Figure 4.2(a)) were the exception rather than the rule, forcing a compromise to be reached.

Rotation rate levels for a specific bead size were inferred by the combination of many partial resurrection traces to create generic average levels for each stator number at a given sodium concentration (Figure 4.6). These levels were then combined to show the torque-speed points for each stator number (Figure 4.7).

As can be seen from the resurrection dependent torque-speed curves (Figure 4.7) based on average loads for each bead size, there is no hint of the typical knee in the torque-speed curve. The knee might be expected to occur somewhere within the range of viscous loads and sodium concentrations used if the motor behaves the same

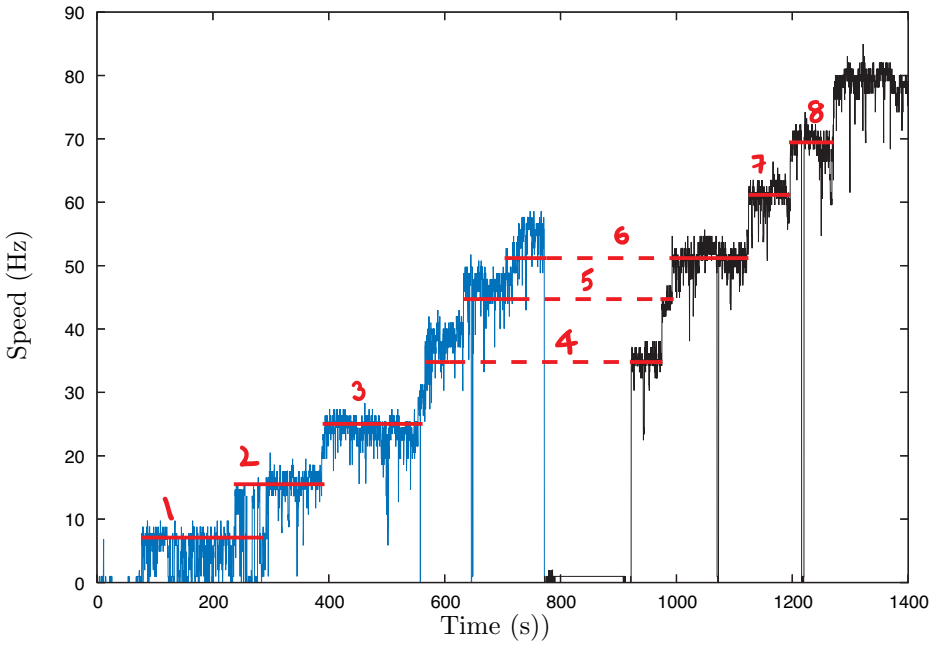

(a) Two resurrection traces for 1 μm beads in 85 mM sodium combined to define resurrection levels.

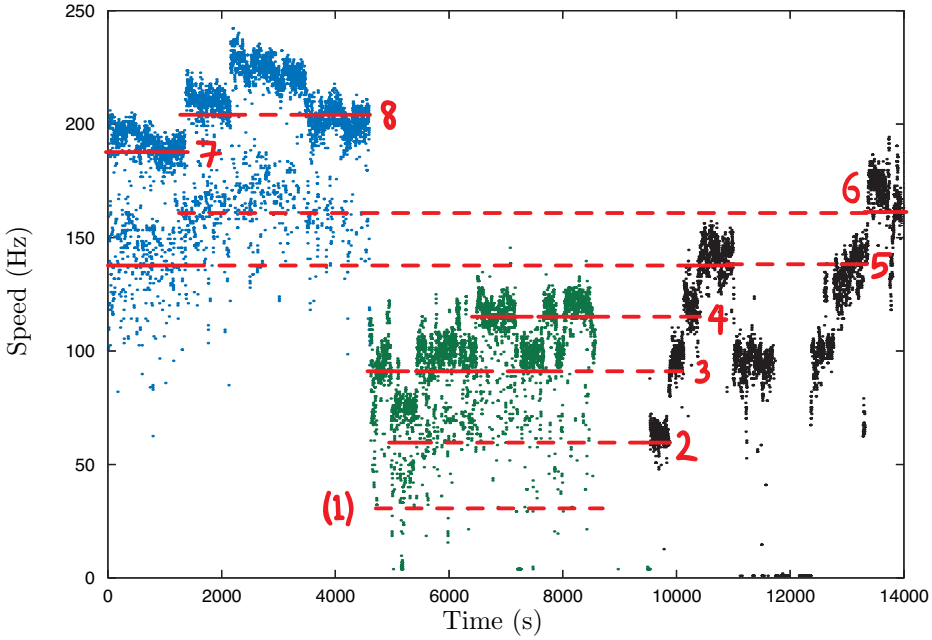

(b) Three resurrection traces for 0.5 μm beads in 85 mM sodium combined to define resurrection levels.

Figure 4.6: Examples of resurrection levels estimated by the combination of several partial resurrection traces. (a) Resurrection levels for motors with 1 μm beads in 85 mM sodium from two separate cells (blue and black traces) were combined to give a complete set of values for rotation rate vs stator number. (b) Poorer quality resurrection traces were combined for 0.5 μm beads in 85 mM sodium to again infer resurrection levels for each sodium stator number.

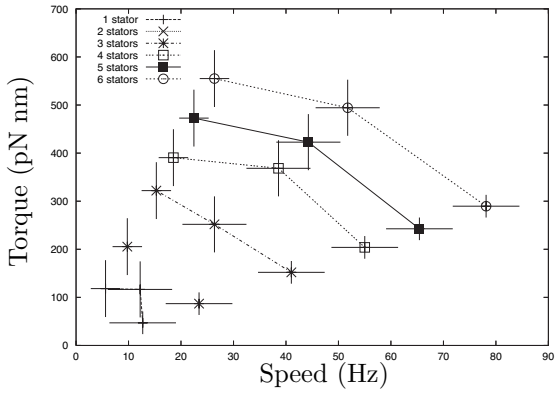

(a) Simple Torque vs Speed at 1 mM sodium.

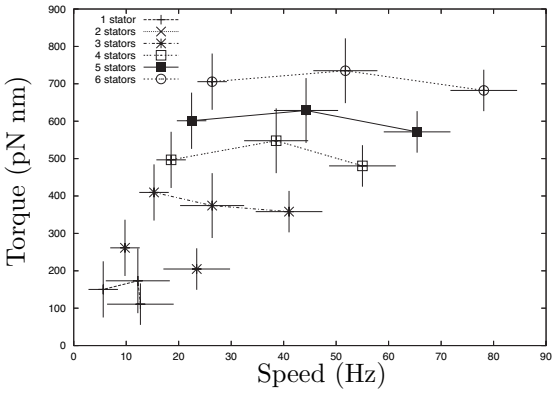

(b) Ryu method corrected Torque vs Speed at 1 mM sodium.

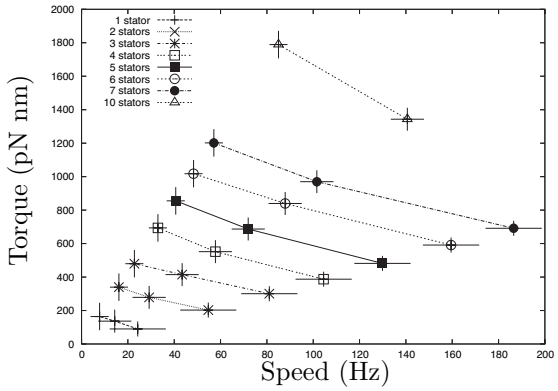

(c) Simple Torque vs Speed at 5 mM sodium.

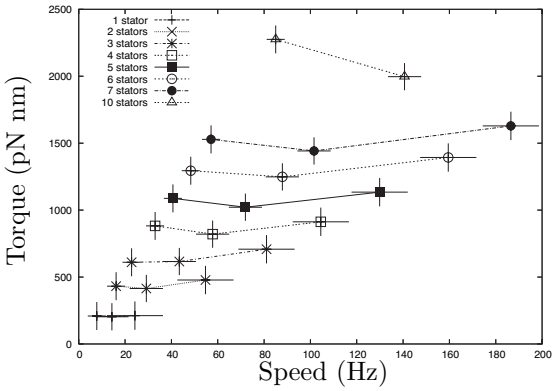

(d) Ryu method corrected Torque vs Speed at 5 mM sodium.

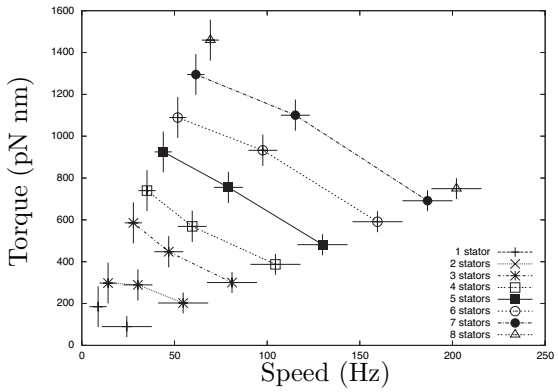

(e) Simple Torque vs Speed at 85 mM sodium.

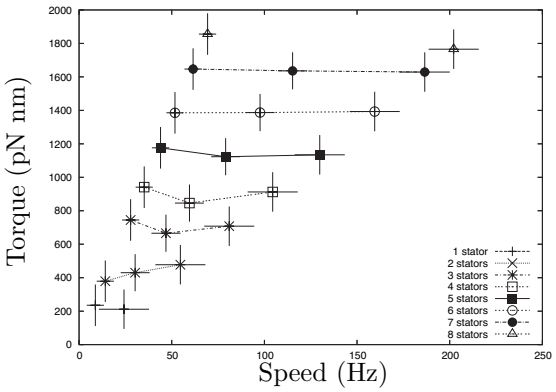

(f) Ryu method corrected Torque vs Speed at 85 mM sodium.

Figure 4.7: Sections of the torque vs speed relations for chimæric flagellar motors at 1 mM, 5 mM and 85 mM sodium are constructed on the basis of the bead being the dominant source of drag in (a) 1 mM external sodium (c) 5 mM sodium and (e) 85 mM sodium. Alternative torque-speed curves are constructed by the method of Ryu [33], with an additional drag component from an average flagellar stub length of 0.9 μm, chosen to place the 85 mM torques in the high torque regime, concurrent with the *V. alginolyticus* torque-speed relation (Figure 3.10). These are shown for comparison in (b) 1 mM external sodium (d) 5 mM sodium and (f) 85 mM sodium. Further discussion about the shape of these curves is found in Section 4.4.3, but it is immediately obvious that they do not clearly follow the characteristic trend of convergence at a single high speed as shown for the proton driven motor. Furthermore there is no clear knee point in the torque as has been shown for wild type sodium driven and proton driven motors. Further work is required to decide whether the difference is sytematic or due to experimental issues.

way in an *E. coli* background cell as it does in its natural *V. alginolyticus* background cell. Instead, the torque appeared to fall off roughly linearly with rotation rate and the zero torque rotation rate did not converge at the same speed independent of stator number, with the possibility of a knee point occurring at very low (<50 Hz) rotation rates if at all. Furthermore the extrapolated stall torque falls some way below that measured for the *V. alginolyticus* motor (Figure 3.10 (a,c,e)) and a long way below the estimates for the proton driven motor. This is clearly either erroneous data, or a significant extra parameter has been missed.

The fitting method of Ryu [33] was therefore applied, which assumed a known torque versus speed relation for the 5th stator level and used the unknown flagellar stub length as the fitting parameter. Beyond the fact that the drag coefficients for a given bead size quoted by Ryu appear somewhat high, there is the added complication of the lack of a known torque-speed relation to fit to. The torque-speed relation for the proton driven motor is not a candidate on account of the observation of rotation speeds in excess of 300 Hz with a 0.5 μm bead in 85 mM sodium. Since the zero torque speed of a proton motor falls below this value, we can safely discard this possibility.

This leaves the possibility of fitting the curve to the *V. alginolyticus* curve derived in Chapter 3. The validity of this in itself is unclear, given that the stators are not interacting with a native rotor and that we know very little about the comparative energetics of the two cells or any adverse load that the presence of a large extra sodium circuit may cause. Assuming a torque speed curve for the chimæra at 85 mM sodium which is roughly the shape of that for *V. alginolyticus* at 50 mM sodium, implies that all of the 85 mM rotations should fall in the constant high torque range before the knee. Fitting flagellar stub values to this shows that a consistent stub length of 0.9 μm adequately corrects the curve, independent of bead size. Using this as a reference, the curves for 5 mM and 1 mM could be reconstructed (Figure 4.7).

At best, the conclusion of these reconstructions is that within the margin of error all of the loads at every sodium concentration fall into the linear pre-knee regime. The downside to this is that the flagellar stub is by far the dominant drag component compared with a 0.5μm bead, which implies that this experimental protocol can never get far beyond the knee point, thus necessitating an alternate experimental approach in order to measure high speed rotation. Alternately it could be a demonstration of the fact that this motor behaves differently from previously measured naturally occurring motors.

Given the potential for pathological conditions having occurred due to the IPTG

degradation, it is perhaps barely worth speculating as to why this motor does not follow the patterns of motors in their native backgrounds without first performing further experimental work. The first experiment to perform would be to replicate the Chen assay [57] using a small bead and a range of viscosities on a fully resurrected motor to determine what the shape of the torque-speed curve truly is at each sodium concentration. However the possibility remains that the energetics - or more specifically the unnaturally high load on the sodium cycle - of the cell directly affects the torque-speed relation in an unstable and perhaps indeterminate manner.

4.4.4 Stator On/Off Rates

The resurrection traces for the sodium motor exhibit what I refer to as ghost levels which can be clearly seen as a sparse collection of points falling ∼35 Hz below the main rotation levels in Figure 4.2(a). Given that each of these points represents the dominant rotational frequency from one second of data, they cannot simply be passed off as noise. The size of the interval between ghost levels and main levels suggests that they correspond to short periods of stator dissociation from the rotor.

Step Detection

A Chung-Kennedy step finding algorithm (Section 4.3.1) with a 5 s window width was applied to 19 of the best resurrection traces and the steps found were recorded (Figure 4.8(a)). The clear resurrection steps were found, but shorter steps relating to the ghost levels were not recorded. Repeating the analysis using an 0.8 s window width found many shorter steps within a resurrection level (Figure 4.8(b)) as well as the resurrection steps.

Analysis of a large data set using only a small window width would be expected to show up both the steps within a resurrection level and the resurrection steps, by a double exponential dependence of the interval length distribution. Given the limited data set available it was necessary to record the resurrection steps independently from the shorter fluctuations using a longer window width in order to build up a meaningful distribution for them. For this reason the interval lengths have been treated separately.

Inevitably the step detection is not perfect. This is due to fluctuation in the variance for reasons which are unclear[6] and the presence of step-like and non step-like transitions between levels (these are discussed in more detail in Section 4.4.5).

[6]See discussion of variance of rotation rate which follows.

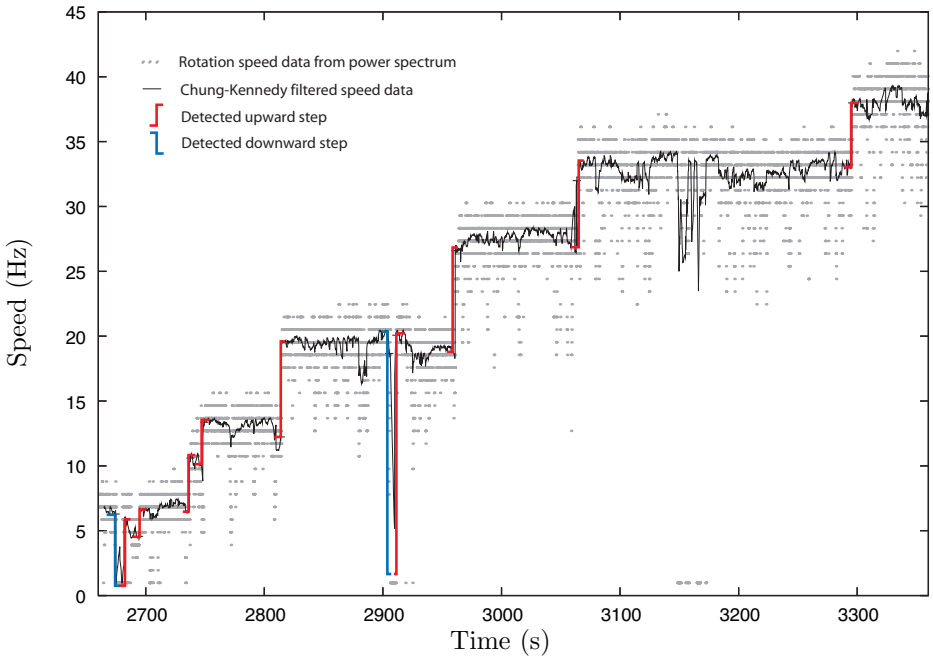

(a) A Chung-Kennedy filter and edge detector with a 5 s window width applied to resurrection data for a 1 μm bead in 2.5 mM Na^+.

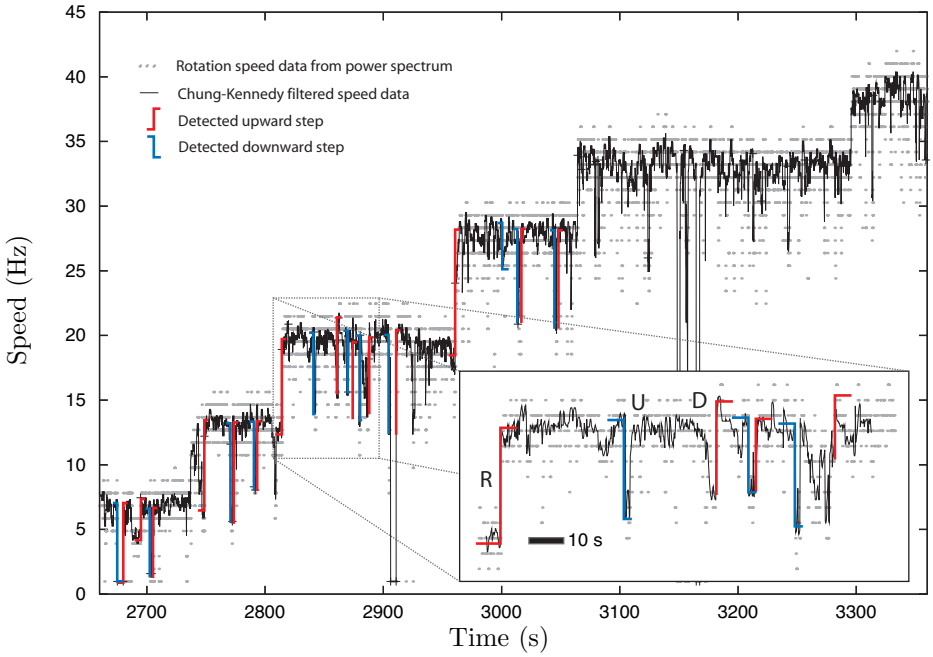

(b) A Chung-Kennedy filter and edge detector with a 0.8 s window width applied to the same resurrection data.

Figure 4.8: (a) The resurrection trace for a 1 μm beads in 2.5 mM sodium shows the output from a Chung-Kennedy filter with a 5 s window. Upward and downward steps detected by the algorithm are overlaid. (b) Many more short steps were detected in the same data using a window width of 0.8 s. These are marked on the figure up to the 4th level. Inset highlights the limited ability of the filter to separate out levels with a poorly defined edge. The resurrection step **R** is found, as are several other short timescale upward and downward steps, however there are clear changes in speed visible to the eye at **U** and **D** which mark the ends of speed levels, but these are not found by the algorithm. These are discussed below in conjunction with Figure 4.10.

Smoother transitions tended not to be passed as steps.

Interval Length Distributions

Interval length distributions of the steps between resurrection levels (Figure 4.9(a)) show mean upward step times $\langle t \rangle$ of 66 ± 11 s and mean downward step times of 160 ± 64 s. These times are assumed to describe the rate of stator binding and separation from the peptidoglycan at the periphery of the rotor, which defines the rate of exchange of stators at the motor. This is in good agreement with the preliminary results of Fluorescence Recovery After Photo-bleaching (FRAP)[7] experiments with fluorescent tagged stator units conducted by Mark Leake and Jennifer Chandler, which appear to show a single exponential dependence with a mean stator exchange time in the region of 1 minute (personal communication).

Considering the distribution of interval lengths for every level between found steps (without selecting for the direction of the step) in all of the data (Figure 4.9(b)) revealed a double exponential dependence, with mean times of 3.2 ± 0.1 s and 14.7 ± 1 s. I postulate that the 14.7 ± 1 s timescale process is a simple docking of the stator, as discussed in terms of de-resurrection (Section 4.4.2), during which time the stator remains attached to the peptidoglycan at the periphery of the motor but does not contribute torque. Since this reduction in torque does not involve stator exchange at the rotor it should not affect the results of the FRAP experiment. The 3.2 ± 0.1 s timescale process is likely to represent the mean time spent by the stator in the docked state, before returning to contribute torque at the rotor.

In summary, the stators of the chimæric flagellar motor bind to the cell wall at the periphery of the motor with a mean time of 66 ± 11 s and detach from the peptidoglycan with a mean time of 160 ± 64 s. Stators which are attached to the cell wall may remain attached to the peptidoglycan but detach from the rotor temporarily with a mean time of 14.7 ± 1 s. Stators in this detached state may remain detached for an average time of 3.2 ± 0.1 s before returning to the rotor to contribute torque.

Variance of Rotation Rate

Given that the Chung-Kennedy filter is intrinsically a running measure of the variance of the speed with rotation rate, I chose to plot the variance value from the

[7]Fluorescence Recovery After Photo-bleaching, whereby a motor with fluorescent stators is photobleached and the timescale of the stepwise fluorescence recovery at the motor implies exchange of stators.

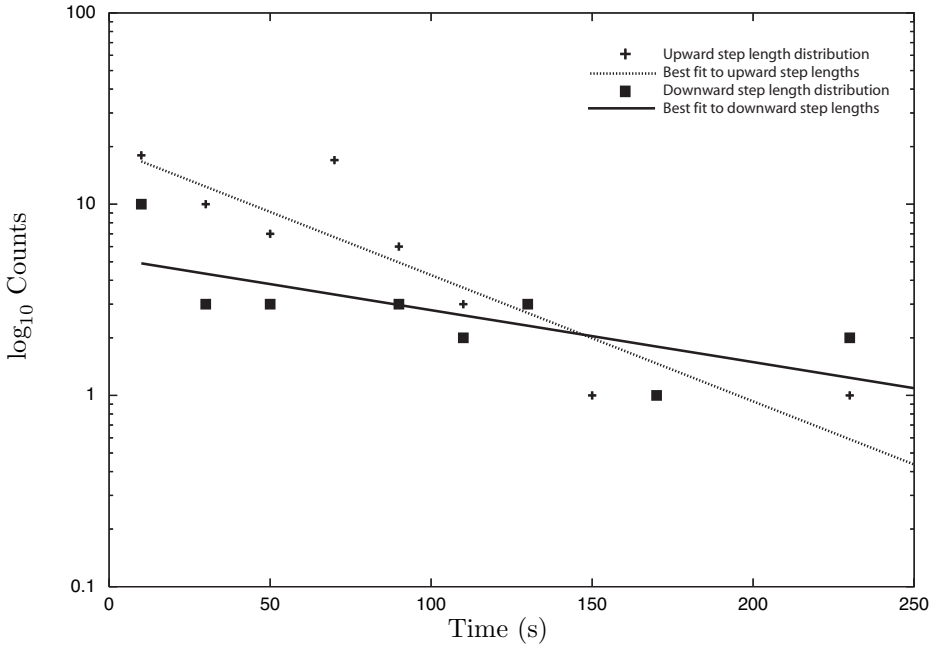

(a) Interval length histogram of forward and backward steps found in partial resurrection traces from 19 cells, using a 5 s window.

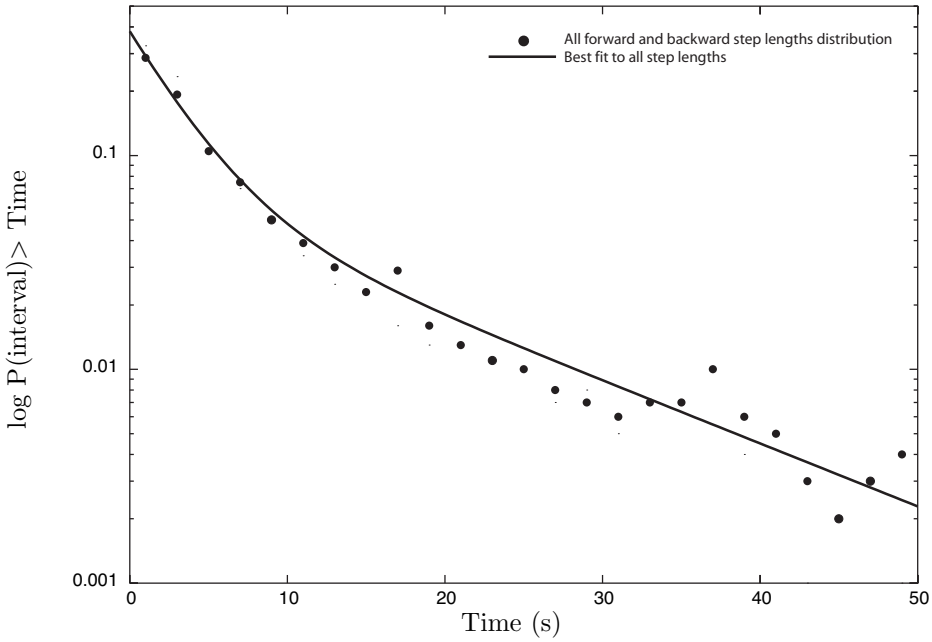

(b) Interval length histogram of all levels found in partial resurrection traces from many cells, using a 0.8 s window.

Figure 4.9: Step length distributions detected (a) The 67 forward steps and 27 backward steps detected using a 5 s window width were placed in 20 s bins on a histogram. The single exponential distribution implies mean upward step times $\langle t \rangle$ of 66 ± 11 s and mean downward step times of 160 ± 64 s. (b) The histogram of interval lengths for over 18000 upward and downward steps found in resurrection and continuous rotation rate data from many cells, using a 0.8s window. This shows double exponential dependence of the mean step times $\langle t \rangle$, giving values of 3.2 ± 0.1 s and 14.7 ± 1 s.

window containing the smallest variance against the mean rotation rate for that window (Figure 4.10), which showed bands of variance grouped by stator number. These data cannot be directly compared to the fluctuation analysis performed by Samuel [95, 96], since the variance measured differs between the two methods. Instead, it is being considered purely with regard to the failure of the Chung-Kennedy filter to detect changes in speed level which lack a sharp transition.

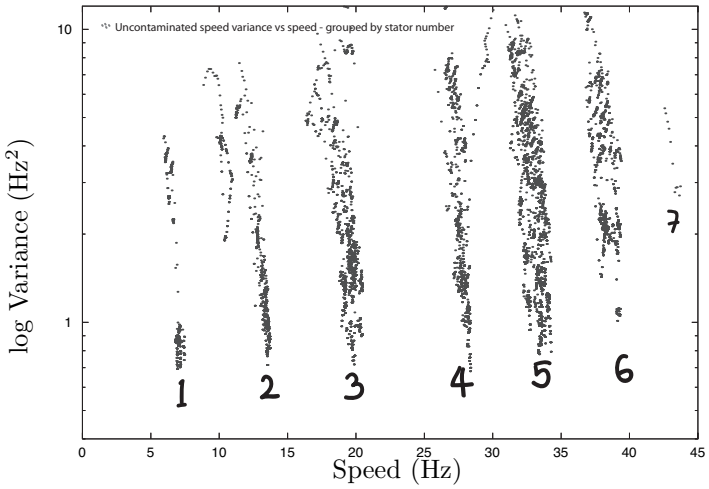

Figure 4.10: Uncontaminated variance for each point of the Chung-Kennedy filtered data in Figure 4.8(a) plotted against rotation rate shows bands of variance with speed for each resurrection level.

Close inspection of the inset to Figure 4.8(b) reveals that the speed data near the missed steps **U** and **D** is markedly more noisy than the data at the adjacent found steps. The large variance which goes with the noisy data at the missed steps inevitably causes the paired t-statistic from the filter passing over it to fall below the threshold of the step detector, thereby missing the step. If these noisy transitions between speed levels turn out to be systematic to chimæric flagellar motors, the filter used to detect steps will have to be adjusted to account for it. This will only be determined by comparison of this motor with the motors of new strains in the future.

Of some interest also is the gradient of the bands of variance vs speed for each stator. The implication of the gradient is that the rotation of a motor with a certain number of stators is most stable when all of the stators are contributing maximal torque. Why a stator should be unable to contribute its full complement of torque and therefore why it would destabilise rotation is, however, unknown.

4.4.5 Stator Integration

The unspoken assumption has always been that when a stator arrives at the rotor it immediately begins to contribute its full complement of torque, however the rotation rate change has never been investigated to greater precision than that allowed by a power spectrum method. An understanding of how stators affect the rotation rate as they integrate into the motor may shed light on the stator duty ratio, and therefore be an essential part of comprehending both the assembly process for the motor and the wider mechanism of stator torque generation.

By analysing the rotation rate of the motor in terms of the time period for each full revolution (Section 4.3.2) it was possible to attain a finer measure of the rotation rate of the motor during a resurrection process.[8]

The results of this analysis are shown (Figure 4.11 and discussion in caption). Comparison of the resurrection traces from 20 cells including a single resurrection trace for a WSR8 strain of *E.coli*[9] rotating 1 μm beads and analysed by this method showed speed transitions between low resurrection levels which occurred within a single revolution, implying potentially immediate generation of full torque by the new stator. At higher levels there was increased instability in the rotation rate during the stator arrival which caused the change in rotation rate to take place over several revolutions. At near full expression levels the change in rotation rate often took place over many revolutions.

It is not possible to assign a particular stator number to the resurrection level at which the speed increase between levels began to take more than one revolution, since there was considerable variation of rotational stability between individual cells at a given resurrection level. For the most stably rotating motors, resurrection transitions up to the 4th stator were generally immediate and subsequent levels showed increased instability with stator number. This trend appeared to be independent of the external sodium concentration. There was insufficient data to determine whether the trend was dependent upon bead size or rotation rate.

The generic mechanism of stator integration is not known. It seems reasonable to assume that there are three possible processes:

- The periplasmic MotB domain consistently finds a target site on the peptidoglycan at the periphery of the rotor, binds firmly to it and then the membrane

[8]The speed per rev had been measured before using video sampling rates to record the low (below 9 Hz) rotation rates of tethered cells [51], but not to measure higher rotation rate data acquired at much faster sampling rates.

[9]Original data from Stuart Reid.

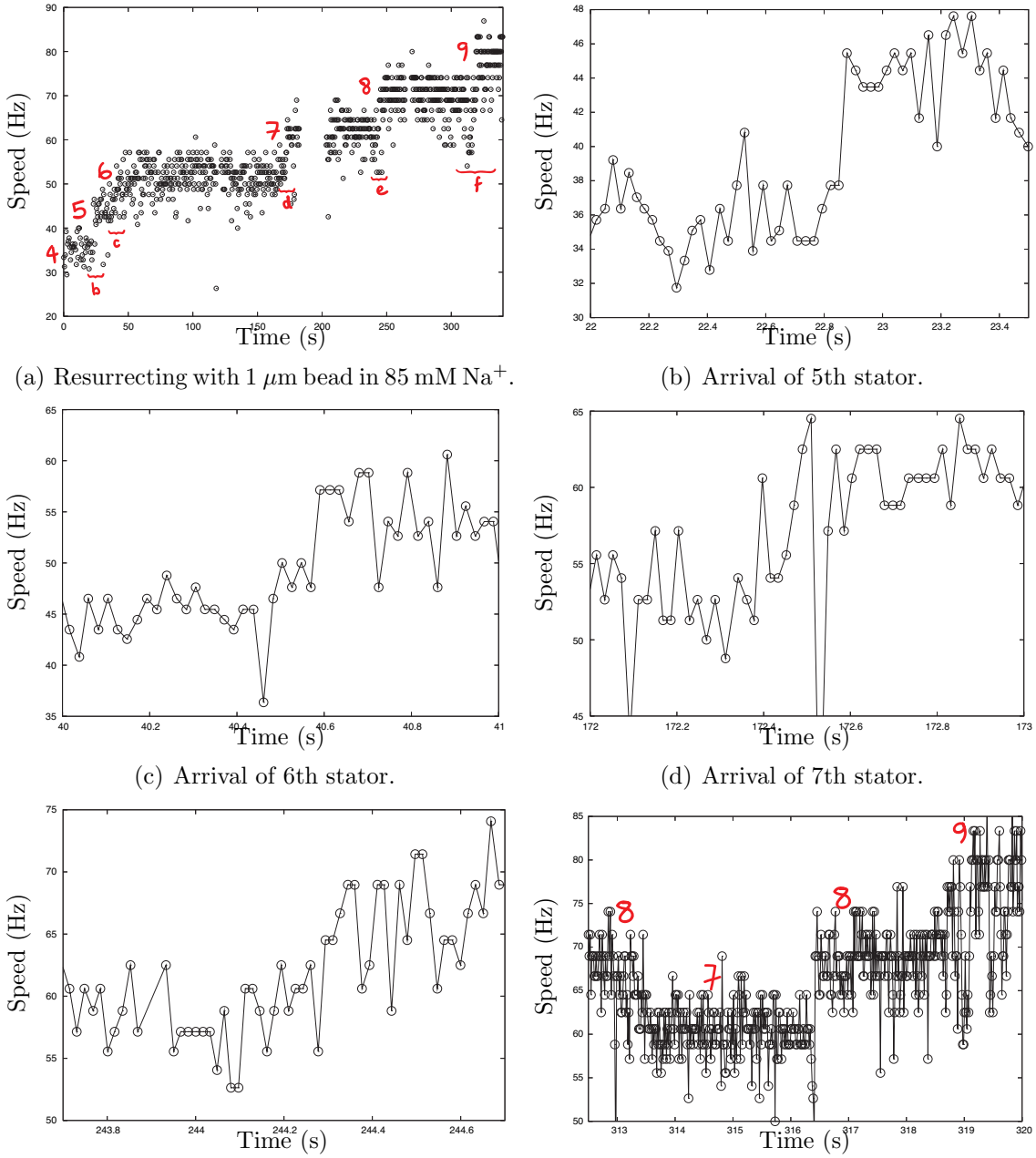

(a) Resurrecting with 1 μm bead in 85 mM Na^+.

(b) Arrival of 5th stator.

(c) Arrival of 6th stator.

(d) Arrival of 7th stator.

(e) Arrival of 8th stator.

(f) Arrival of 9th stator.

Figure 4.11: (a) A resurrection trace for a 1 μm bead in 85 mM sodium analysed by motor rotation period, shown resurrecting from the 4th stator level to the 9th. The interval between resurrection levels is around 9 Hz. Sections of the data where a step in speed occurs, corresponding to the arrival of another stator, are shown in subsequent panels. (b) The arrival of the 5th stator shows an increase of speed within 1 revolution, implying potentially immediate integration. (c) The 6th stator arrival shows full acceleration within one revolution, but its arrival is preceded by a brief drop in speed and is followed by greater rotational instability than earlier stators. (d) The 7th stator arrival demonstrates greater disruption to the rotation rate and what appears to be a relatively progressive acceleration over several revolutions to the higher level. (e) The trend continues for the 8th stator, with the acceleration time increasing further still. (f) With the 9th stator arrival the increase in rotation rate is very gradual and noisy indeed. This trend was consistent in the resurrection traces of 20 cells.

and cytoplasmic section of the stator swings into place and begins to contribute torque.

- The stator diffusing in the membrane arrives at the rotor, diffuses into an open space around the rotor, thereby perhaps loosely sterically associating itself to it before the peptidoglycan binding motif of MotB anchors the stator against the cell wall.

- Either or both of the first two processes can occur.

Whichever is true, the following postulate for stator integration should hold. With low stator numbers present, the chances of a stator arriving at an open space around the rotor are high. Given that the interval between peptidoglycan strands is around 1 nm it should be safe to assume that the MotB binding motif can attach itself at any point around the rotor, rather than being limited to a small integer number of binding sites. Thus by the first model, the chance of MotB binding to a point where the rest of the stator will interfere with an already bound stator is small. By the second model, the time between a stator arriving at the rotor and being dragged into another stator will on average be longer the less stators there are present; therefore the probability of the MotB binding to the peptidoglycan before the new stator interferes with existing stators is higher.

Extrapolating from here and comparing to the transitions shown, the arrival of a new stator when there are less than 5 stators present tends to be marked by an acceleration to the new speed within a single revolution.
As more stators arrive, there may be a preceding dip in speed, followed by a slower increase over several revolutions to the new rotation rate. This is often followed by some instability in the rotation rate for a while. As the number of stators present continues to increase, these instabilities become more pronounced and the time taken to reach a new steady speed extends further.

As a result of these observations I postulate a stator jostling mechanism, much like diners arriving randomly at a round table. There comes a point where a diner who is present has to stop eating to make space for a new diner. As the table fills up, these shuffling processes are likely to take longer as more people may have to shuffle round to make the last spaces available.

Thus newly arriving stators may diffuse into a gap and interfere with one or several neighbour stators, temporarily preventing them from coupling torque or affecting their duty cycle. The re-equilibration of this system would require a certain amount of creep in the stator-peptidoglycan interface for one or many of the inter-

fering stators. This is not beyond the bounds of reason given the on and off rates measured previously.

Chapter 5

Discrete Steps in Flagellar Rotation

This chapter reports the most significant contribution [109] of this thesis. The result is conclusive evidence of angular substeps in flagellar rotation whose size matches the symmetry of the proposed torque generating sites on the rotor.

The experiments were performed in two parts. The first set were carried out using BFP detection and were performed with Yoshiyuki Sowa. The second set were carried out with Mark Leake, some time later, upon the arrival of a high speed video camera.

5.1 Experimental Aims

The characterisation experiments of Chapter 4 were initially designed with one purpose in mind, this being to find a set of conditions at low load where slow single stator rotation could be reliably maintained. This would allow the search for stepwise fine structure within a single rotation to be conducted, thereby revealing how a single stator generates torque at the rotor.

As it turned out, these single stator slow rotation conditions were anything but stable, but despite this it was possible to study the fine structure of rotation as the motor passed transiently through the right conditions.

5.2 Experimental Techniques

All assay preparation was carried out as described in Chapter 4. Rotation measurements were first obtained by the BFP technique described in Section 2.4. Using a 1064 nm wavelength (λ) laser as a detector, the first limit to positional and thus angular resolution was the quality of the detector signal, which was dependent upon bead size. Experiment quickly determined that the smallest usable bead size was 0.5 μm diameter, roughly $\lambda/2$.

This placed the second limit on the experiment. For any fine structure to be resolved, the time between steps (which for the purpose of this experiment could be considered to be instantaneous at the rotor) was required to be long enough for the viscous load of the bead - rotating at an eccentricity of $\sim$150 nm from the rotor axis and coupled to the rotor by the elastic hook - to relax to the new step angle before the next step commenced. For a 0.5 μm bead this relaxation time was estimated to be 1.1ms without taking into account any excess drag contribution from the flagellar stub. On this basis, the maximum number of steps detectable per second was estimated at $\sim$900. In practice the value was more like 200 steps s^{-1}. On the assumption that the number of steps per revolution - should they exist - would probably match one of the symmetries of the rotor, average rotation rates of 7 Hz and below were judged to be good candidates for revealing stepping.

Slow rotation conditions were achieved by decreased smf due to low external sodium concentrations which forced de-resurrection (Section 4.4.2) and passed the motor through a condition of single stator rotation at below 7 Hz. In practice this was achieved by moving a partially resurrected motor from 5 mM sodium in which rotation was stable, into 0.1 mM sodium. Upon full de-resurrection, the cell was re-introduced to 5 mM sodium until one or two stators reassociated with the rotor. The cell was returned to 0.1 mM sodium and the rotation slowed to a single stator condition again for step detection (Figure 5.1(a)). In certain cells this process was repeatable, while in other cells the motor would stop irretrievably.

The second technique applied (Section 2.5 and Figure 5.2) used 0.2 μm fluorescent beads whose position could be calculated to $<$5 nm at 2.4 kHz from a 16$\times$16 pixel high speed video image. Estimates of relaxation time for the lower drag coefficient of the smaller bead meant that $\sim$1000 steps per second could potentially be resolved. The frame rate of video detection (2350 Hz) set the upper limit for step detection and cells rotating at speeds below $\sim$25 Hz were considered to be suitable candidates for step detection.

Slow rotation rates were achieved by smf reduction through photodamage, or

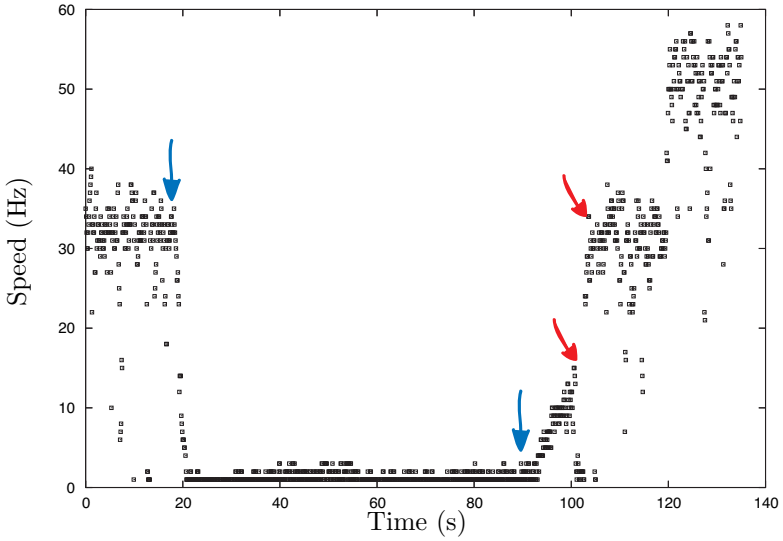

(a) Slow rotation conditions for BFP step detection.

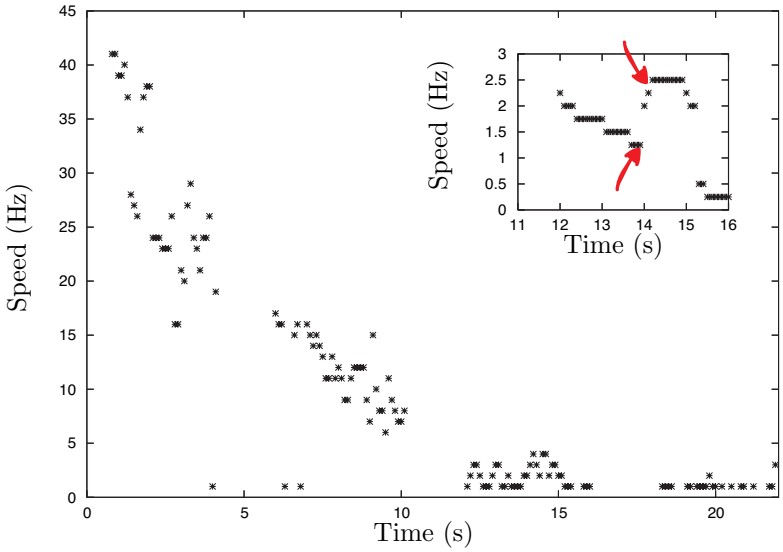

(b) Slow rotation conditions for fluorescence step detection.

Figure 5.1: Rotation rate versus time traces of slowly rotating chimæric motors for step detection. Red arrows indicate a speed doubling step, implying a single stator condition before the step. (a) 5 mM external sodium is replaced with 0.1 mM sodium at the first blue arrow and is returned at the second blue arrow. In between the slow rotation is shown to be driven by a single stator. This is proven by the speed doubling. (b) The smf reduced by photodamage causes motor rotation to decrease and deresurrection to occur. The inset shows a slowing in speed from a section of the main trace, with a speed doubling proving that single stator rotation was present. Steps were searched for in the rotation preceding the speed doubling and were also found after the speed doubling.

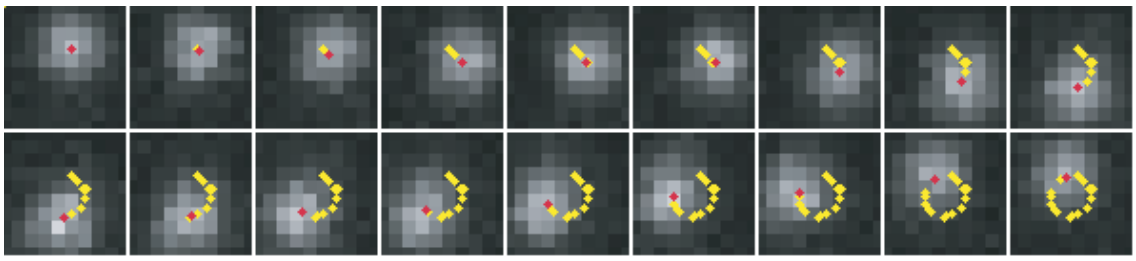

Figure 5.2: Selected 16×16 pixel frames at 21 ms intervals extracted from the high speed camera recording of a single rotation of a 200 nm fluorescent bead. The centre point of the fluorescent bead in each frame is marked in red, while the centres from previous frames are traced in yellow. The centre point is calculated to within 5 nm by the method discussed in Section 2.5. Each pixel represents an 80 nm square in the image plane.

opticution [39] discussed previously (Section 3.2.3), using the fluorescence excitation illumination. As the smf fell, speed fell and stator number reduced. At the lower speeds before the motor stopped, the rotation tended to be driven by a single stator as is proved by the temporary presence of a second stator doubling the rotation rate (Figure 5.1(b)).

5.2.1 Step Detection - Analysis Methods

The simplest method used for step detection was to histogram the angular positions over many revolutions, having corrected for the elipticity in the signal caused by the rotational plane being tilted relative to the detection plane (Section 2.4). A power spectrum of this histogram revealed the periodicities present.

Beyond this, the pairwise distance distribution function (PDDF) [110] was decided against because of the exponential increase in computation time with data volume. Given that many hours of data sampled at several kHz were being searched, this was impracticable. The Chung-Kennedy method [106] was considered briefly, but the method finally used for the bulk of the analysis was developed by Richard Berry, based on communication with J.W. Kerssemakers (Rijksuniversiteit Groningen, Netherlands).

The algorithm was as follows. First, an entire episode was divided into two intervals at the point giving the best least-squares fit to a single-step function. Second, an excess of steps (N_{max} per revolution on average) was assigned by repeatedly dividing, as in the first step, the interval containing the largest range of angles in the previous iteration. Third, a "quality factor" Q was defined for each assigned step

as $Q^2 = (x_1 - x_2)^2/[(var._1/n_1) + (var._2/n_2)]$, where x_i, $var._i$ and n_i are the mean angle, the variance and the number of points in an interval, respectively, and $i = 1$ and $i = 2$ indicate intervals immediately before and after a step. The lowest-quality step was removed and adjacent intervals were concatenated, but only if the quality was below a threshold Q_{min}. Last, the previous step was repeated until no steps remained with $Q < Q_{min}$. The accuracy and sensitivity of the algorithm were tested and a suitable value of Q_{min} for each episode was chosen by applying the algorithm to simulated data with N_o = 10, 20, 30, 40 and 80 poisson-distributed steps per revolution and with brownian noise and average speed similar to real data.

Fluctuation analysis

Analysis of variance was implemented by Richard Berry to ascertain whether the raw data for a particular cell should be expected to contain steps.
The variance across a range of time scales was calculated for the data and the plot of variance vs sampling interval for the position of a bead, with drag coeffiecient f, attached to a flagellar stub of stiffness k being rotated by a poisson stepping motor making d steps at angular velocity v, has been shown to have the form $a(1-e^{-bt})+ct$ where $k = 2/a$, $f = k/b$ and $d = 2\pi v/c$, (Figure 5.3).

By deriving the ratio, k/f it was possible to make an immediate assessment of whether the relaxation time for the bead on stub would be short enough to resolve rotor stepping from the bead signal. The result for the number of steps d was not so clear. The estimated values from the data were far too large. The source of this deviation in the long term trajectory of the rotor is unclear, but is attributable to some extra noise in the system, potentially contributed by the presence of extra stators.

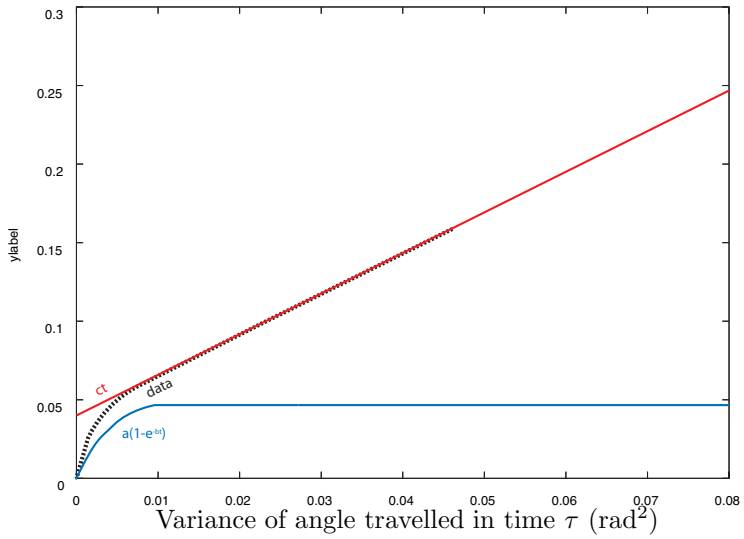

(a) Components of variance vs time curve for fluctuation analysis.

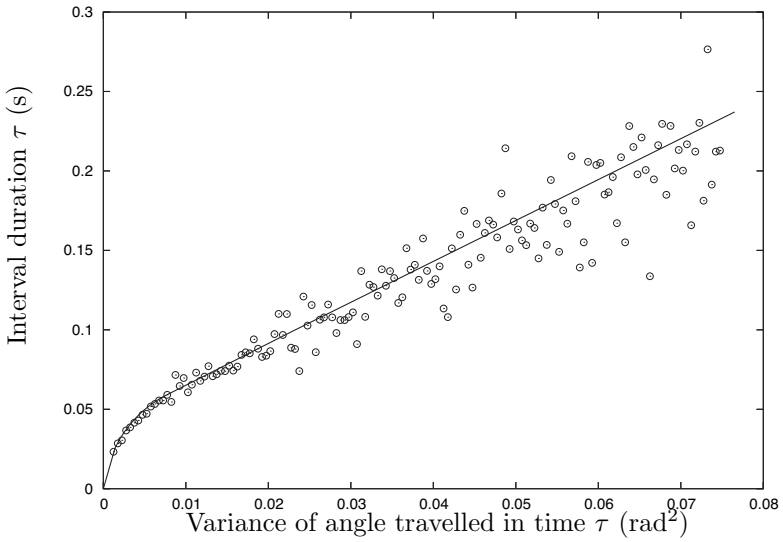

(b) Fluctuation analysis of slow rotation.

Figure 5.3: (a) A plot of variance vs sampling interval for the position of a bead, with drag coeffiecient f, attached to a flagellar stub of stiffness k being rotated by a poisson stepping motor making d steps at angular velocity v, has been shown by Richard Berry to have the form $a(1 - e^{-bt}) + ct$ where $k = 2/a$, $f = k/b$ and $d = 2\pi v/c$. The components of the data curve have been divided into the curve for a bead diffusing on a flexible stub which cannot rotate (blue) and the curve for an angularly diffusing body (red). (b) The variance analysis for a slowly rotating bead can be seen to follow the pattern shown. This implies values of $k \sim 60$ kT rad^{-2} $f \sim 0.5$ kT s rad^{-2}. These are close to ideal values for step detection.

5.3 RESULTS

Here I present the conclusive results of this work. Previous to this point, stepping motion in the flagellar motor had not been recorded on account of the high speed of rotation, the large number of torque generating units present, limitations in detection techniques and the small size of any potential step.[1]

5.3.1 ANGLE VS TIME

Using either the positional signal from the BFP detector (Section 2.4), or the fluorescence image on the high speed camera (Section 2.5) whose centre was tracked (Figure 5.2), the angular position of the bead label was plotted against time at a range of speeds within the step detection range (Figure 5.4) clearly showing discrete dwell angles within a single revolution. It is important to note at this point that steps were also seen in rotation episodes where more than a single stator were judged to be present. The implication of this will be discussed later.

Given that the YS34 strain has a CheY deletion,[2] the motors were expected to rotate in a forward direction only. The presence of backward steps (Figure 5.5) in the angle versus time trace, the probability of which decreased as rotation speed increased, indicated microscopic reversibility within the stators. This is reminiscent of the more occasional backward stepping seen in both linear and rotary ATP driven molecular motors [111, 112]. The probability ratio of forward to backward steps (P_f/P_b) is set by the free energy (ΔG) available to drive a forward step, such that $P_f/P_b = e^{-\Delta G/kT}$. The free energy available during phases where stepping was visible is estimated to lie in the range between 0 and -75mV of smf, equivalent to 0 to $3kT$.

A simple linear histogram of the angle vs time data overlaid for several revolutions (Figure 5.6(a)) shows clear dwell angles around the circle. The power spectrum of the logarithm of this histogram shows a clear peak at 26 per revolution with con-

[1] This is true if the motor is presumed to step with an interval defined either by rotor symmetries (26 or 33 being the most likely candidates) or by calculating the proportion of a revolution contributed by a single ion transit through a stator. 1000 to 1200 ions pass through the 10 to 12 stators of a fully functional motor per revolution [81] which implies an angular contribution of around 3° per stator per ion. Furthermore, by the conservation of energy, the maximum angular contribution of a single ion (θ_{max}) is dependent upon the free energy per ion (ΔG) and the maximum torque generated by a single unit (τ_{max}) by $\theta_{max} = \Delta G/\tau_{max}$. Given that the wild type protonmotive force is roughly -150mV ($6kT$) and that the high level torque of a single stator is in the region of 280pNnm, $\theta_{max} \approx 5°$.

[2] This is the switching signal protein and without it motors rotate smoothly in a forward swimming (CCW when viewed from the distal end of the filament) direction.

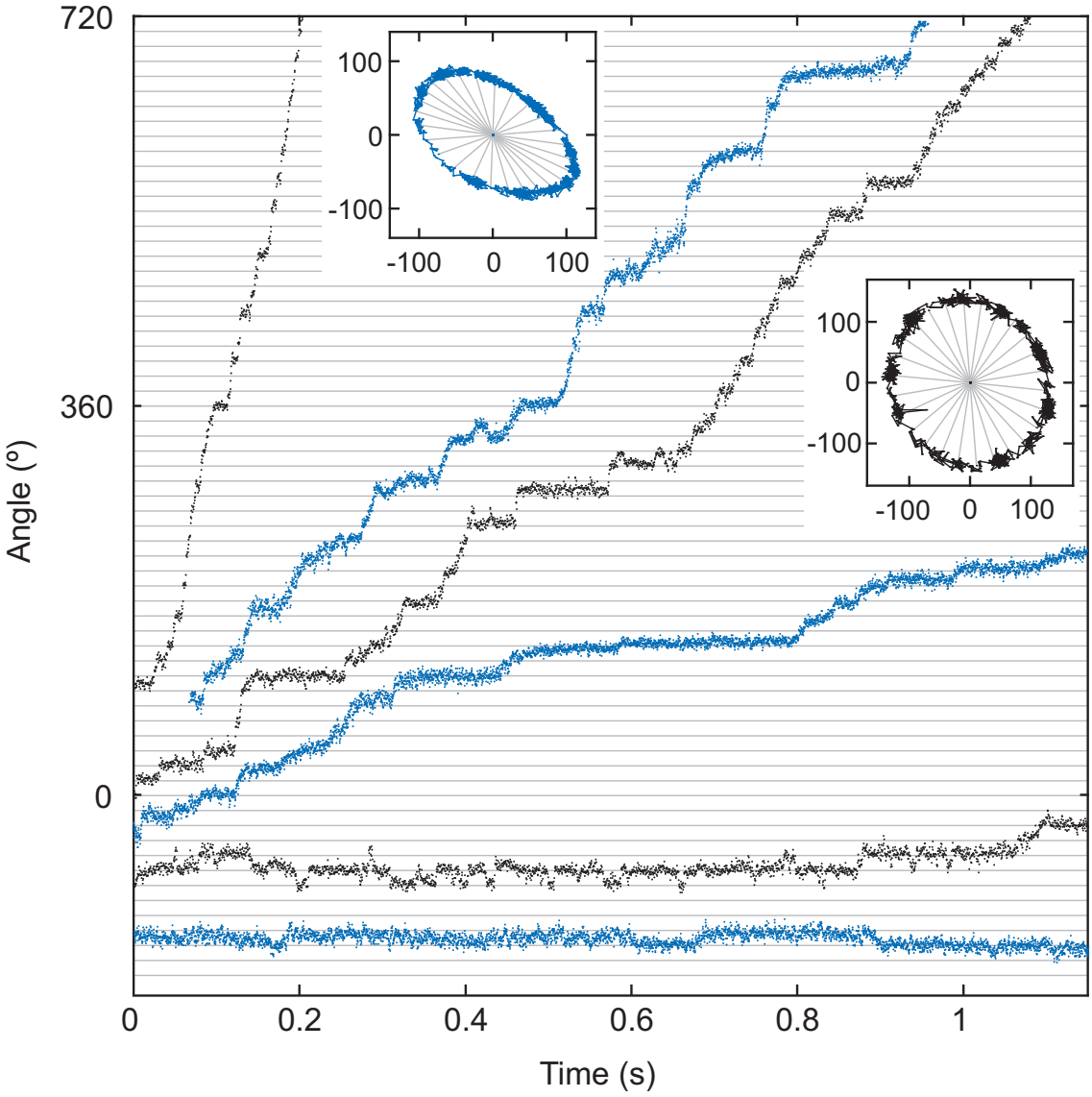

Figure 5.4: Steps in a range of slow rotation rates for the flagellar motor from both BFP detection (blue traces) and fluorescence (black traces). The positions of bead centres are shown in the insets (nm scale), while bead angles are plotted against time in the body of the figure. Backward as well as forward steps were seen at all speeds. Grey gridlines to guide the eye are shown at 26ths of a revolution in both the main and inset figures.

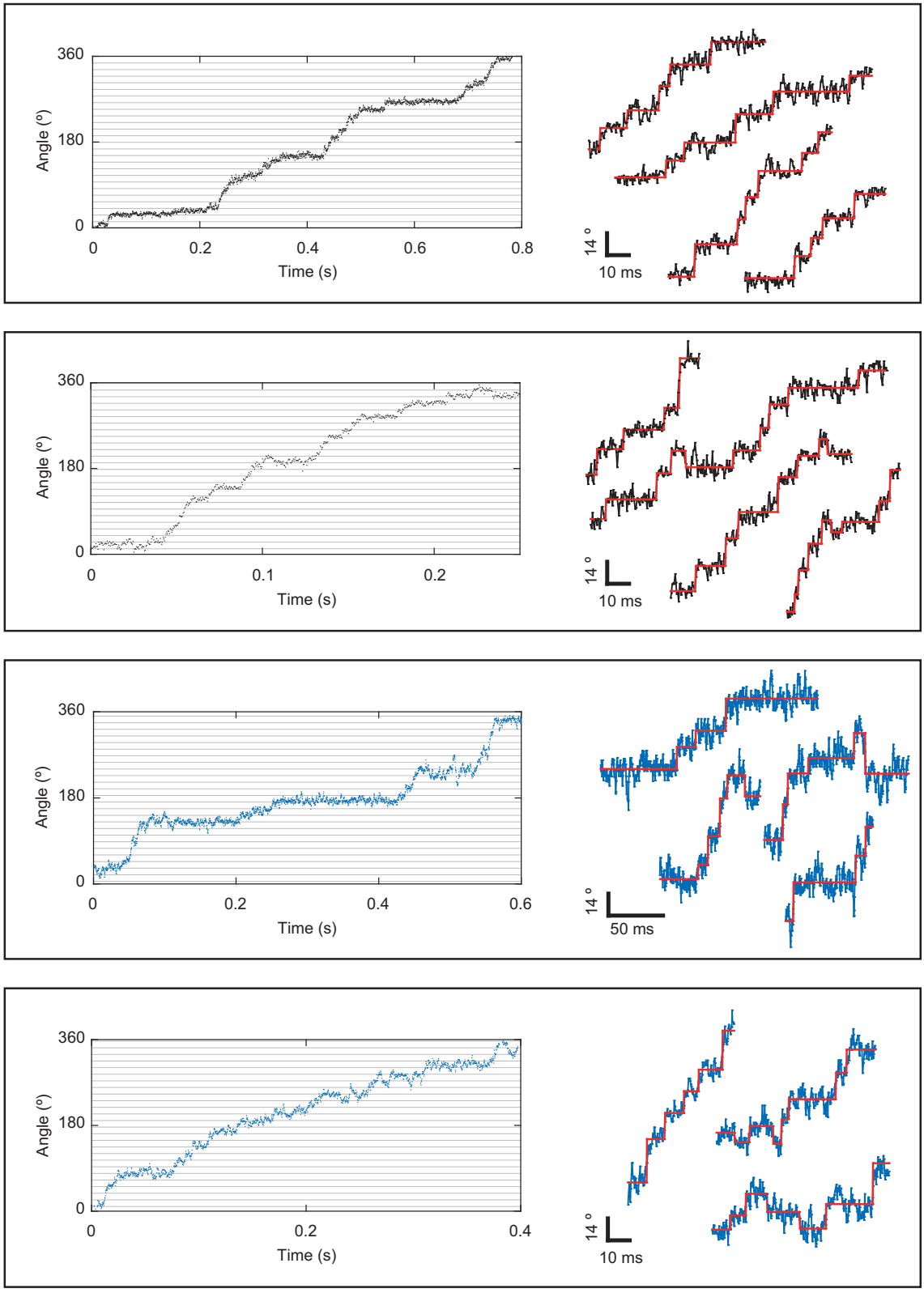

Figure 5.5: Steps detected at four different rotation rates by both BFP detection (blue traces) and fluorescence (black traces) in single rotations. The angular position is shown vs time for each rotation, while segments of the rotation are shown in the same panel with the output of the step detector overlaid in red. Occasional backward steps can be seen in three of the four traces.

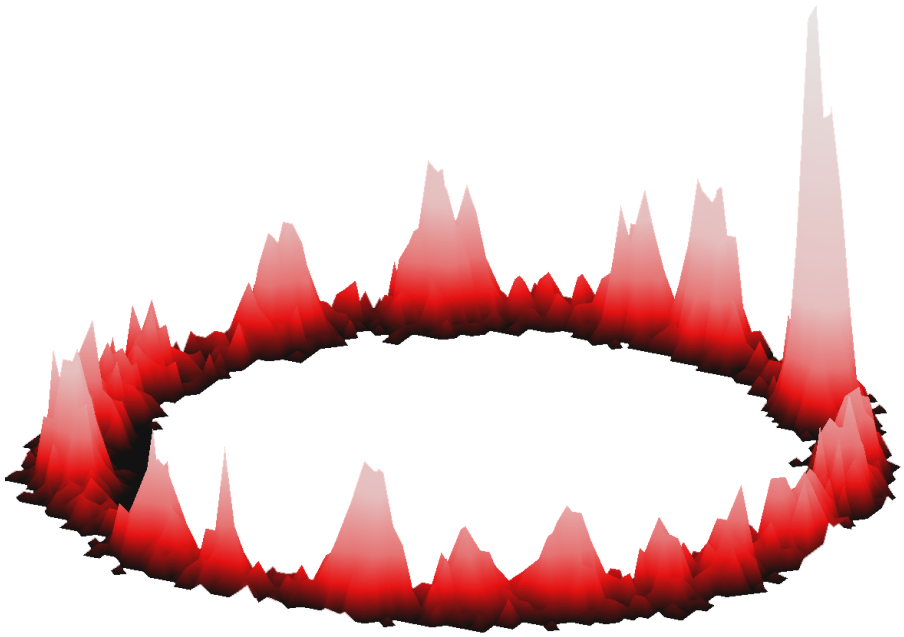

(a) Dwell times histogram for consecutive revolutions

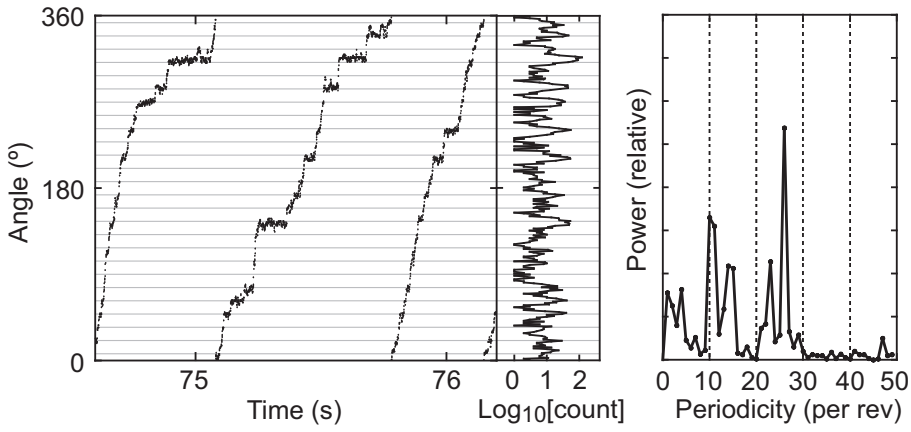

(b) Rotational dwell times histogram for several revolutions

Figure 5.6: (a) Linear histogram of the raw positional data from the fluorescence experiment over three consecutive revolutions. (b) The angle vs time trace for the same revolutions is histogrammed logarithmically. The power spectrum of the histogram is shown with the strongest peak at 26 dwells per revolution, equal to 13.8° intervals, confirming that the motor stops at the same angles on successive revolutions.

sistency over several revolutions. This indicates that the rotor stops at the same angles over many revolutions, thus linking the periodicity directly to the rotor.

5.3.2 Step Sizes

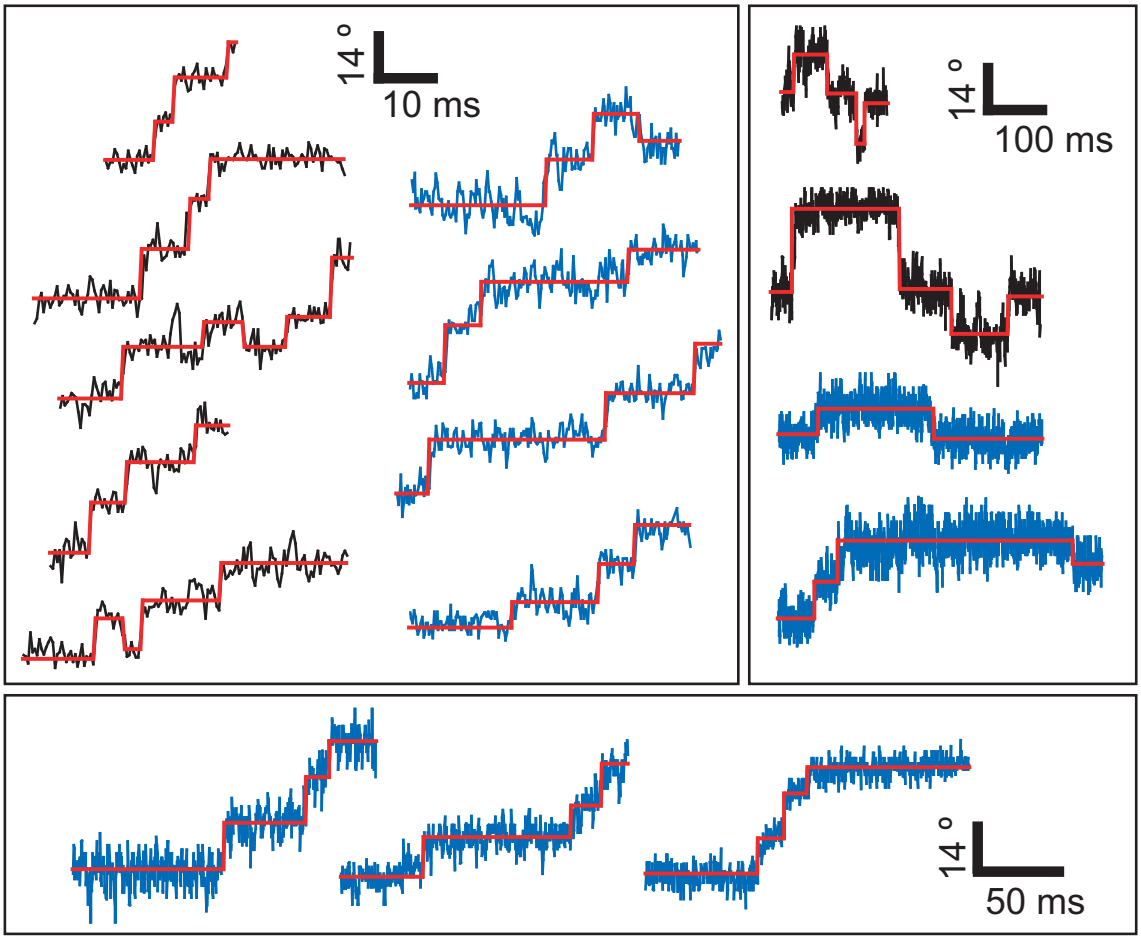

Figure 5.7: Detected steps from sections of the traces in Figure 5.4 with the output of the step-finder overlaid in red. Blue traces are from BFP experiments and black from fluorescence. The dominant step size is in the region of 14°.

Angle vs time data was divided into steps using the algorithm discussed (Section 5.2.1). The sizes of steps were measured (Figure 5.7) and the assumption was made that larger steps were multiples of unresolved small steps.

The magnitude of many steps taken from 9 cells during episodes of similar rotation rate were calculated and placed on a histogram (Figure 5.8(a)). The best fits of multiple gaussian distributions show a forward step size of 13.7°, implying 26 per revolution and a backward step size of -10.9°, equivalent to 35 per revolution.

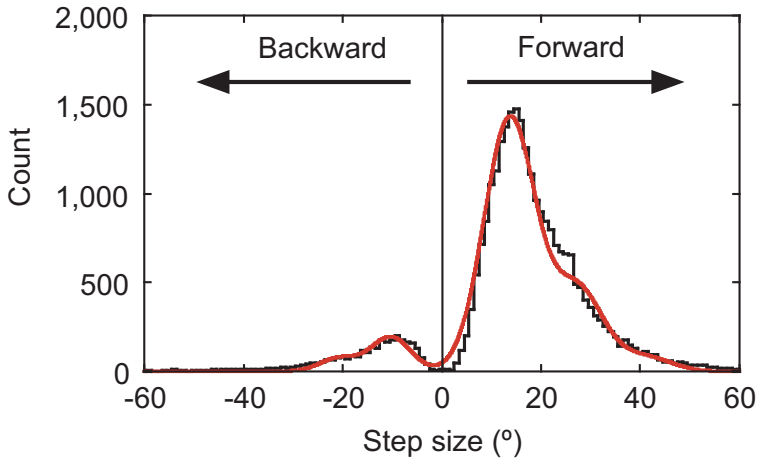

(a) Steps size distribution.

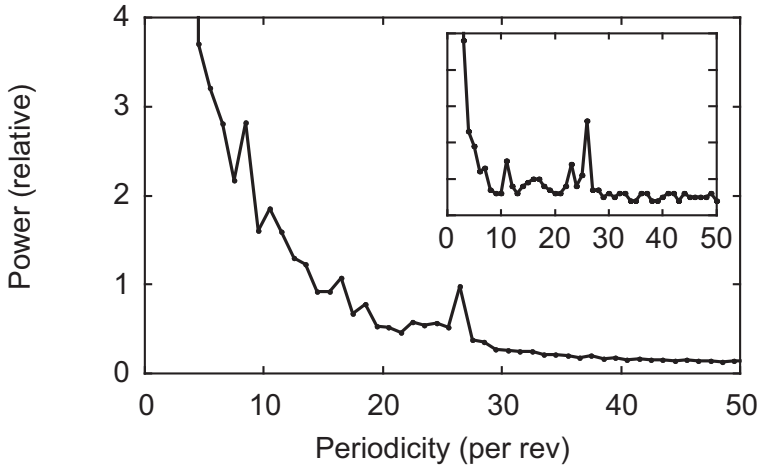

(b) Power spectra of angular dwell time histograms.

Figure 5.8: (a) The sizes of 28,611 steps from a data set comprising 9 cells and 1400 revolutions at a roughly constant speed are histogrammed and a multiple gaussian fit is overlaid in red. Fit results give a step size of 13.7° ($\sigma = 5.16°$) and -10.9° ($\sigma = 3.9°$) for forward and backward steps respectively. (b) The sum of histogram power spectra for the same data set, with inset, the summed histograms of the mean values of levels between found steps. All of these results confirm the presence of 26 forward steps per revolution.

The difference in size between forward and backward steps is not directly explicable. There are many possibilities. A reorientation of the rotation axis on reversal may be the cause, or it may merely be an artifact of the detection and analysis. By way of speculation, if the basis of the symmetry mismatch rotation model [113] is considered,[3] there is the possibility that some slack exists in the FliG multimer of the C-ring, which could allow individual proteins to slip from one site of preferential association with the 34-fold repeat of the FliM to an adjacent site. The size of this interval closely matches the average size of a backward step. Similar results would be apparent if the stator is displaced the equivalent of $\sim$1.4° from its anchor point during stepping in one direction, due to some slack in the binding, a backward step would carry the stator -2.8° in the reverse direction and register a smaller -10.9° step at the detector. Currently there are too many viable possibilities to make a definitive statement.

The sums of the power spectra across the data set comprising similar rotation rate episodes display a clear peak at 26 per revolution (Figure 5.8(b)), while the power spectrum of the mean levels derived from the step finder (Figure 5.8(b) inset) shows a similar peak at 26, alongside smaller peaks at 11, 16 and 23 per revolution.

5.3.3 Conclusions and Discussion

Comparison of the data between different cells, different techniques and different speed episodes shows that the step size and the angular periodicity are independent of the cell, the experimental method, any phase angle, rotation rate or stator number. Stepping is expected to indicate both the stochastic nature of the force generating process and the periodicity of the sites on the 'track' against which the motor couples torque [8, 111, 112, 19] and the persistent 26-fold repeat is in agreement with the symmetry of the ring of FliG proteins of the rotor, against which torque is generated [54]. The presence of other periodicities is not understood. The 11-fold repeat matches the symmetry of the filament and the hook [74], therefore the other periodicities may be due to interactions between some other currently unknown symmetries within the rotor or its bearing structure.

It is interesting to note that in some cases cells were found rotating far more slowly than should be expected for a given smf. When this occurred it was often after a sudden large change from high to low sodium, followed by a return to high sodium. The simplest possible explanation for this mode of rotation was that there

[3] This is based on a conversation I had with David DeRosier, an author of this model.

was a steric jamming of the motor by one or more stators or stator parts. The size of steps in this case was sometimes in the region of a 26-fold repeat, but was often slightly smaller, pointing to a 33-fold repeat. This matches the symmetry of the FliM repeat below the FliG on the rotor and it is not beyond the bounds of possibility that some rapid deformation of the cytoplasmic membrane under large sodium concentration exchange conditions[4] jams some part of the cytoplasmic PomA into the FliMs of the C-ring, hindering rotation. Since these steps were occurring in an undefined pathological condition they were excluded from the main analysis.

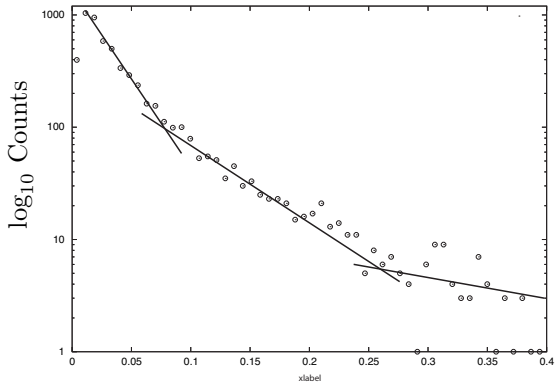

(a) Steps length distribution in speed episodes between 0.7 Hz and 1.7 Hz revolutions s^{-1} for a single cell measured by a BFP technique.

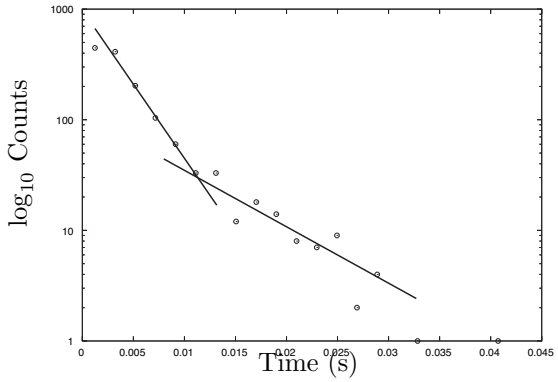

(b) Steps length distribution in speed episodes between 4 Hz and 7 Hz for a single cell measured by a fluorescence technique.

Figure 5.9: (a) Interval length distributions for collected episodes of rotation between 0.7 Hz and 1.7 Hz are shown for a single cell. Lines of best fit are placed on three segments of the data to guide the eye. The reason for the deviation from a single exponential is not understood. (b) Interval lengths for steps occurring during rotation at speeds between 4 Hz and 7 Hz also show a double exponential relation. Division of episodes into 1 Hz subsets of this interval revealed a similarly shaped curve.

Analysis of step interval length distribution within narrow ranges of rotation rates was inconclusive, never clearly conforming to a single exponential, even in cases where the rotation was believed to be driven by a single stator (Figure 5.9). This could be caused by rotation being slowed at certain angles due to bead interaction with the cell body, by the limitations of the step-finding algorithm being approached, or by some fundamental deviation of the motor mechanism from that of a simple poisson stepper. This observation - if it remains true for better quality

[4]Iso-osmolarity was maintained throughout the experiment with K^+, but energetics of *E. coli* suggest that internal potassium concentration is maintained independent from the external concentration, while the internal sodium depends on external sodium (see Section 1.4.3). This may cause some form of osmotic shock mechanism across the cytoplasmic membrane, which could deform it sufficiently to cause mechanical disruption of the stator proteins anchored in it.

step data - combined with the independence of step size from stator number and the observation of occasional smaller steps, may require modification of the currently held model of the flagellar motor as a set of independent poisson steppers [33, 95].

Another question, left as yet unanswered, is whether or not a single step corresponds to the passage of a single ion through the stator ion channel. As determined at the beginning of Section 5.3, a single ion transit under wild type rotation conditions corresponds to a maximum angle of 5°. This is well below the 13.8° for a single step seen during these experiments in near de-energised conditions. Potentially the stoichiometry of the system changes in conditions of low smf or stator number, but only a direct measure of smf under these conditions would indicate whether one should expect to see either substeps to the 13.8° steps reported here, or multiple ions being involved in one mechanical step as is supposed to occur during the ion driven rotation of the F_O portion of the F_1F_O motor during the synthesis of ATP.

Chapter 6

Conclusions and Discussion

'It is a good morning exercise for a research scientist to discard a pet hypothesis every day before breakfast. It keeps him young.'
Konrad Lorenz (1903-1989)

6.1 Conclusions and Contributions

Several novel technical contributions have been reported here. The high speed rotation detection of trapped particles [32] (Section 2.3) and the rapid medium exchange flow cell (Section 3.2.2), are certainly applicable to this field in the future and could conceivably be relevant to a broader bio-medical field. The need to characterise the dielectric properties of individual cells is ongoing and the potential combination of the electrorotation technique with a rapid exchange flow cell and laser tweezers could allow highly efficient processing of this technique in a range of environments. Furthermore, given the recent production of fluorescent dyes which act as fast responding indicators of membrane potential and intracellular ion concentration, the tweezer and flow cell assay could also be applied to the measurement of transient responses of cellular energetics between steady state conditions, thereby opening up a fresh and important path of enquiry.

The high angular resolution techniques employed here (Sections 2.4 and 2.5) are not novel in themselves, but are adaptations of existing techniques. In the case of the fluorescence based experiments, these employ the advances of the latest high speed video technology in order to take positional and temporal resolution to a previously unachieved level of sensitivity. One drawback of the video technique is the computer

processing time required to analyse the data.[1] However the advantage over a BFP technique far outweighs the long processing time by greatly increasing the precision available in tracking much smaller particles, thereby improving the temporal resolution of the system. Techniques involving high speed video will therefore become increasingly standard, as the maximal frame rate of cameras improves further and computation power increases.

Alongside the techniques development, there are several valuable experimental results shown.

V. alginolyticus Torque-Speed Relation

The torque-speed relation for the *V. alginolyticus* strain (Section 3.3.2) validates both the results of Sowa [65] and the rapid exchange flow cell technique through good agreement of the results. Additionally the torque-speed relation for cells cultured and maintained in 300mM sodium rather than 50mM sodium (Section 3.3.3) indicates a systematic variation in the total sodium motive force which scales with the sodium concentration of the long term surroundings. Whether the additional smf is generated by a greater number of Na^+/H^+ antiporters present in higher sodium conditions, whether it is due to a direct electrogenic extrusion of sodium as well as protons by the respiratory chain at higher sodium levels [67], or perhaps some combination of the two remains to be discovered.

The consistency of the exponential decay characteristic for rotation rate change on transition between sodium levels (Section 3.3.4) points to the rate of diffusive exchange between the periplasm of the cell and the surrounding medium through the outer membrane.

Chimæra Motor Characterisation

The chimæric motor has been characterised in a wide range of conditions and several general processes have been identified which merit both further investigation and integration into complete models for motor assembly and function.

The number of stators has been clearly seen to exceed 8 and to have been up to 12 in certain motors (Section 4.4.1). This value is in agreement with previous estimates [114], and the speeds attained show that the chimæric motor functions in the *E. coli* background cell much like the original sodium motor in its wild type *V. alginolyticus* background.

[1] This was about 1hr to analyse 3 seconds of data using my own analysis programs written in LabView on a 1.6Ghz processor.

The stated aim of the experiments with the chimæra motor was to derive a set of conditions in which slow consistent single stator rotation could be achieved. On the way to finding these conditions it became clear that the notion of continuous slow single stator rotation was a naïve ideal. The sodium dependence of single stator rotation, based on the interval between low resurrection levels in each sodium concentration, showed a rotation rate linear with $\log[Na^+]$.

However, an important, though as yet unquantified relation was discovered between the association rate of the stators to the rotor and the smf present. Until the smf can be measured accurately and simultaneously[2] there are few concrete conclusions which can be drawn. In short, the tendency of functioning stator units to temporarily dissociate from the rotor increases as the smf falls (Section 4.4.2). Conversely an increase in smf from a low level sees reintegration of the stator units to the motor. These characteristics have been termed de-resurrection and sodium induced resurrection respectively. Forcing de-resurrection of partially expressed motors became the optimal method for inducing temporary single stator slow rotation conditions.

The stator number and sodium dependent torque-speed relation for the chimæra was examined in part, though no clear conclusion can be drawn as yet. Due to degradation of the inducer which only came to light after the experiments were completed, it would be foolhardy to read too much into the original data, given its quality (Section 4.4.3). Analysis of the data by the method used to construct a similar relation for *E. coli* may have been instructive however, since it implies that the drag of the remaining flagellar stub is too significant for rotation to be measured in the high speed low torque regime beyond the knee point of the torque-speed curve using this assay. If this is the case, it is likely that a different detection system will be necessary to determine this curve in any valuable detail. The feedback controlled laser trap built by Teuta Pilizota in this lab is an ideal candidate for doing this and further work is planned along this line.

Analysis of the interval length distributions (Section 4.4.4) of levels during many resurrection traces revealed mean times for the arrival and binding of stators to the cell wall at the rotor, for unbinding from the cell wall, for periods of detachment from the rotor without unbinding from the cell wall and for the short time spent in the detached state. The long timescales defining the rate of exchange of stators at the motor are in good agreement with the preliminary data of Mark Leake and Jennifer Chandler (personal communication).

[2] I expect this to happen very soon on the basis of recent work by C-J Lo in this lab [103].

An important observation with regard to understanding the assembly of stators at the rotor was the short timescale rotation rate change during a resurrection step (Section 4.4.5). Standard analysis methods reveal a discrete step in rotation rate and the assumption has always been that a stator arrives and instantly contributes its full complement of torque, however consideration of the rotation rate for each revolution shows a different trend.

At low stator number the integration process occurs within a single revolution, in agreement with the standard assumption. However as the periphery of the rotor becomes more crowded the integration process becomes increasingly less immediate. There appears to be a jostling process taking place, whereby a newly arriving stator is only able to contribute partial torque because it is hindered by the presence of a nearby stator, or the new stator impedes the torque generation process of an existing stator. The time taken to re-equilibrate the distribution of the stators around the rotor to allow them all to generate full torque increases with stator number. The direct implication of this with regard to the duty ratio of stator units is not clear, however it must be taken into account in order to fully understand the mechanisms involved in motor assembly and rotation.

Flagellar Motors Step

The final and most significant contribution of this work combined the slow rotation rate conditions and the high resolution angular detection system mentioned previously to show that the flagellar motor rotates with 26 steps per revolution (Chapter 5). This was the first experimental resolution of steps in an ion driven molecular motor and is therefore the first result to directly validate stepping models for the bacterial flagellar motor.

The magnitude of the step is consistent with the periodicity of the site of force generation on the rotor and, though it is impossible to say how many ion transits are involved in one rotational step without measuring the smf concurrently (and therefore impossible to say whether one should expect to see substeps), this result represents a significant contribution to the field.

Furthermore, it was observed that the same number of steps per revolution appeared to be independent of stator number, which calls into question the validity of the currently accepted independent poisson stepper models. Whether this question is specific to the chimæra motor in general, this specific strain, or to flagellar motors as a whole will only be clarified by comparison between these results and those from natural motors and other chimæric strains.

6.2 Final Thoughts and Further Work

This study has opened several fruitful paths of enquiry.

The most obvious direct further work would be to search for steps in both proton motors and sodium motors with simultaneous measurement of the relevant ion motive force. This would clarify whether or not one should expect to see substeps to the 26 so far reported.

Technically there are many potential advances to be made. Stiffening of the flagellar hook would yield an immediate improvement in resolution, as would the reduction of drag. The average length of flagellar stubs left by shearing needs to be determined, in order to validate the assumptions currently used to fit the torque-speed relation, and this would be best done with either electron microscopy or perhaps an AFM.[3] If the stubs turn out to still be ~ 1 μm long then another way of producing cells with short, stiff flagella must be found. The final remaining optimisation would be the use of smaller biologically functionalised quantum dots as labels on the hook in place of the relatively larger beads currently used.

Very recently I worked on some preparatory experiments with Yoshi Sowa using an improved chimæra strain with the sticky filament on the chromosome rather than on a plasmid. The results of these are promising in themselves, however the relevant observation to this work was that the sodium driven motor seemed to rotate with greater stability than that used throughout my experiments. This may mean that the motor can be made to run for longer at slow rotation rates and any opportunity to perform these experiments with more stable motors should be taken.

It might also be instructive to perform the same experiments using a *Rhodobacter spheroides* cell, particularly if the stator association rate to the rotor is dependent upon the light sensitive pmf of the cell. This may be the key to a much needed understanding of the relation between the pmf and rotor stator association rate, which must be understood in order to gain full control of the motor.

As a final thought, I cannot help but feel that the rotation of these motors will not be clearly understood without both a crystal structure of the stators - a problem upon which many groups are bringing their considerable experience to bear - and the separation of the motor from the direct energetics of the cell.
This could be attained by either gaining access to the cytoplasm, or by physically extracting a motor. Neither of these is a simple process on account of the cell structure and the osmotic pressure inside the cell, however recent advances with

[3] The compliance of the flagellar hook may mean that an AFM is insufficiently sensitive to detect a flagellar stub on the end of it.

scanning probes, particularly by Yuri Korchev at Imperial College, suggest that now might be a good time to try.

Appendix A

Building and Tuning Laser Tweezers - A HOWTO

A.1 Building a non-commercial optical trap

The primary consideration when building a home-made optical trap is to ensure that the paths for the illumination, the imaging and the trapping beam all pass simultaneously along the optical axis of the objective lens that is being used.
Thus the first step in the process is to fix the objective permanently and to mark its optical axis with a laser beam.

A.1.1 Marking the optical axis

- Fix the objective lens in its final position.
  When fixing the objective it is advisable to leave roughly 150mm below it to accommodate the trapping beam path and the imaging path.
  The mounting for the objective should be as solid as possible, since any vibration of the objective lens will contribute a very significant amount of noise to both the trapping and any subsequent detection.

- Place the optics as shown in Figure A.1 to create a beam path from the laser to the CCD.
  M4 should be fixed bearing in mind that a dichroic mirror needs to be placed between it and the objective lens.

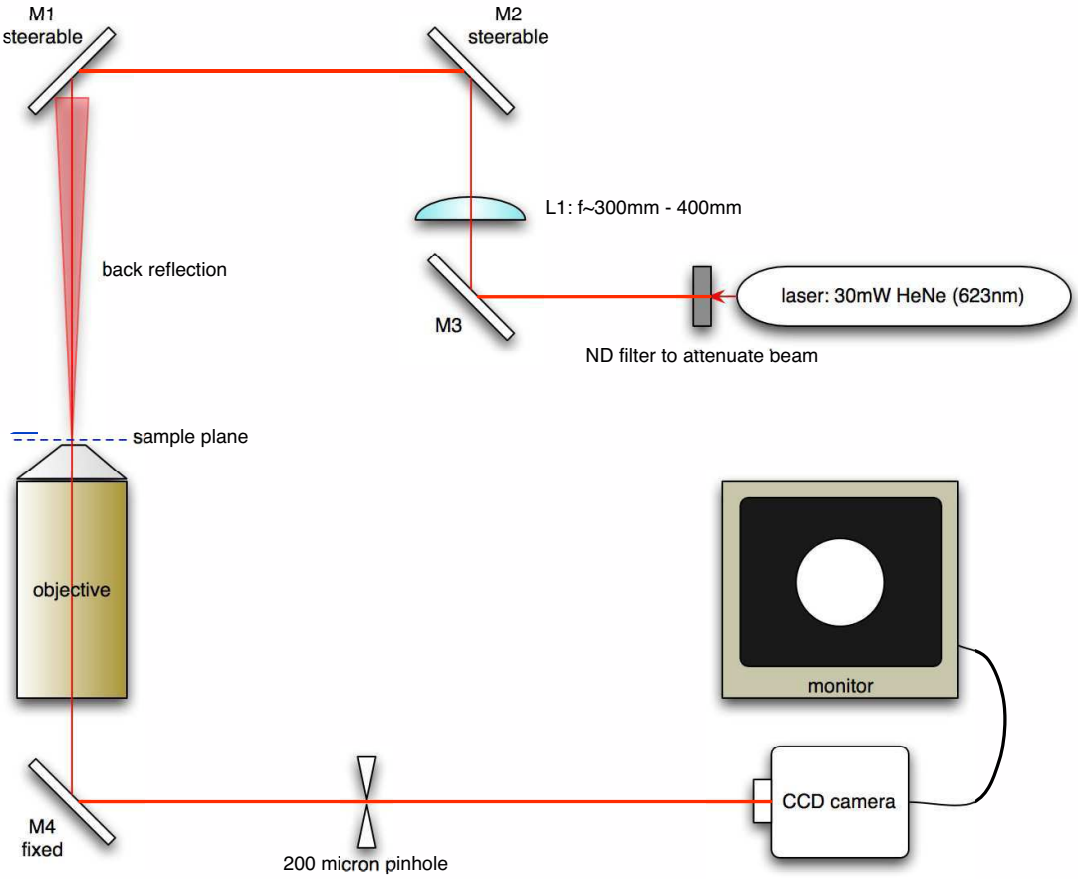

Figure A.1: Optics to align the laser beam with the axis of the objective lens.

L1 should lie approximately its focal length (300mm - 400mm) from the sample plane, such that it roughly focusses the HeNe light onto the objective.

- By steering M2 and M3 the position and angle of incidence of the laser on the on the objective can be adjusted. Once the beam is incident on the objective, the back reflection can be used as a precise measure of the angle of incidence. Only when the beam lies perfectly on the axis of the objective will the back reflection of the laser be indistinguishable from the incident beam.
  The back reflection is best tracked using a piece of paper with a small hole punched in it. Initially one needs to scan near to the objective to find the back reflection. As the beam becomes more accurately aligned one should scan further from the sample plane in order to detect the smallest misalignment.
  The final tuning can be done by adjusting M1 to maximise the intensity of the (probably diverging) beam transmitted by the objective.

- Once the incident beam lies on the axis of the objective, the objective can be removed from its mounting. A CCD (without lens) can then be placed at the end of the beam path. The position of the spot on the CCD should be marked on the monitor, as it constitutes one marker point of the axis of the objective. A 200 μm pinhole should then be placed across the beam such that it does not deflect the image on the camera.

At this point we have a failsafe marker of the objective's axis given that none of M4, the pinhole and the CCD are moved relative to the mounting for the objective.

A.1.2 Marking the axis in the image plane

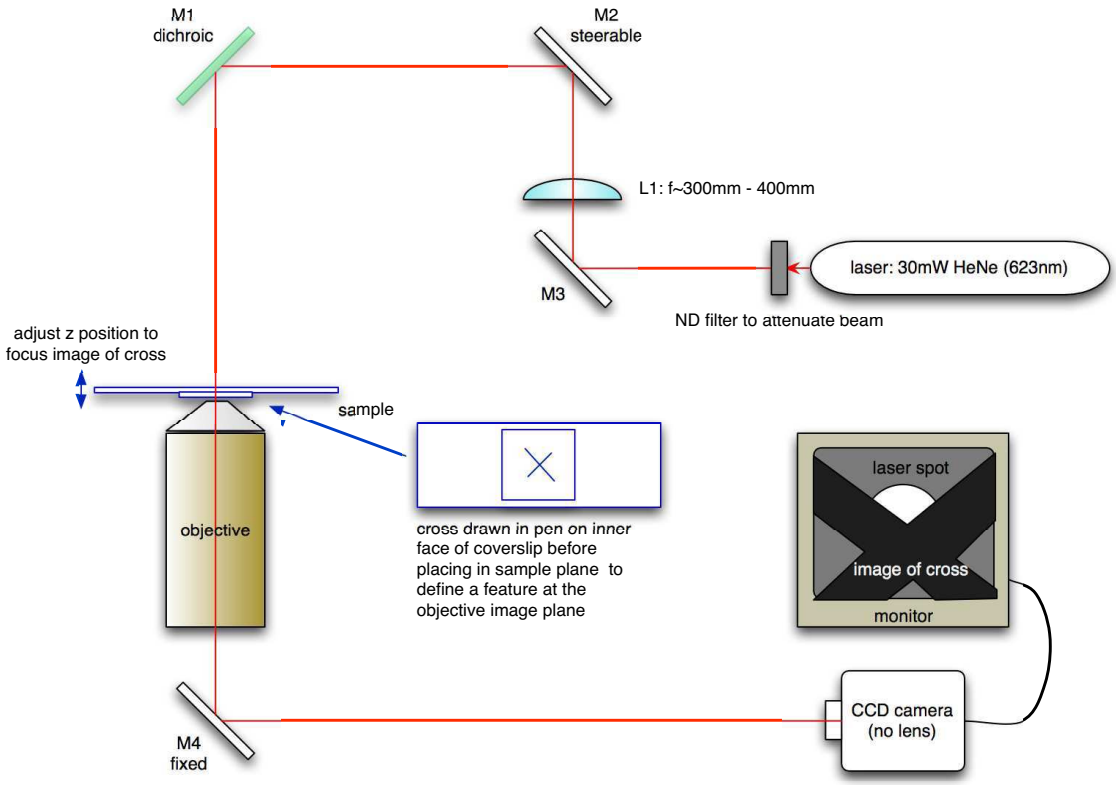

Figure A.2: Placing a recognisable feature in the image plane provides the most precise definition of the axis of the objective.

- In order to couple in the illumination at a later stage, M1 needs to be replaced with a dichroic mirror which will transmit light from above, but reflects infrared from the objective towards a detector.
  The correct alignment of the dichroic is confirmed by the laser beam once again passing through the pinhole and hitting the marked point on the CCD. With the dichroic in place the pinhole becomes redundant and can be removed. It is worth noting that there will be a secondary reflection off the back surface of the dichroic and it may well be necessary to block this.

- The objective can now be replaced and a sample as shown in Figure A.2 can be placed in the sample plane. This sample should resemble a standard experimental assay as closely as possible, hence the use of a tape tunnel slide containing water with the cross marked on the lower inside surface of the chamber. Immersion oil should also be used on the objective.

The sample position should be adjusted in x,y and z so that a recognisable feature such as the intersection of crossing lines lies in focus at a distinct point on the CCD. (see A.2 for ideal image on monitor)
Intense illumination will be needed to see the image if the laser is off or on a low power.

With the feature placed on axis in the sample plane we now have the most sensitive measure of axial alignment for any optics which are introduced further up stream of the objective.

A.1.3 Aligning the condenser

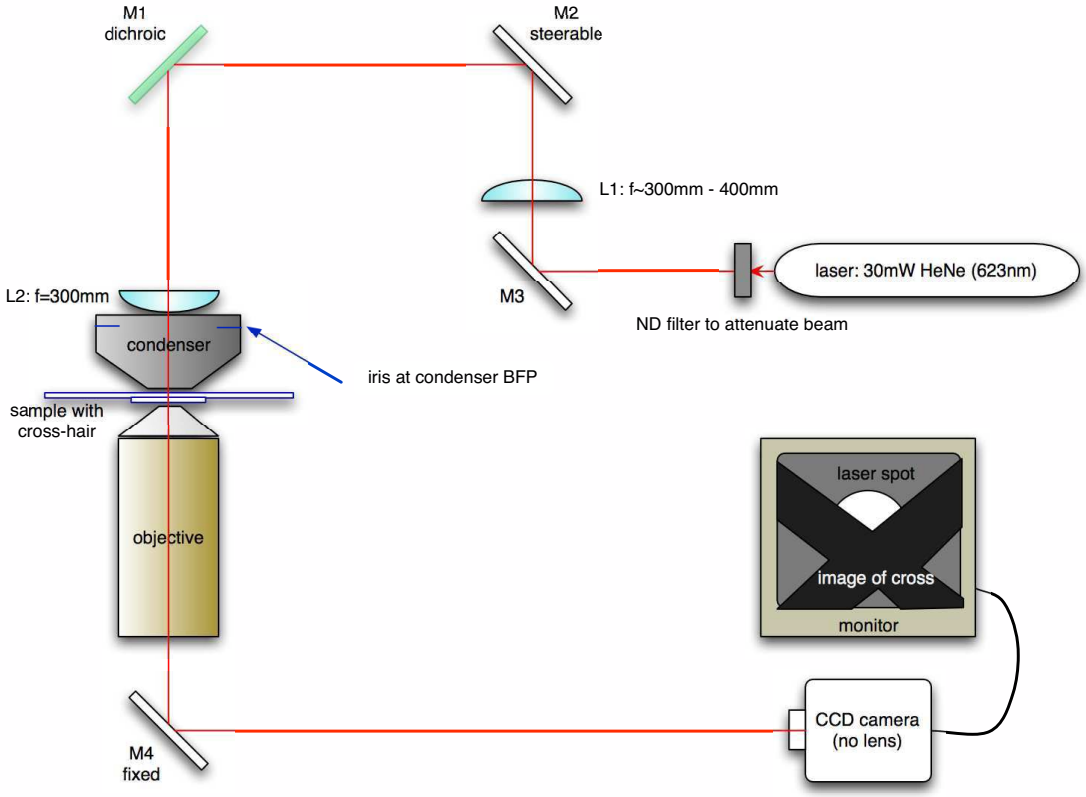

Figure A.3: Placing the condenser lens on axis.

- It is now necessary to place the condenser as shown in Figure A.3 on axis. First place the condenser approximately, them adjust it in z to form the image of the laser spot somewhere[1] on the CCD. Finally adjust its position in x and y until the spot falls in its original position on the CCD relative to the image of the feature in the sample plane.

- L2 must now be placed behind the condenser. Its function is to form part of the telescope to narrow the collimated beam of trapping radiation which will be used for detection.
  In the case of this system L2 is placed on the back of the condenser, adjusted in$x$ and y until it lies on the same axis as the objective and the condenser and then held in place with a few small dabs of glue.

[1]Since parallel light at the condenser back focal plane is imaged to the condenser axis, misalignment of the condenser axis and the objective axis will cause the image of the spot to be angularly deflected at the BFP of the objective and fall elswhere on the CCD.

A.1.4 Adding visible illumination

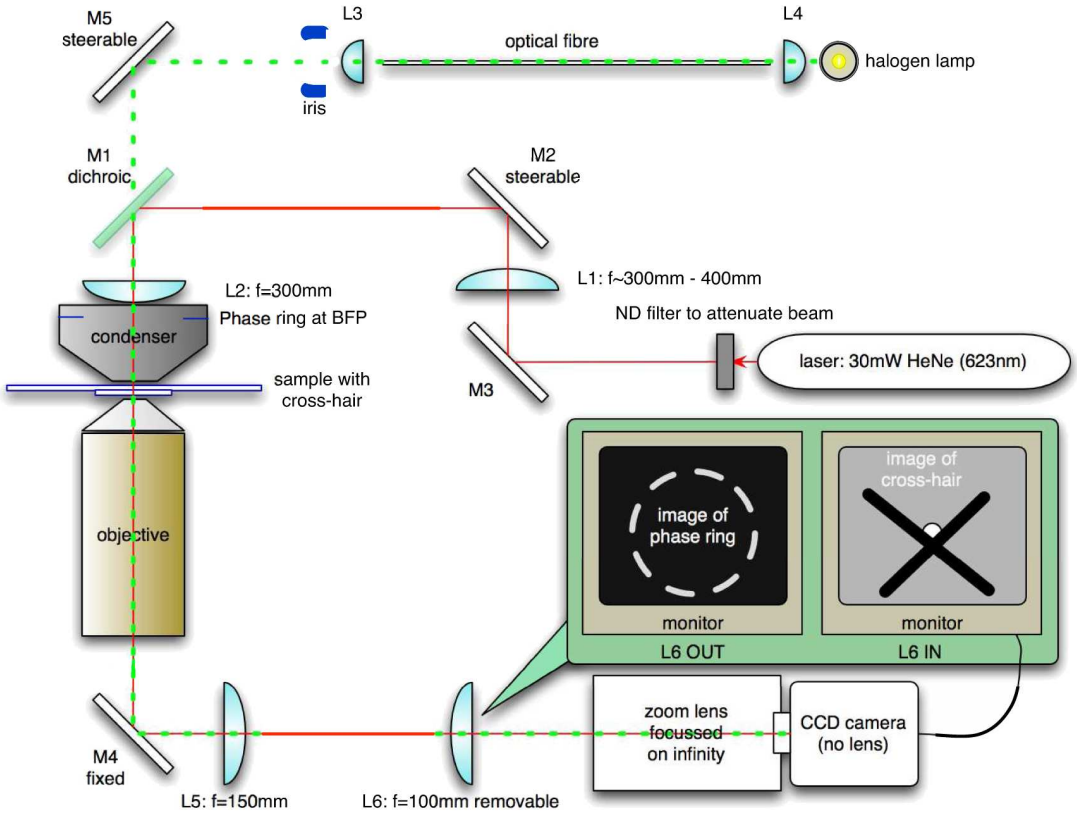

Figure A.4: Adding Köhler illumination and an imaging telescope.

The system is now ready for the visible illumination to be coupled in.
The preferred method of coupling visible light into the trap is by Köhler illumination. This involves using the light from a small source, such as the tip of an optical fibre and focussing it via an accurately positioned lamp condenser lens onto the back focal plane of the main condenser lens.
This system allows the main visible light source to be far away from the objective and the illumination to be coupled in via a flexible fibre. In this system the back surface of the lamp condenser lens acts as a uniformly illuminated large area light source. See Figure A.4.

A.1.5 Steering in the trapping beam

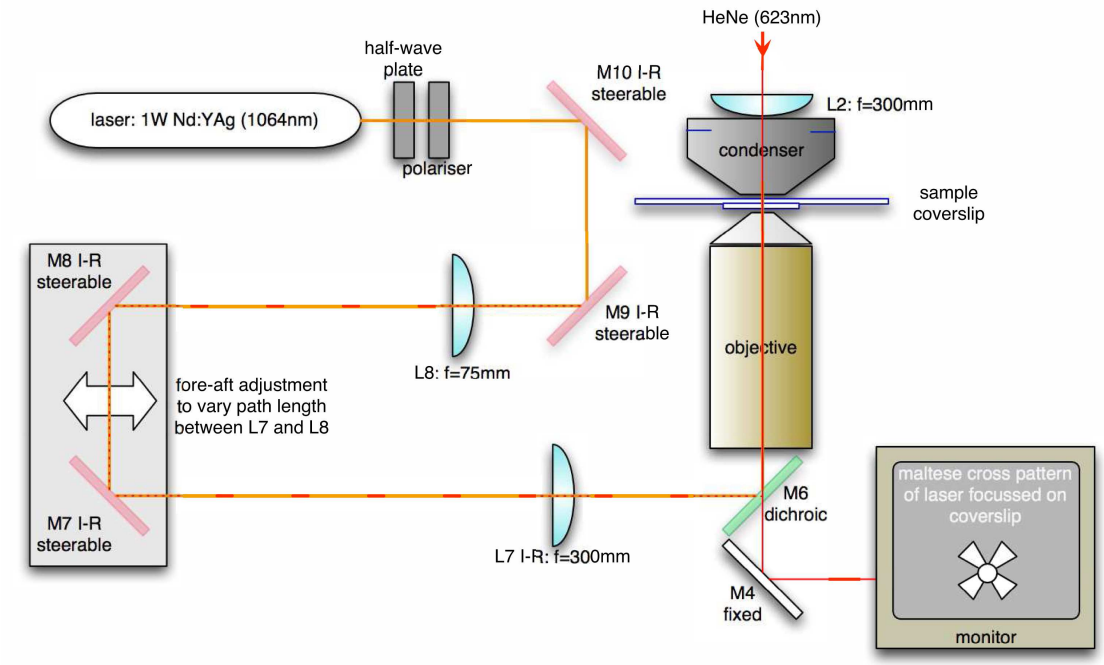

Figure A.5: Addition of the infra-red trapping beam.

With everything else aligned it is simply a case of steering the 1064 nm trapping beam into the back aperture of the objective along the optical axis.
A weak reflection of the HeNe laser from the dichroic below the objective is enough to align the beam broadening telescope and the steerable mirrors can then be used to steer the counter-propagating red and infra red beams into each other.
The job is essentially done when the two beams intersect at two separate points along the trapping beam path. See Figure A.5.

From here, fine adjustments can be made to the steering mirrors in order to refine the quality of the trap.

Appendix B

Microfluidics - Troubleshooting

For the purposes of passing on the experience gained during fruitless hours spent optimising a protocol to reliably and repeatably load and use a low pressure multiple channel microfluidic system, I have included the salient points here. I hope it is of use to someone somewhere...

B.1 Loading a multi channel flow cell

The essential problems associated with loading a reusable PDMS flow cell stuck to glass are twofold.
The first is that the seal to the glass is of limited strength, therefore high pressures cannot be used to drive fluid into the channels. The second is that the PDMS is naturally hydrophobic.

This means that loading the flow cell so that there are no air bubbles inside it can be a painfully long process. Furthermore, the hydrophobic nature of the PDMS means that the pressure requred to drive a fluid meniscus through a channel thereby wetting a path is much greater than the pressure requred to drive the fluid at the same rate through the wetted path.

PDMS can be bathed in HCl for several hours in order to make it more hydrophilic, but the result is a loss of adhesion to glass, making it easier to blow the seal at low loading pressures.

B.2 Flow Control Issues

The appeal of precise flow control using a syringe pump is obvious, however there can be drawbacks. If the dimensions of the microfluidics are sufficiently small the fact that the syringe pump is driven by a stepper motor becomes inescapable even with a narrow bore (not a Hamilton) syringe. This results in occasional pulses of fluid through the system, which is incompatible with the requirement for constant steady flow.
Attempting to damp the pulses by leaving a pocket of air in the syringe failed, since the pressure built up in order to drive the mensicus through the channel to wet it would be not be released until the requisite volume of fluid in the syringe had been driven through the flow cell for the air to reach a lower equilibrium pressure. The net result would be extremely fast flow which could not be finely controlled.
Thus the syringe pump can be a non-starter.

Usually the best approach to driving a fluid through the channels with sensitive immediate pressure control is to use gravity to create a head of pressure.
The problem arises when loading several channels. One would think that the pressures in adjacent channels would all drive the flow forward through the channel and into an exit. However this is not the case!
Adjacent flows emerging into the main chamber of the flow cell, rather than continuing through, can find that the path of least resistance is to equilibrate pressure between themselves rather than to continue wetting the chamber.

B.3 The Solution

The answer to this problem is to ensure that the resistance of each loading channel is the dominant resistance of the flow circuit. That way the head of pressure used to drive the flow can be very high and will ensure that there is no backward flow through the system.
In practice this is best done by having a section of the feed channels which can be crimped in a controlled manner until the requisite flow rates are achieved.

Good luck...

Appendix C

Bacterial Cultures, Growth and Motility Media

C.1 Culturing *V. alginolyticus* strain NMB136

The NMB136 strain was used throughout the main *V. alginolyticus* experiment (Chapter 3). The strain is a chemotaxis signalling protein CheY deficient smooth swimming mutant of the VI05, itself a $Pof^{+}Laf^{-}Rif^{r}$ (rifampicin resistant) strain [115].

Glossary of relevant terms:

Laf^{+} Laf^{-} State of expression of lateral *(peritrichous)* flagella, denoted by + or -.

Pof^{+} Pof^{-} State of expression of *polar* flagella, denoted by + or −.

Peritrichous Having flagella evenly distributed about the body of the cell rather than at one of the *poles*.

Polar Expressing a flagellar filament at a pole of the cell body.

Some rotation measurements were also performed on the NMB102 backward swimming strain, a gift from Michio Homma, first published in 2005 [116].

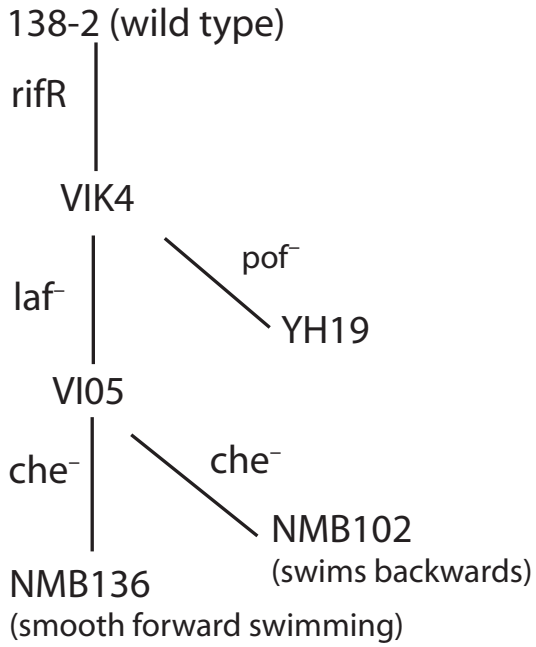

Figure C.1: *V. alginolyticus* strain chart

C.1.1 Cell Preparation

The standard protocols used to prepare stocks and daily use cultures of *V. alginolyticus* and the recipes for the growth and motility media are detailed below.

Primary Stock Preparation

A flake from an original deep frozen stock was streaked onto a plate of 1.5%[1] VC agar (for all media see recipes in C.1.2) with no antibiotics present. The high salt concentration of the VC medium was sufficient to prevent the growth of other species.

After overnight incubation at 30°C a single colony was picked from the streak plate and grown at 30°C with shaking for 24hrs in 5ml of VC medium.

20% glycerol was added to the culture at the end of the growth period and the stock was divided into 100μl aliquots which were snap frozen in liquid nitrogen and stored at -80°C.

Daily Culture Preparation

Optimised protocol as mentioned in Section 3.2.1.

[1] All % (w/v).

100μl of frozen stock from aliquot was inoculated in 3ml of VPG growth medium and grown with shaking at 30°C for 2.5hrs, to coincide with mid to late log-phase.[2] The culture was refrigerated at 4°C until cells were harvested.

Cells were harvested by centrifugation of 1ml samples at (2250-3500)$\times g$ for 1 minute, washed twice and resuspended in 1ml of the required motility medium with the addition of 14μl of a 344μg/ml solution of chloramphenicol in ethanol to prevent further cell division.

C.1.2 GROWTH MEDIA RECIPES

All recipes from M. Homma [89].

Primary stock culture - VC medium

- 0.5% polypeptone
- 0.5% yeast extract
- 0.4% K_2HPO_4
- 3% NaCl
- 0.2% glucose

VC agar is made with the VC medium.

Daily culture - VPG medium

- 1% polypeptone
- 0.4% K_2HPO_4
- 3% NaCl
- 0.5% glycerol

Sodium Motility Medium - TMN 300

- 50mM TRIS-HCl pH 7.5
- 5mM $MgCl_2$
- 5mM Glucose
- 300mM NaCl

[2] See graph in section 3.1.

Potassium Motility Medium - TMK

- 50mM TRIS-HCl pH 7.5
- 5mM $MgCl_2$
- 5mM Glucose
- 300mM KCl

C.2 Culturing Chimeric *E. coli* Strain YS34

The YS34 *E. coli* chimæra strain was constructed in Nagoya by Yoshiyuki Sowa. YS34 ($\Delta cheY$, *fliC*::Tn*10*, $\Delta pilA$, $\Delta motAmotB$) was derived from strain RP4979 [117] ($\Delta cheY$) and transformed with plasmids pYS11 (*fliC* sticky filaments [118], ampicillin resistance, pBR322 derivative) and pYS13 (*pomApotB* [119], isopropyl βDthiogalactoside inducible, chloramphenicol resistance, pMMB206 derivative). Deletions of *pilA* and *motAB* were made as described in [120]; *fliC*::Tn*10* was transduced from HCB1271 [33].
This strain was used for all the experiments comprising Chapters 4 and 5.

C.2.1 Cell Preparation

The standard protocols used to prepare stocks and daily use cultures of chimeric *E. coli* and the recipes for the growth and motility media are given below.

Primary Stock Preparation

Primary stock preparation was as for *V. alginolyticus* with the substitution of TB agar for VC agar and the use of antibiotics chloramphenicol and ampicillin to preserve the plasmids.

Daily Culture Preparation

Cells were grown for 5 hours at 30°C from frozen stocks, with shaking, in tryptone broth (TB) containing antibiotics to preserve plasmids. Isopropyl βDthiogalactoside (IPTG) between 1 and 10 mM was added for low-level expression of stator proteins. Stator expression for resurrection experiments was induced by the addition of 100 mM IPTG.

Bibliography

[1] Lubert Stryer, **Biochemistry** (Freeman, 1995).

[2] A. Ashkin, JM. Dziedzic, and T. Yamane, *Optical trapping and manipulation of single cells using infrared laser beams*, Nature **330**, 769–771 (1987).

[3] C. Kural, H. Kim, S. Syed, G. Goshima, VI. Gelfand, and PR. Selvin, *Kinesin and dynein move a peroxisome in vivo: a tug-of-war or coordinated movement?*, Science **308**, 1469–1472 (2005).

[4] R. Mallik, BC. Carter, SA. Lex, SJ. King, and SP. Gross, *Cytoplasmic dynein functions as a gear in response to load*, Nature **427**, 649–652 (2004).

[5] JE. Baker, EB. Krementsova, GG. Kennedy, A. Armstrong, KM. Trybus, and DM. Warshaw, *Myosin V processivity: multiple kinetic pathways for head-to-head coordination*, Proceedings of the National Academy of Science USA **101**, 5542–5546 (2004).

[6] ML. Walker, SA. Burgess, JR. Sellers, F. Wang, JA. Hammer, J. Trinick, and PJ. Knight, *Two-headed binding of a processive myosin to F-actin*, Nature **405**, 804–807 (2000).

[7] C. Veigel, F. Wang, ML. Bartoo, JR. Sellers, and JE. Molloy, *The gated gait of the processive molecular motor, myosin V*, Nature Cell Biology **4**, 59–65 (2002).

[8] AD. Mehta, RS. Rock, M. Rief, JA. Spudich, MS. Mooseker, and RE. Cheney, *Myosin-V is a processive actin-based motor*, Nature **400**, 590–593 (1999).

[9] W. Steffen, D. Smith, R. Simmons, and J. Sleep, *Mapping the actin filament with myosin*, Proceedings of the National Academy of Science USA **98**, 14949–14954 (2001).

[10] NJ. Carter and RA. Cross, *Mechanics of the kinesin step*, Nature **435**, 308–312 (2005).

[11] C. Veigel, S. Schmitz, F. Wang, and JR. Sellers, *Load-dependent kinetics of myosin-V can explain its high processivity*, Nature Cell Biology **7**, 861–869 (2005).

[12] B. Yurke, AJ. Turberfield, AP. Mills, FC. Simmel, and JL. Neumann, *A DNA-fuelled molecular machine made of DNA*, Nature **406**, 605–608 (2000).

[13] AJ. Turberfield, JC. Mitchell, B. Yurke, AP. Mills, MI. Blakey, and FC. Simmel, *DNA fuel for free-running nanomachines*, Physical Review Letters **90**, 118102–118102 (2003).

[14] P. Yin, H. Yan, XG. Daniell, AJ. Turberfield, and JH. Reif, *A unidirectional DNA walker that moves autonomously along a track*, Angewandte Chemie International Edition English **43**, 4906–4911 (2004).

[15] J. Bath, SJ. Green, and AJ. Turberfield, *A free-running DNA motor powered by a nicking enzyme*, Nature Structural and Molecular Biology **44**, 4358–4361 (2005).

[16] R. Yasuda, H. Noji, M. Yoshida, K. Kinosita, and H. Itoh, *Resolution of distinct rotational substeps by submillisecond kinetic analysis of F1-ATPase*, Nature **410**, 898–904 (2001).

[17] T. Nishizaka, K. Oiwa, H. Noji, S. Kimura, E. Muneyuki, M. Yoshida, and K. Kinosita, *Chemomechanical coupling in F1-ATPase revealed by simultaneous observation of nucleotide kinetics and rotation*, Nat Struct Mol Biol **11**, 142–148 (2004).

[18] H. Itoh, A. Takahashi, K. Adachi, H. Noji, R. Yasuda, M. Yoshida, and K. Kinosita, *Mechanically driven ATP synthesis by F1-ATPase*, Nature **427**, 465–468 (2004).

[19] M. Diez, B. Zimmermann, M. Börsch, M. König, E. Schweinberger, S. Steigmiller, R. Reuter, S. Felekyan, V. Kudryavtsev, CA. Seidel, and P. Gräber, *Proton-powered subunit rotation in single membrane-bound F0F1-ATP synthase*, Nature Structural and Molecular Biology **11**, 135–141 (2004).

[20] G. Oster, H. Wang, and M. Grabe, *How Fo-ATPase generates rotary torque*, Philosophical Transactions of the Royal Society of London B **355**, 523–528 (2000).

[21] J. Xing, H. Wang, C. von Ballmoos, P. Dimroth, and G. Oster, *Torque generation by the Fo motor of the sodium ATPase*, Biophysical Journal **87**, 2148–2163 (2004).

[22] RM. Macnab, *Flagella and motility in* Escherichia coli *and* S. typhimurium, Cellular and Molecular Biology pages 123–145 (1996).

[23] RM. Berry and JP. Armitage, *The bacterial flagella motor*, Advances in Microbial Physiologyiol **41**, 291–337 (1999).

[24] S. Ravid and M. Eisenbach, *Minimal requirements for rotation of bacterial flagella*, Journal of Bacteriology **158**, 1208–1210 (1984).

[25] JZ. Liu, M. Dapice, and S. Khan, *Ion selectivity of the* Vibrio alginolyticus *flagellar motor*, Journal of Bacteriology **172**, 5236–5244 (1990).

[26] G. Lowe, M. Meister, and HC. Berg, *Rapid rotation of flagellar bundles in swimming bacteria*, Nature **325**, 637–640 (1987).

[27] M. Silverman and M. Simon, *Flagellar rotation and the mechanism of bacterial motility*, Nature **249**, 73–74 (1974).

[28] SH. Larsen, RW. Reader, EN. Kort, WW. Tso, and J. Adler, *Change in direction of flagellar rotation is the basis of the chemotactic response in Escherichia coli*, Nature **249**, 74–77 (1974).

[29] HC. Berg, *Dynamic properties of bacterial flagellar motors*, Nature **249**, 77–79 (1974).

[30] HC. Berg and RA. Anderson, *Bacteria swim by rotating their flagellar filaments*, Nature **245**, 380–382 (1973).

[31] HC. Berg and L. Turner, *Torque generated by the flagellar motor of Escherichia coli*, Biophysical Journal **65**, 2201–2216 (1993).

[32] AD. Rowe, MC. Leake, H. Morgan, and RM. Berry, *Rapid rotation of micron and sub-micron dielectric particles measured using optical tweezers*, Journal of Modern Optics **50**, 1539–1554 (2003).

[33] WS. Ryu, RM. Berry, and HC. Berg, *Torque-generating units of the flagellar motor of* Escherichia coli *have a high duty ratio*, Nature **403**, 444–447 (2000).

[34] S. Kudo, Y. Magariyama, and S. Aizawa, *Abrupt changes in flagellar rotation observed by laser darkfield microscopy*, Nature (1990).

[35] Y. Magariyama, S. Sugiyama, K. Muramoto, I. Kawagishi, Y. Imae, and S. Kudo, *Simultaneous measurement of bacterial flagellar rotation rate and swimming speed*, Biophysical Journal **69**, 2154–2162 (1995).

[36] J. Gimsa, T. Schnelle, G. Zechel, and R. Glaser, *Dielectric spectroscopy of human erythrocytes: investigations under the influence of nystatin*, Biophysical Journal **66**, 1244–1253 (1994).

[37] KL. Chan, H. Morgan, E. Morgan, IT. Cameron, and MR. Thomas, *Measurements of the dielectric properties of peripheral blood mononuclear cells and trophoblast cells using AC electrokinetic techniques*, Biochimica et Biophysica **1500**, 313–322 (2000).

[38] RM. Berry, L. Turner, and HC. Berg, *Mechanical limits of bacterial flagellar motors probed by electrorotation*, Biophysical Journal **69**, 280–286 (1995).

[39] KC. Neuman, EH. Chadd, GF. Liu, K. Bergman, and SM. Block, *Characterisation of photodamage to* Escherichia coli *in optical traps*, Biophysical Journal **77**, 2856–2863 (1999).

[40] A. Ashkin, *Forces of a single-beam gradient laser trap on a dielectric sphere in the ray optics regime*, Biophysical Journal (1992).

[41] JA. Lock, *Calculation of the radiation trapping force for laser tweezers by use of generalized Lorenz-Mie theory. I. Localized model description of an on-axis tightly focused laser beam with spherical aberration*, Applied Optics **43**, 2532–2544 (2004).

[42] JA. Lock, *Calculation of the radiation trapping force for laser tweezers by use of generalized Lorenz-Mie theory. II. On-axis trapping force*, Applied Optics **43**, 2545–2554 (2004).

[43] K. Svoboda and SM. Block, *Biological applications of optical forces*, Annual review of Biophysical and Biomolecular Structure **23**, 247–285 (1994).

[44] MC. Leake, **The Elasticity of the Giant Muscle Protein Titin Investigated Using a Laser-Tweezers Technique**, D.Phil thesis, King's College London, 2001.

[45] SM. Block, CL. Asbury, JW. Shaevitz, and MJ. Lang, *Probing the kinesin reaction cycle with a 2D optical force clamp*, Proceedings of the National Academy of Science USA **100**, 2351–2356 (2003).

[46] RM. Simmons, JT. Finer, S. Chu, and JA. Spudich, *Quantitative measurements of force and displacement using an optical trap*, Biophysical Journal **70**, 1813–1822 (1996).

[47] A. Ashkin, *Optical trapping and manipulation of neutral particles using lasers*, Proceedings of the National Academy of Science USA (1997).

[48] MJ. Lang and SM. Block, *Laser-based optical tweezers*, American Journal of Physics **71**, 201–215 (2002).

[49] N. Pralle, M. Prummer, E. Florin, EH. Stelzaer, and JKH. Horber, *Three dimensional high resolution particle tracking for optical tweezers by forward scattered light*, Microscopy research and technique **44**, 378–386 (1999).

[50] EJG. Peterman, F. Gittes, and CF. Schmidt, *Laser-induced heating in optical traps*, Biophysical Journal **84**, 1308–1316 (2003).

[51] DF. Blair and HC. Berg, *Restoration of torque in defective flagellar motors*, Science **242**, 1678–1681 (1988).

[52] L. Turner, WS. Ryu, and HC. Berg, *Real time imaging of fluorescent flagellar filaments*, Journal of Bacteriology **182**, 2793–2801 (2000).

[53] S Ravid, P Matsumura, and M Eisenbach, *Restoration of flagellar clockwise rotation in bacterial envelopes by insertion of the chemotaxis protein CheY*, Proceedings of the National Academy of Science USA **83**, 7157–7161 (1986).

[54] SA. Lloyd, FG. Whitby, DF. Blair, and CP. Hill, *Structure of the c-terminal domain of flig, a component of the rotor in the bacterial flagellar motor*, Nature **400**, 472–475 (1999).

[55] PN. Brown, CP. Hill, and DF. Blair, *Crystal structure of the middle and c-terminal domains of the flagellar rotor protein flig*, The EMBO Journal **21**, 3225–3234 (2002).

[56] RM. Berry and HC. Berg, *Torque generated by the flagellar motor of* Escherichia coli *while driven backward*, Biophysical Journal **76**, 580–587 (1999).

[57] X. Chen and HC. Berg, *Torque-speed relationship of the flagellar rotary motor of escherichia coli*, Biophysical Journal **78**, 1036–1041 (2000).

[58] FC. Neidhardt, JL. Ingraham, KB. Low, B. Magasanik, M. Schaechter, and HE. Umbarger, **Escherichia coli and Salmonella typhimurium Cellular and Molecular Biology**, volume 1 (American Society for Microbiology, 1987).

[59] FC. Neidhardt, JL. Ingraham, KB. Low, B. Magasanik, M. Schaechter, and HE. Umbarger, **Escherichia coli and Salmonella Typhimurium Cellular and Molecular Biology**, volume 2 (American Society for Microbiology, 1987).

[60] Y. Imae and T. Atsumi, *Na+ driven bacterial flagellar motors*, Journal of Bioenergetics and Biomembranes **21**, 705–716 (1989).

[61] K. Muramoto, Y. Magariyama, M. Homma, I. Kawagishi, S. Sugiyama, Y. Imae, and S. Kudo, *Rotational fluctuation of the sodium-driven flagellar motor of vibrio alginolyticus induced by binding of inhibitors*, Journal of Molecular Biology **259**, 687–695 (1996).

[62] T. Atsumi, L. McCarter, and Y. Imae, *Polar and lateral flagellar motors of marine vibrio are driven by different ion-motive forces*, Nature **355**, 182–184 (1992).

[63] T. Atsumi, Y. Maekawa, T. Yamada, I. Kawagishi, Y. Imae, and M. Homma, *Effect of viscosity on swimming by the lateral and polar flagella of vibrio alginolyticus*, Journal of Bacteriology **178**, 5024–5026 (1996).

[64] M. Homma, H. Oota, S. Kojima, I. Kawagishi, and Y. Imae, *Chemotactic responses to an attractant and a repellent by the polar and lateral flagellar systems of vibrio alginolyticus*, Microbiology **142**, 2777–2783 (1996).

[65] Y. Sowa, H. Hotta, M. Homma, and A. Ishijima, *Torque-Speed relationship of the Na+ driven flagellar motor of* Vibrio alginolyticus, Journal of Molecular Biology **327**, 1043–1051 (2003).

[66] H. Tokuda and T. Unemoto, *Na+ is translocated at NADH:quinone oxidoreductase segment in the respiratory chain of Vibrio alginolyticus*, Journal of Biological Chemistry **259**, 7785–7790 (1984).

[67] H. Tokuda and T. Unemoto, *Characterization of the respiration-dependent Na+ pump in the marine bacterium Vibrio alginolyticus*, Journal of Biological Chemistry **257**, 10007–10014 (1982).

[68] JP. Armitage and RM. Macnab, *Unidirectional, intermittent rotation of the flagellum of Rhodobacter sphaeroides*, Journal of Bacteriology **169**, 514–518 (1987).

[69] HL. Packer and JP. Armitage, *The unidirectional flagellar motor of Rhodobacter sphaeroides WS8 can rotate either clockwise or counterclockwise: characterization of the flagellum under both conditions by antibody decoration*, Journal of Bacteriology **175**, 6041–6045 (1993).

[70] KA Morehouse, IG Goodfellow, and RE Sockett, *A chimeric N-terminal Escherichia coli–C-terminal Rhodobacter sphaeroides FliG rotor protein supports bidirectional E. coli flagellar rotation and chemotaxis*, Journal of Bacteriology **187**, 1695–1701 (2005).

[71] RM Macnab, *How bacteria assemble flagella*, Annu Rev Microbiol **57**, 77–100 (2003).

[72] HS. Young, H. Dang, Y. Lai, DJ. DeRosier, and S. Khan, *Variable symmetry in Salmonella typhimurium flagellar motors*, Biophysical Journal **84**, 571–577 (2003).

[73] PN Brown, MA Mathews, LA Joss, CP Hill, and DF Blair, *Crystal structure of the flagellar rotor protein FliN from Thermotoga maritima*, Journal of Bacteriology **187**, 2890–2902 (2005).

[74] FA. Samatey, H. Matsunami, K. Imada, S. Nagashima, TR. Shaikh, DR. Thomas, JZ. Chen, DJ. Derosier, A. Kitao, and K. Namba, *Structure of the bacterial flagellar hook and implication for the molecular universal joint mechanism*, Nature **431**, 1062–1068 (2004).

[75] SM. Block, DF. Blair, and HC. Berg, *Compliance of bacterial flagella measured with optical tweezers*, Nature **338**, 514–517 (1989).

[76] T Minamino, Y Saijo-Hamano, Y Furukawa, B González-Pedrajo, RM Macnab, and K Namba, *Domain organization and function of Salmonella FliK, a flagellar hook-length control protein*, Journal of Molecular Biology **341**, 491–502 (2004).

[77] K Imada, FA Samatey, H Matsunami, S Nagashima, A Kitao, K Yonekura, S Maki-Yonekuraz, and K Namba, *[Structure, function and self-assembly of the bacterial flagellum]*, Tanpakushitsu Kakusan Koso **50**, 1328–1334 (2005).

[78] S. Kojima and DF. Blair, *Conformational change in the stator of the bacterial flagellar motor*, Biochemistry **40**, 13041–13050 (2001).

[79] TF. Braun, S. Poulson, JB. Gully, C. Empey, S. Van Way, A. Putnam, and DF. Blair, *Function of proline residues of MotA in torque generation by the flagellar motor of* Escherichia coli, Journal of Bacteriology **181**, 3542–3551 (1999).

[80] TF. Braun and DF. Blair, *Targeted disulfide cross-linking of the MotB protein of* Escherichia coli*: evidence for two H+ channels in the stator complex*, Biochemistry **40**, 13051–13059 (2001).

[81] M. Meister, G. Lowe, and HC. Berg, *The proton flux through the bacterial flagellar motor*, Cell **49**, 643–650 (1987).

[82] J. Zhou and D.F. Blair, *Residues of the cytoplasmic domain of mota essential for torque generation in the bacterial flagellar motor*, Journal of Molecular Biology (1997).

[83] J. Zhou, SA. Lloyd, and DF. Blair, *Electrostatic interactions between rotor and stator in the bacterial flagellar motor*, Proceedings of the National Academy of Science USA **95**, 6436–6441 (1998).

[84] HC Berg, *The rotary motor of bacterial flagella*, Annual Review of Biochemistry **72**, 19–54 (2003).

[85] LL. McCarter, *MotY, a Component of the Sodium-Type Flagellar Motor*, Journal of Bacteriology **176**, 4219–4225 (1994).

[86] LL. McCarter, *MotX, the Channel Component of the Sodium-Type Flagellar Motor*, Journal of Bacteriology **176**, 5988–5998 (1994).

[87] Y. Asai, S. Kojima, H. Kato, N. Nishioka, I. Kawagishi, and M. Homma, *Putative channel components for the fast-rotating sodium-driven flagellar motor of a marine bacterium*, Journal of Bacteriology **179**, 5104–5110 (1997).

[88] M Okabe, T Yakushi, and M Homma, *Interactions of MotX with MotY and with the PomA/PomB sodium ion channel complex of the Vibrio alginolyticus polar flagellum*, Annual Review of Microbiology **280**, 25659–25664 (2005).

[89] K. Muramoto, I. Kawagishi, S. Kudo, Y. Magariyama, Y. Imae, and M. Homma, *High-speed rotation and speed stability of the sodium-driven flagellar motor in vibrio alginolyticus*, Journal of Molecular Biology **251**, 50–58 (1995).

[90] KK. Gosink and CC. Hase, *Requirements for conversion of the Na+ driven flagellar motor of* Vibrio cholerae *to the H+ driven motor of* Escherichia coli, Journal of Bacteriology **182**, 4234–4240 (2000).

[91] Y. Asai, I. Kawagishi, RE. Sockett, and M. Homma, *Hybrid Motor with H+ - and Na+ -Driven Components can Rotate* Vibrio *Polar Flagella by using Sodium Ions*, Journal of Bacteriology **181**, 6332–6338 (1999).

[92] Y. Asai, I. Kawagishi, RE. Sockett, and M. Homma, *Coupling ion specificity of chimeras between H+ and Na+ driven motor proteins in* Vibrio *polar flagella*, The EMBO Journal **19**, 3639–3648 (2000).

[93] RM. Berry, *Torque and switching in the bacterial flagellar motor: an electrostatic model*, Biophysical Journal **64**, 961–973 (1993).

[94] M. Meister, SR. Caplan, and HC. Berg, *Dynamics of a tightly coupled mechanism for flagellar rotation*, Biophysical Journal **55**, 905–914 (1989).

[95] AD. Samuel and HC. Berg, *Fluctuation analysis of rotational speeds of the bacterial flagellar motor*, Proceedings of the National Academy of Science USA **92**, 3502–3506 (1995).

[96] AD Samuel and HC Berg, *Torque-generating units of the bacterial flagellar motor step independently*, Biophysical Journal **71**, 918–923 (1996).

[97] J Happel and H Brenner, **Low Reynolds number hydrodynamics** (Martinus Nijhoff Publishers (Kluwer Group), 1983).

[98] DC. Duffy, JC. McDonald, OJA. Schueller, and GM. Whitesides, *Rapid prototyping of microfluidic systems in poly(dimethylsiloxane)*, Analytical Chemistry **70**, 4974–4984 (1998).

[99] LD. Landau, EM. Lifshitz, and LP. Pitaevskii, **Statistical Physics** (Pergamon NY, 1980).

[100] HC. Berg, **Random Walks in Biology** (Princeton, 1993).

[101] T. Yorimitsu and M. Homma, *Na+ -driven flagellar motor of vibrio*, Biochimica et Biophysica Acta **1505**, 82–93 (2000).

[102] CV. Gabel and HC. Berg, *The speed of the flagellar rotary motor of* Escherichia coli *varies linearly with protonmotive force*, Proceedings of the National Academy of Science USA **100**, 8748–8751 (2003).

[103] CJ. Lo, MC. Leake, and RM. Berry, *Fluorescence Measurement of Intracellular Sodium Concentration in single* Escherichia coli *cells*, Biophysical Journal - IN PRESS (2005).

[104] E. Padan, M. Venturi, Y. Gerchman, and N. Dover, *Na(+)/H(+) antiporters*, Biochimica et Biophysica **1505**, 144–157 (2001).

[105] J. Steuber, C. Schmid, M. Rufibach, and P. Dimroth, *Na+ translocation by complex I (NADH:quinone oxidoreductase) of* Escherichia coli, Molecular Microbiology **35**, 428–434 (2000).

[106] SH. Chung and RA. Kennedy, *Forward-backward non-linear filtering technique for extracting small biological signals from noise*, Journal of Neuroscience Methods **40**, 71–86 (1991).

[107] S. Reid, MC. Leake, JH. Chandler, CJ. Lo, JP. Armitage, and RM. Berry, *The bacterial flagellar motor contains at least 11 torque-generating units*, IN PRESS (2005).

[108] DC. Fung and HC. Berg, *Powering the flagellar motor of Escherichia coli with an external voltage source*, Nature **375**, 809–812 (1995).

[109] Y Sowa, AD Rowe, MC Leake, T Yakushi, M Homma, A Ishijima, and RM Berry, *Direct observation of steps in rotation of the bacterial flagellar motor*, Nature **437**, 916–919 (2005).

[110] K. Svoboda, CF. Schmidt, BJ. Schnapp, and SM. Block, *Direct observation of kinesin stepping by optical trapping interferometry*, Nature **365**, 721–727 (1993).

[111] MJ. Schnitzer and SM. Block, *Kinesin hydrolyses one ATP per 8-nm step*, Nature **388**, 386–390 (1997).

[112] R. Yasuda, H. Noji, K. Kinosita, and M. Yoshida, *F1-ATPase is a highly efficient molecular motor that rotates with discrete 120 degree steps*, Cell **93**, 1117–1124 (1998).

[113] DR. Thomas, DG. Morgan, and DJ. DeRosier, *Rotational symmetry of the C ring and a mechanism for the flagellar rotary motor*, Proceedings of the National Academy of Science USA **96**, 10134–10139 (1999).

[114] HC. Berg, *Constraints on models for the flagellar rotary motor*, Philosophical Transactions of the Royal Society of London B **355**, 491–501 (2000).

[115] S. Kojima, T. Atsumi, K. Muramoto, S. Kudo, I. Kawagishi, and M. Homma, Vibrio alginolyticus *mutants resistant to phenamil, a specific inhibitor of the sodium-driven flagellar motor*, Journal of Molecular Biology **265**, 310–318 (1997).

[116] Y. Magariyama, M. Ichiba, K. Nakata, K. Baba, T. Ohtani, S. Kudo, and T. Goto, *Difference in bacterial motion between forward and backward swimming caused by the wall effect*, Biophysical Journal **88**, 3648–3658 (2005).

[117] BE. Scharf, KA. Fahrner, L. Turner, and HC. Berg, *Control of direction of flagellar rotation in bacterial chemotaxis*, Proceedings of the National Academy of Science USA **95**, 201–206 (1998).

[118] G. Kuwajima, *Construction of a minimum-size functional flagellin of* Escherichia coli, Journal of Bacteriology **170**, 3305–3309 (1988).

[119] Y. Asai, T. Yakushi, I. Kawagishi, and M. Homma, *Ion-coupling determinants of Na+-driven and H+-driven flagellar motors*, Journal of Molecular Biology **327**, 453–463 (2003).

[120] KA. Datsenko and BL. Wanner, *One-step inactivation of chromosomal genes in* Escherichia coli *K-12 using PCR products*, Proceedings of the National Academy of Science USA **97**, 6640–6645 (2000).